HİTİT
UNIVERSITY

ISSN 2148-4171

JOURNAL OF SCIENCE & ENGINEERING
HITTITE

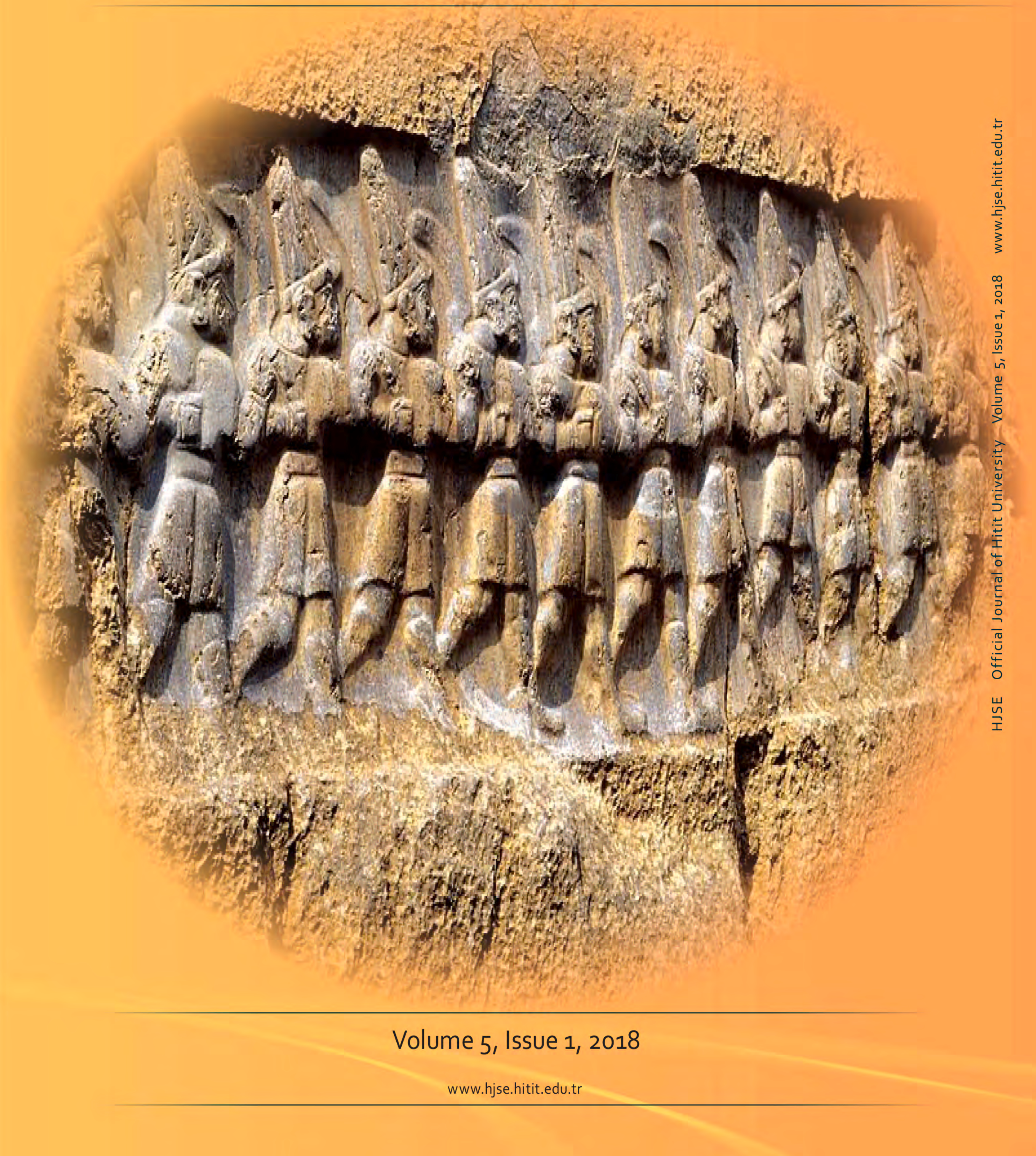

HJSE Official Journal of Hitit University Volume 5, Issue 1, 2018 www.hjse.hitit.edu.tr

Volume 5, Issue 1, 2018

www.hjse.hitit.edu.tr

JOURNAL OF SCIENCE & ENGINEERING
HITTITE

Cytotoxic Effects of Zinc Oxide on Human Periodontal Ligament Fibroblasts In Vitro 1-5

Şükran Şeker

This study describes potential cytotoxic effect of ZnO on human periodontal ligament fibroblasts (hPDLFs) in vitro.

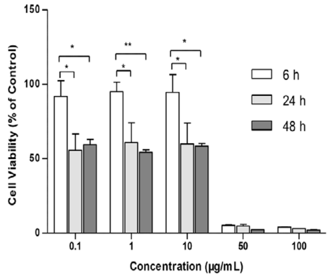

Triazole substituted phthalocyanines and their electrochemical properties

7-12

Rıza Bayrak

The main goal of this work is to prepare new metal free and metallo Pcs (cobalt(II), Zinc(II) and tin(II)) containing triazole and Schiff base moieties

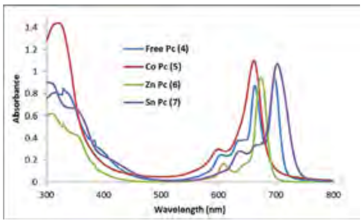

Cationic Dye Degradation by Means of an Efficient Photocatalyst Promoted by Aluminum Oxide 13-17

Kinyas Polat

In this study magnetic $MgFe_2O_4$ particles and Al_2O_3 were used for the first time as an efficient adsorbent to improve the photocatlytic activity of Ag_3VO_4 in methylene blue degradation under visible light illumination from the aqueous solution.

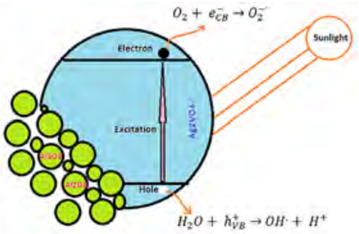

Failure Analysis of Graphene Sheets with Multiple Stone-Thrower-Wales Defects Using Molecular-Mechanics Based Nonlinear Finite Element Models 19-24

Cengiz Baykasoglu and Ata Mugan

Physical or experimental measurements for prediction of fracture behavior of carbon-based nanostructures are very limited due to challenges associated with designing experiments at the nanoscale.

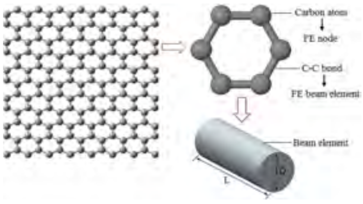

A New Demodulator For Inverse Pulse Position Modulation Technique

25-29

Mehmet Sönmez

In order to generate I-PPM signal, one of the most widely used modulator structures is mux-based techniques because mux-based architectures operates using codeword table.

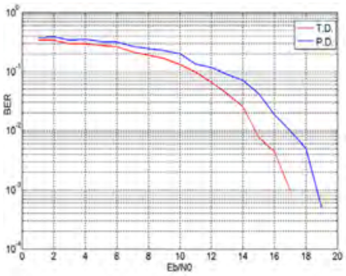

Rotor Slot Distance Effects on Output Parameters in Single Phase Induction Motors 31-35

Merve Şen Kurt and Ahmet Fenercioğlu

In this paper, rotor slot distance influences on SPIM with run capacitors have been examined. Speed, currents, shaft torque, power factor, efficiency have predicted and compared by 2D FEM for each slot distance.

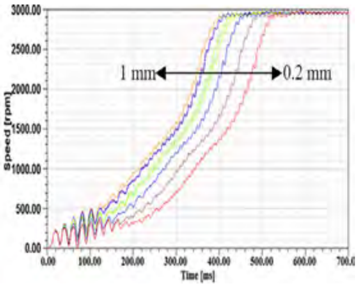

Rehabilitation of Francis Turbines of Power Plants with Computational Methods

37-48

Kutay Celebioglu, Selin Aradag, Ece Ayli and Burak Altintas

This article presents a Computational Fluid Dynamics (CFD) based rehabilitation procedure involving the state of the art redesign of the turbine of a hydroelectric power plant for better performance at design and off-design conditions of several head and flow rates.

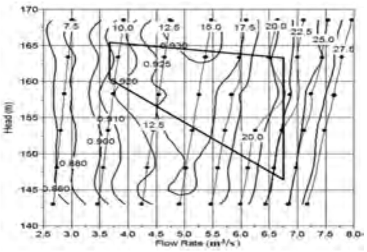

Synthesis, characterization and electrochemical performance of Nb doped $LiFePO_4$/C cathodes

49-55

Cengiz Bağcı and Öncü Akyıldız

The aim of this work is to produce $LiFePO_4$/C nano composite cathode material with high purity and high electrochemical performance using the mechanochemical activation.

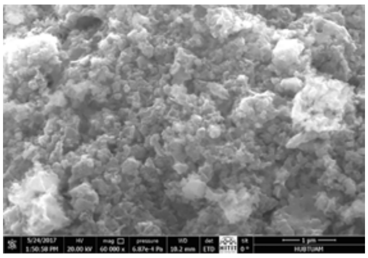

Some Geological Features of Limestone Aggregates Produced from Central Anatolian Carbonate Formations

57-61

Gürsel Kansun, Veysel Zedef and Kerim Koçak

Easy crack-down of the limestones is the result of weak bond values between Ca-O-C even in the metamorphic limestones. The Bozlutepe Limestones are highly fragmented and have irregularly scattered fracture and joint systems.

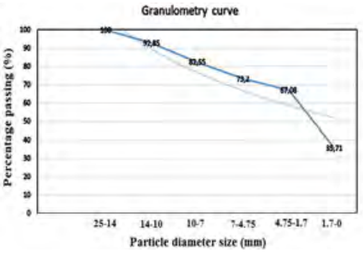

Determination of Phase Transformation and Activation Energy in High Temperature Shape Memory Ti-V-Al Alloy

63-68

Semra Ergen

Activating the solid-solid transformation of the alloy is much easier than with the Ni-Ti alloy, which is an advantage for the Ti-V-Al alloy.

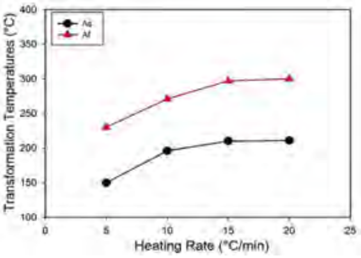

The Synthesis and Spectral Properties of Benzofuran Derivative Bis-Chalcone

69-73

Neslihan Beyazıt

A new bis-chalcone containing benzofuran moiety was synthesized from Claisen Schmidt condensation reaction of khellinone with terephthalaldehyde and its spectral properties was described in details.

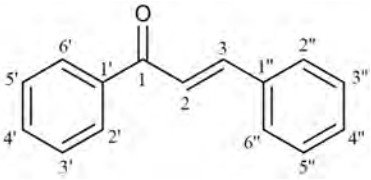

The Effect of Welding Positions on the Weldability of X20CrMoV11-1 Steels

75-83

Bünyamin Çiçek, Emine Gündoğdu İş, Emre Gümüş and Polat Topuz

The X20CrMoV11-1 steels have been widely used in thermal power plant applications in combustion chambers and other high-temperature parts.

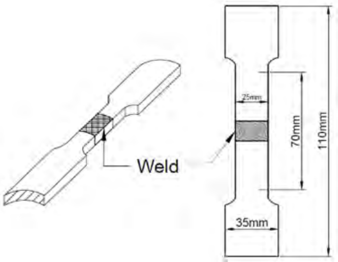

Owner
Prof. Dr. Reha Metin ALKAN
on behalf of Hitit University

Editor-in-chief
Prof. Dr. Ali Kılıçarslan

Associate Editors
Assoc. Prof. Dr. D. Ali Köse
Asst. Prof. Dr. Öncü Akyıldız

Production
Assoc. Prof. Dr. Kazım Köse
Mustafa Güzel
Mustafa Reşit Haboğlu
Erhan Çetin

Proofreading
Asst. Prof. Dr. Aytekin Uzunoğlu
Dr. Hülya Çakmak

Editor’s Office
Tel: +90 364 227 45 33 / 12 36
Fax: +90 364 227 45 35
Email: alikilicarslan@hitit.edu.tr

Subscription Service:
Tel: +90 364 227 45 33 / 12 82
Fax: +90 364 227 45 35
Email: hjse@hitit.edu.tr

EDITORIAL BOARD

Prof. Dr. Iftikhar AHMAD	University of Malakand, Chakdara, Pakistan
Prof. Dr. Mike BECKETT	Bangor University, Bangor, United Kingdom
Prof. Dr. İbrahim DİNÇER	Uoit Ontario University, Ontario, Canada
Prof. Dr. Ali ELKAMEL	University of Waterloo, Ontario, Canada
Prof. Dr. Mohamad S QATU	Central Michigan University, Michigan, United States
Prof. Dr. Saffa RIFFAT	The University of Nottingham, United Kingdom
Prof. Dr. Thanos SALIFOGLOU	Aristotle University of Thessaloniki, Thessaloniki, Greece
Assoc. Prof. Dr. Yuehong SU	The University of Nottingham, United Kingdom
Dr. Wojciech NOGALA	Polish Academy of Sciences, Poland
Prof. Dr. Yusuf AYVAZ	Suleyman Demirel University, Turkey
Prof. Dr. Adil DENİZLİ	Hacettepe University, Turkey
Prof. Dr. Ali GENCER	Ankara University, Turkey
Prof. Dr. Metin GÜRÜ	Gazi University, Turkey
Prof. Dr. Murat HOŞÖZ	Kocaeli University, Turkey
Prof. Dr. Sadık KAKAÇ	TOBB University, Turkey
Prof. Dr. Tarık Ömer OĞURTANI	Middle East Technical University, Turkey
Prof. Dr. Ender SUVACI	Anadolu University, Turkey
Assoc. Prof. Dr. Ali TOPÇU	Hacettepe University, Turkey
Prof. Dr. Satılmış BASAN	Hitit University, Turkey
Prof. Dr. Vedat DENİZ	Hitit University, Turkey
Prof. Dr. Ali KILIÇARSLAN	Hitit University, Turkey
Prof. Dr. Aydın ÖZLÜK	Hitit University, Turkey
Prof. Dr. Menderes SUİÇMEZ	Hitit University, Turkey
Prof. Dr. Seçil SATIR	Hitit University, Turkey
Prof. Dr. Faruk GÖKMEŞE	Hitit University, Turkey
Prof. Dr. Uğur Adnan SEVİL	Hitit University, Turkey
Prof. Dr. İbrahim SÖNMEZ	Hitit University, Turkey
Assoc. Prof. Dr. Abdurrahman ASAN	Hitit University, Turkey
Assoc. Prof. Dr. Kazım Savaş BAHÇECİ	Hitit University, Turkey
Assoc. Prof. Dr. Elif DALYAN	Hitit University, Turkey
Assoc. Prof. Dr. Naki ÇOLAK	Hitit University, Turkey
Assoc. Prof. Dr. Hakan GÜNGÜNEŞ	Hitit University, Turkey
Assoc. Prof. Dr. Bülent KABAK	Hitit University, Turkey
Assoc. Prof. Dr. Dursun Ali KÖSE	Hitit University, Turkey
Assoc. Prof. Dr. İrfan KURTBAŞ	Hitit University, Turkey
Assoc. Prof. Dr. Fatma Muazzez ŞİMŞİR	Hitit University, Turkey
Assoc. Prof. Dr. Dilber Esra YILDIZ	Hitit University, Turkey

MASTHEAD

Journal Name : HITTITE JOURNAL OF SCIENCE AND ENGINEERING
Year : 2018
Managing Editor : Prof. Dr. Ali KILIÇARSLAN
Managing Office : Hitit University Faculty of Engineering
Managing Office Tel : +90 364 227 45 33 / 12 36
Publication Language : English
Publication Type : Peer Reviewed, Open Access, International Journal
Delivery Format : 4 times a year
Print ISSN : 2149-2123
Publisher : Bir Medya
Publisher Address : Yeniyol Mah. Gazi 12. Sok. No:9/13 ÇORUM
Publisher Tel : +90 364 225 66 64

EDITORIAL

This new issue of Hittite Journal of Science and Engineering (HJSE) contains manuscripts within different aspects of the science and engineering. I would like to express my gratitude to all our authors and contributing reviewers of this issue. Due to an increase in the number of submitted articles we change our publication plan starting with this volume, thereafter HJSE will publish four issues in a year, where each issue will contain twelve articles.

I would like to thank to the President of Hitit University, Prof. Dr. Reha Metin Alkan, for his constant interest in HJSE and also to the Associate Editors of HJSE, namely Dr. Dursun Ali Kose and Dr. Oncu Akyildiz. Special thanks is due to our Production Team, Dr. Kazim Kose, Mustafa Guzel, Mustafa Resit Haboglu, Erhan Çetin and to our Proofreaders Dr. Aytekin Uzunoglu. Dr. Hülya Çakmak. I also would like to thank to the Editorial Board from national and international universities.

It's my pleasure to invite the researchers and scientists from all branches of science and engineering to join us by sending their best papers for publication in Hittite Journal of Science and Engineering.

Dr. Ali Kilicarslan

Editor-in-Chief

Hittite Journal of Science and Engineering, 2018, 5(1) 01-05
ISSN NUMBER: 2148-4171
DOI: 10.17350/HJSE19030000070

Cytotoxic Effects of Zinc Oxide on Human Periodontal Ligament Fibroblasts *In Vitro*

Şükran Şeker
Ankara University Stem Cell Institute and Ankara University Faculty of Science, Tissue Engineering, Biomaterials and Nanobiotechnology Laboratory, Ankara, TURKEY

ABSTRACT

Zinc oxide (ZnO) has been widely used in wound dressing, food additive and root canal filling material owing to its antibacterial and antifungal properties. This study describes potential cytotoxic effect of ZnO on human periodontal ligament fibroblasts (hPDLFs) in vitro. ZnO was characterized using BET (Braun-Emmet-Teller) and DLS (dynamic light scattering) analyses. The hPDLFs were treated with 0.1, 1, 10, 50 and 100 µg/mL of ZnO for 6 h, 24 h and 48 h durations. After exposure to ZnO, phase contrast microscopy, transmission electron microscopy (TEM), mitochondrial function (MTT) and lactate dehydrogenase (LDH) assays were used to evaluate cell morphology, particle uptake, cell viability and membrane leakage. In addition, real time cell responses to ZnO exposure were monitored by impedance measurements. Results indicated that ZnO exposure caused toxic effect in a dose- and time-dependent manner when compared to control group, especially at 50 and 100 µg/mL.

Article History:
Received: 2017/08/01
Accepted: 2017/09/30
Online: 2017/12/22

***Correspondence to**: Şükran Şeker, Ankara University Stem Cell Institute and Ankara University, Tissue Engineering, Biomaterials and Nanobiotechnology Laboratory, Ankara, Turkey*
Tel: +90 (312) 583-6623
Fax: +90 (312) 583-6605
E-Mail: sukran.seker@gmail.com

Keywords:
Cytotoxicity, Zinc oxide, Periodontal ligament fibroblasts, Impedance, *In vitro* toxicity assays.

INTRODUCTION

Zinc oxide (ZnO) is used extensively in various fields, ranging from rubber, ceramics, food and coating to cosmetic, medical and pharmaceutical industry due to its unique properties such as antibacterial, antifungal, anti-corrosive, low electrical conductivity and high heat resistance [1, 2]. ZnO particles have been incorporated into various polymers to improve the antimicrobial properties of materials for food packaging [3] and wound dressing [4]. Furthermore, antibacterial and antifungal activities of ZnO have received significant interest in endodontics as a filling material in root canal sealers [5, 6]. ZnO together with eugenol, called as zinc oxide-eugenol (ZOE), has been used as a filling material for many years in clinical dentistry. Nowadays, new endodontic sealers containing ZnO are still being developed to improve the bioactivity and antibacterial activity of cementation materials [7, 8].

The evaluation of the possible toxic effects with regard to exposure to chemical or biological agents is crucial for maintaining human health. Therefore, a better understanding of their toxic effects on human health will provide significant insights into their safe use [9]. In order to evaluate the potential toxic effect of a substance, a variety of *in vitro* assays (e.g., MTT, LDH and ROS) have been performed. These methods are based on evaluation of changes in cell growth, membrane leakage or reactive oxygen species production, which allow determination of cell responses at a specific time point. In recent years, impedance-based systems began to gain importance in toxicological studies due to providing label-free and real time monitoring of cell adhesion, proliferation, and death [10]. One of these, real-time cell analysis (RTCA) system uses an electrode-plates (E-plate) with gold microelectrode incorporated in the bottom of the well of culture plates. The microelectrodes are connected to a computer that measures electrical impedance changes in response to an applied voltage. The changes in electrical impedance are converted into cell index (CI) [11]. The impedance in culture medium without cell results from the ion environment at the electrode/culture medium interface. When the cell attaches onto the E-plate, the ionic environment at the electrode/culture medium interface changes, causing higher impedance. The increase in cell number attached to the E-plate leads to larger increase in electrode impedance. The electrode impedance can also be affected by the degree of interaction between electrode surface and cell. The strong attachment of cell to the electrode surface leads to a larger increase in electrical impedance [12]. By this means, the change in CI gives particular information about cell viability, morphology, migration and adhesion in real time.

The aim of this study is to evaluate the toxic effects of ZnO on human periodontal ligament fibroblast using MTT [3-(4,5-dimethylthiazol-2-yl)-2,5-diphenyltetrazolium bromide] assay, LDH assay and real-time impedance-based assay. The ZnO characterization was performed using BET (Braun-Emmet-Teller) and DLS (dynamic light scattering) analyses. The cellular uptake of ZnO within cells was evaluated by transmission electron microscopy (TEM).

MATERIALS AND METHODS

Chemicals and reagents

ZnO powder, MTT and LDH assay kits were purchased from Sigma (St. Louis, MO, USA). DMEM, L-glutamine and penicillin/streptomycin were purchased from Lonza (Biowhittaker, Verviers, Belgium). All other chemicals were obtained from Sigma.

Braun-Emmet-Teller (BET) analysis

BET analysis was used to measure the mean specific surface area of ZnO. The measurements were carried out using Quantachrome NOVA 2200e (Instruments, Boynton Beach, FL, USA).

Zeta potential and DLS analysis

Before measurements, ZnO suspension (100 µg/mL) was prepared in the cell medium and sonicated in an ultrasonic bath for 5 minutes to obtain homogenous dispersion. Then, thirteen measurements were carried out by Malvern's NanoZetasizer-ZS (Worcestershire, UK) at 25°C.

hPDLF culture

Cells were purchased from ATCC, defrost and adapted to culture conditions, and were used in all experiments. Briefly, the frozen cells in the cryovials were thawed and cultured in DMEM including 10% FBS, 100 U/mL penicilin, 100 µg/mL streptomycin and 1% non-essential amino acids under standard culture conditions (5% CO_2 at 37°C in a humidified atmosphere).

ZnO exposure

The ZnO powder sterilization was performed using UV irradiation for 30 minutes. The sterile stock suspension was prepared in culture media and sonicated for 30 min. Then, the stock solution was diluted to desired concentrations (0.1, 1, 10, 50 and 100 µg/mL) in cell culture medium. In ZnO exposure experiments, the hPDLF cells were seeded at a density of 1.0×10^4 cells/well into 96-well plates and cultured for 1 day. Then, the culture medium was replaced with the ZnO-containing medium. The cells were cultured with ZnO suspensions for 6 h, 24 h and 48 h. Control cells were cultured with cell culture medium without any particle. The morphology of human PDLFs was examined after ZnO exposure using an inverted microscope (Zeiss, Jena, Germany). Before imaging, the cells were washed carefully with PBS to remove excess particles.

TEM analysis

The subcellular localization of ZnO in hPDLF cells was observed by TEM (transmission electron microscopy). After 48 h of exposure to ZnO, the cells were washed and harvested by centrifugation. Sample preparation for TEM was performed according to a previously reported method [13]. The cell sections were imaged under a JEOL 100 CX TEM (Tokyo, Japan).

MTT assay

After 6 h, 24 h and 48 h of exposure to ZnO, cell viability was determined by MTT assay. Control cells were incubated in normal culture medium without ZnO. Optical density at 570 nm was detected using a microplate reader (Molecular Devices, Sunnyvale, CA, USA).

LDH assay

Membrane leakage assay was performed using a LDH Toxicology Assay kit (Sigma), as described in detail elsewhere [13]. LDH leakage was normalized to positive control cells as 100%.

Real-time impedance measurements

Impedance measurements were carried out using the xCELLigence Real-Time Cell Analyzer (RTCA) DP (Roche, Basel, Switzerland) in real time. For that purpose, the hPDLF cells were seeded in the wells of E-plates at a density of 12.5×10^3 cells/well, and cultured at 37°C and 5% CO_2 for 15 h. Thereafter, ZnO suspensions were added into each well of E- plate (final concentration of 0.1, 1, 10, 50 and 100 µg/mL). As a control, the cells were cultured with cell medium without ZnO. The CI changes were continuously monitored at 15 min intervals for 100 h. To determine whether particle interference had occurred, the CI measurement was also carried out with ZnO solutions (in culture medium) with the highest concentrations used in this study.

Statistical analysis

Data were collected from three independent experiments, displayed as the mean±SD, and analysed by two-way ANOVA with Bonferroni post-test using GraphPad Prism software version 5.00 (GraphPad Software, San Diego, California, USA).

RESULTS AND DISCUSSION

Particle characterization

The physicochemical properties of a substance such as surface area, surface charge, and hydrodynamic diameter have major effects on its toxicity, fate and mechanisms in cells [14, 15]. The particle surface area obtained from BET analysis was

8.886 m^2/g. The particle size distribution, zeta (ζ) potential and polydispersity index (PDI) of the ZnO were determined by DLS measurements (Table 1). The average hydrodynamic diameter of ZnO was 842.4 nm (Figure 1 and Table 1). The particle size distribution measurements retrieved from the DLS analysis indicated that ZnO might have a tendency to aggregate in cell culture medium.

Cell morphology

The inverted microscopy images of control and ZnO-exposed cells are shown in Figure 2. As seen in the images, the control cells showed the characteristic fibroblastic morphology. The hPDLF cells exposed to low concentration of ZnO (0.1 µg/mL) showed no dramatic morphology changes. Whereas, at 100 µg/mL ZnO, the cells had a round morphology, showed weaker attachment to the surface. The results indicated that exposure of PDLFs to high concentration of ZnO resulted in dramatic changes in morphology.

Subcellular localization of ZnO

TEM analysis is one of the basic methods for determination of intracellular distribution of particles following uptake into cells [16]. TEM images of control and exposed cells are presented in Figure 3. The results revealed that ZnO particles were mostly located within cytoplasmic vacuoles, whereas, any particle was not observed in uniformly homogeneous vacuoles of control cell, as in previous studies [17, 18].

Table 1. Characterization of ZnO

BET results (m2/g)	*8.886*
Average diameter in DLS (nm)	*842.4*
Polydispersity index	*0.540*
Zeta potential (mV)	*13.6*

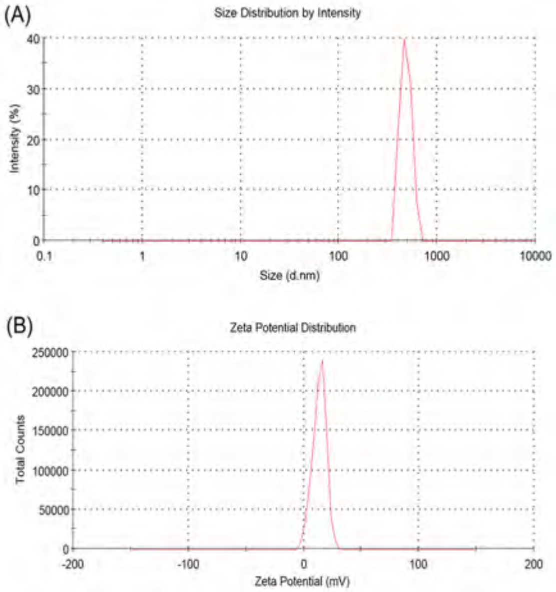

Figure 1. Particle size distribution (A) and zeta potential (B) results of the ZnO.

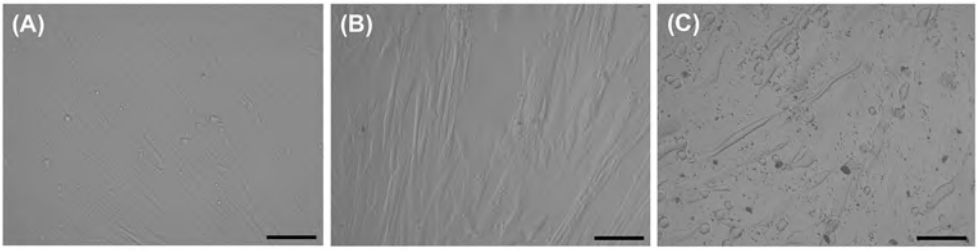

Figure 2. Inverted microscopy images of hPDLF cells. (A) Control cells. Cells exposed to (B) 0.1 µg/mL ZnO, and (C) 100 µg/mL ZnO for 48 h. Scale bars: 200 µm.

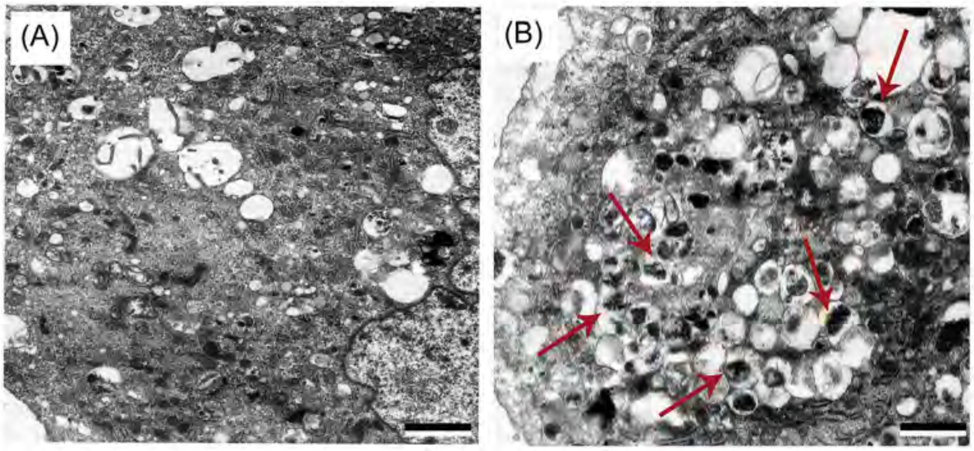

Figure 3. TEM micrographs of the hPDLF cells. (A) Control cells, and (B) cells exposed to ZnO. The arrows indicate the localization of ZnO particles in the vacuoles. Scale bars: 1 µm.

MTT results

hPDLF cells were treated with different concentrations of ZnO for 6 h, 24 h and 48h. Then, the cell viabilities were assessed by the MTT assay and data were normalized to unexposed cells. It is clearly seen from Figure 4, after 6 h of exposure, ZnO at concentrations below 50 µg/mL did not exhibit a significant toxic effect on hPDLFs. After 24 h and 48 h of exposure, ZnO at low concentrations (0.1, 1 and 10 µg/mL) resulted in ~50-60 % decrease in the cell viability, while the cell viability at all three time points significantly decreased at higher concentrations (50 and 100 µg/mL) of ZnO. These results showed that exposure to ZnO caused cell death in a concentration- and time -dependent manner.

LDH results

The measurement of LDH activity has been widely used to determine the loss of membrane integrity related to cell death [19, 20]. In this study, cell membrane integrity was assessed by measuring the released LDH from cells with damaged membrane. As seen in the Figure 5, exposure to ZnO for 6 h resulted in no significant difference between exposed groups, regardless of the concentration used. After 24 h of exposure, LDH release significantly increased, especially at 50 and 100 µg/mL. The results indicated that exposure to ZnO at concentrations above 10 µg/mL caused membrane damage and LDH release in hPDLFs.

Impedance profiles

Real-time cell responses to different concentrations of ZnO were monitored by impedance-based system. The normalized cell index (NCI) measurements of control and ZnO-exposed cells are shown in Figure 6. The results indicated that impedance profiles of cells exposed to 0.1, 1 and 10 µg/mL ZnO had similarity with the control cells. However, the NCI values at concentrations of 50 µg/mL and 100 µg/mL started to decrease at ~4 hours after exposure. After 12 hours, NCI values rapidly decreased to zero. The results of the real-time impedance measurements indicated that the presence of 50 and 100 µg/mL ZnO caused toxic effect on hPDLFs.

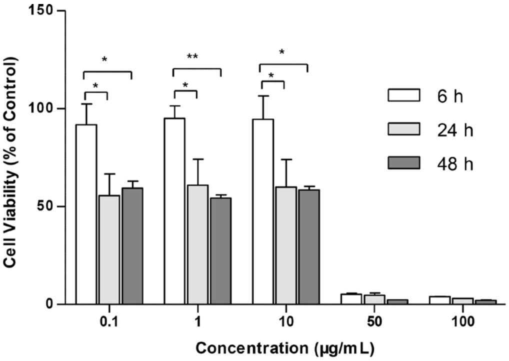

Figure 4. Cell viability results of hPDLFs exposed to 0.1-100 µg/mL of ZnO for 6 h, 24 h and 48 h. Data were expressed as the mean±SD, and conducted using the two-way ANOVA with Bonferroni post-test. Asterisks show significant differences between the groups: * = *p*<0.05, ** = *p*<0.01.

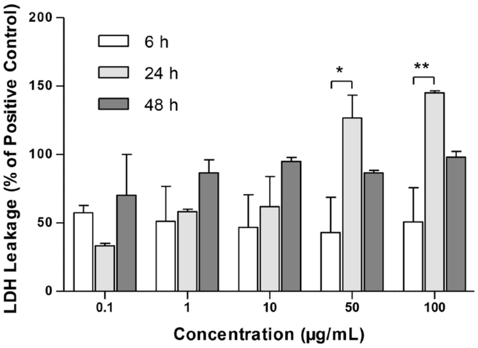

Figure 5. LDH release of hPDLF cells exposed to 0.1-100 µg/mL of ZnO for 6 h, 24 h and 48 h. Data were expressed as the mean±SD, and conducted using the two-way ANOVA with Bonferroni post-test. Asterisks show significant differences between the groups: * = *p*<0.05, ** = *p*<0.01.

CONCLUSION

Endodontic sealers may cause inflammatory responses and periodontal tissue damage. Therefore, it is necessary to know their toxic effects on periodontal tissues [21]. *In vitro* toxicity assays used mammalian cell culture systems have been commonly performed to evaluate the biocompatibility of dental materials using cell lines (e.g., HeLa, 3T3, L929 cells) [22] or primary cells (e.g., PDLFs, dental pulp cells) [23]. In the study, hPDLF cells were exposed to different concentration of ZnO and the toxic effects of ZnO were evaluated using MTT, LDH and real-time impedance based assays. The results of this study demonstrated that the toxic effect is related to exposure concentration and time. Impedance-based assay could be implemented as an effective and sensitive tool for

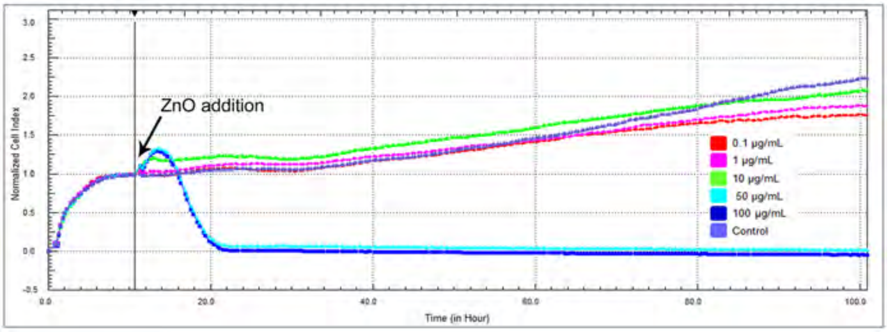

Figure 6. Real-time cell impedance profiles of hPDLF cells treated with different concentrations of ZnO.

long-term monitoring of hPDLF cell responses. Morever, the results indicated that ZnO at concentration below 10 μg/mL had no significant toxic effects on hPDLF cells.

ACKNOWLEDGMENTS

This study was performed at Ankara University Faculty of Science, Tissue Engineering, Biomaterials and Nanobiotechnology Laboratory (ElcinLab). I would like to express my sincere gratitude to Professor Yaşar Murat Elçin and Professor Ayşe Eser Elçin for their continuous support and scientific guidance.

REFERENCES

1. Kołodziejczak–Radzimska A, Jesionowski T. Zinc oxide–from synthesis to application: a review. Materials 7(4) (2014) 2833–2881.
2. Esteban–Tejeda L, Prado C, Cabal B, Sanz J, Torrecillas R, Moya JS. Antibacterial and antifungal activity of ZnO containing glasses. PloS One 10(7) (2015) e0132709.
3. Castro–Mayorga JL, Fabra MJ, Pourrahimi AM, Olsson RT, Lagaron JM. The impact of zinc oxide particle morphology as an antimicrobial and when incorporated in poly (3–hydroxybutyrate–co–3–hydroxyvalerate) films for food packaging and food contact surfaces applications. Food and Bioproducts Processing 101 (2017) 32–44.
4. Mohandas A, Sudheesh Kumar PT, Raja B, Lakshmanan VK, Jayakumar R. Exploration of alginate hydrogel/nano zinc oxide composite bandages for infected wounds. International Journal of Nanomedicine 10 (2015) 53–66.
5. Thosar N, Chandak M, Bhat M, Basak S. In Vitro Antimicrobial Efficacy of Zinc Oxide with Peppermint Oil in Comparison to Zinc Oxide Eugenol against Four Root Canal Microorganisms. Journal of Medical and Dental Science Research 3(9) (2016) 53–58.
6. Kaur A, Shah N, Logani A, Mishra N. Biotoxicity of commonly used root canal sealers: A meta–analysis. Journal of Conservative Dentistry 18(2) (2015) 83–88.
7. Oprea O, Andronescu E, Ficai D, Ficai A, Oktar FN, Yetmez M. ZnO applications and challenges. Current Organic Chemistry 18(2) (2014) 192–203.
8. Javidi M, Zarei M, Naghavi N, Mortazavi M, Nejat AH. Zinc oxide nano–particles as sealer in endodontics and its sealing ability. Contemporary Clinical Dentistry 5(1) (2014) 20–24.
9. Papavlassopoulos H, Mishra YK, Kaps S, Paulowicz I, Abdelaziz R, Elbahri M, Maser E, Adelung R, Röhl C. Toxicity of functional nano–micro zinc oxide tetrapods: impact of cell culture conditions, cellular age and material properties. PLoS One 9(1) (2014) e84983.
10. Dönmez Güngüneş Ç, Şeker Ş, Elçin AE, Elçin YM. A comparative study on the in vitro cytotoxic responses of two mammalian cell types to fullerenes, carbon nanotubes and iron oxide nanoparticles. Drug and Chemical Toxicology 40(2) (2017) 215–227.
11. Martinez–Serra J, Gutierrez A, Muñoz–Capó S, Navarro–Palou M, Ros T, Amat JC, Lopez B, Marcus TF, Fueyo L, Suquia AG, Gines J, Rubio F, Ramos R, Besalduch J. xCELLigence system for real–time label–free monitoring of growth and viability of cell lines from hematological malignancies. OncoTargets and Therapy 7 (2014) 985–994.
12. Urcan E, Haertel U, Styllou M, Hickel R, Scherthan H, Reichl FX. Real–time xCELLigence impedance analysis of the cytotoxicity of dental composite components on human gingival fibroblasts. Dental Materials 26(1) (2010) 51–58.
13. Şeker Ş, Elçin AE, Yumak T, Sınağ A, Elçin YM. In vitro cytotoxicity of hydrothermally synthesized ZnO nanoparticles on human periodontal ligament fibroblast and mouse dermal fibroblast cells. Toxicology in Vitro 28(8) (2014) 1349–1358.
14. Gatoo MA, Naseem S, Arfat MY, Mahmood Dar A, Qasim K, Zubair S. Physicochemical properties of nanomaterials: implication in associated toxic manifestations. BioMed Research International 2014 (2014) 1–8.
15. Pan CH, Liu WT, Bien MY, Lin IC, Hsiao TC, Ma CM, Lai CH, Chen MC, Chuang KJ, Chuang HC. Effects of size and surface of zinc oxide and aluminum–doped zinc oxide nanoparticles on cell viability inferred by proteomic analyses. International Journal of Nanomedicine 9 (2014) 3631–3643.
16. Milić M, Leitinger G, Pavičić I, Zebić Avdičević M, Dobrović S, Goessler W, Vinković Vrček I. Cellular uptake and toxicity effects of silver nanoparticles in mammalian kidney cells. Journal of Applied Toxicology 35(6) (2015) 581–592.
17. Lin W, Xu Y, Huang CC, Ma Y, Shannon KB, Chen DR, Huang YW. Toxicity of nano–and micro–sized ZnO particles in human lung epithelial cells. Journal of Nanoparticle Research 11(1) (2009) 25–39.
18. Condello M, De Berardis B, Ammendolia MG, Barone F, Condello G, Degan P, Meschini S. ZnO nanoparticle tracking from uptake to genotoxic damage in human colon carcinoma cells. Toxicology In Vitro 35 (2016) 169–179.
19. Niles AL, Moravec RA, Riss TL. In vitro viability and cytotoxicity testing and same–well multi–parametric combinations for high throughput screening. Current Chemical Genomics 3 (2009) 33–41.
20. Ng CT, Yong LQ, Hande MP, Ong CN, Yu LE, Bay BH, Baeg GH. Zinc oxide nanoparticles exhibit cytotoxicity and genotoxicity through oxidative stress responses in human lung fibroblasts and Drosophila melanogaster. International Journal of Nanomedicine 12 (2017) 1621–1637.
21. Silva EJNLD, Santos CC, Zaia AA. Long–term cytotoxic effects of contemporary root canal sealers. Journal of Applied Oral Science 21(1) (2013) 43–47.
22. Ashraf H, MoradiMajd N, Mozayeni MA, Dianat O, Mahjour F, Yadegari Z. Cytotoxicity evaluation of three resin–based sealers on an L929 cell line. Dental Research Journal 9(5) (2012) 549–553.
23. Chakar S, Changotade S, Osta N, Khalil I. Cytotoxic evaluation of a new ceramic–based root canal sealer on human fibroblasts. European Journal of Dentistry 11(2) (2017) 141–148.

Hittite Journal of Science and Engineering, 2018, 5 (1) 07-12
ISSN NUMBER: 2148-4171
DOI: 10.17350/HJSE19030000071

Triazole substituted phthalocyanines and their electrochemical properties

Rıza Bayrak
Vocational School of Health Services, Sinop University, Sinop, TURKEY

Article History:
Received: 2017/08/22
Accepted: 2017/09/25
Online: 2017/12/22

***Correspondence to**: Rıza Bayrak*
Vocational School of Health Services, Sinop University, Sinop, Turkey
Tel: +90 (368) 271-65 30
Fax: +90 (368) 271-48 22
E-Mail: bayrakriza@gmail.com

ABSTRACT

New cobalt (II), zinc (II), tin (II) and metal free phthaloyanines having peripherally triazole and Schiff's base groups on were synthesized and their electrochemical properties were studied. In the first step of the synthetic procedure, triazole moiety, in the second step Shiff base moiety and in the third step key compound substituted phthalonitrile have been synthesized successfully in high yield. At the final stage target phthalocyanines have been obtained and characterized by combination of spectral analysis. The electrochemical measurements showed that while Free- and Sn-Pc give irreversible oxidation process, Co- and Zn- phthalocyanines give quasi-reversible electron transfer reaction in dichloromethane solution.

Keywords:
Phthalocyanine; Metallophthalocyanine; Triazole; Schiff base; Electrochemistry.

INTRODUCTION

Phthalocyanines (Pcs) can be used many different applications such as gas sensors, electrochromic devices, photovoltaic cells and photodynamic therapy (PDT), due to their 18-π planar conjugate electron system [1-4]. Therefore synthesizing Pcs having different groups play a vital role in promoting these high technologies.

These macrocyclic compounds are ideal building blocks for applications when they are modified with groups in the desired properties. For this reason, substitution of Pcs either on peripheral/non-peripheral or axial positions has vital importance for their utilizations. Furthermore, the solubility of Pc derivatives plays a critical role in order to use in all those applications. Phthalocyanines that unsubstituted are not soluble in common organic solvents due to the aggregation. These compounds can be made soluble in organic solvents by integration of substituents in the periphery/non-periphery of Pc core, thus increasing their electrochemical and catalysis applications. [5].

1,2,4-Triazole derivatives are one of the key organic compound class have an important functions in biological applications. It's known that some of 1,2,4-triazoles exhibit biological trenchancy e.g. antifungal, anti microbial, anti viral, anti tubercular, antidepressant, anti inflammatory, anti oxidant anti convulsant and anticancer [6-8]. Furthermore, Schiff base derivatives of [1,2,4] triazoles have been identified having diverse pharmacological properties, like antifungal, antimicrobial, anticancer, antioxidant, anticonvulsant and anti-tubercular activities [9-12]. Moreover, Schiff bases bearing 1,2,4-triazole ring play important roles in coordination chemistry as they easily stable complexes with most transition metal ions [13, 14].

Recently, Tanyeli and co-workers drew attention the promising results for photochromic applications of triazole substituted zinc(II) Pc [15]. Kantekin et al. studied on the singlet oxygen quantum yield of phthalocyanine complexes substituted with tetra triazole groups on periphery and they have studied the electrochemical properties of 1,2,4-triazole substituted Pcs [16, 17]. Bayır and co-workers have recently investigated the electrochemical properties of Pcs that have thiazole substituents containing Cobalt, Zinc and manganese as metal centers [5].

As mentioned above, to the best of our knowledge, there are few studies concerning about the electrochemical applications of triazole containing Pcs. For this purpose, the main goal of this work is to prepare new metal free and metallo Pcs (cobalt(II), Zinc(II) and tin(II)) containing triazole and Schiff base moieties with long alkyl chain and to investigate the electrochemical properties of them. Long alkyl chain and bulky heterocyclic moieties were purposely chosen and adapted the structure to overcome the insolubility and aggregation drawback of Pcs.

EXPERIMENTAL

Material and equipment used in this study and experimental studies were explained in supplementary information.

RESULTS AND DISCUSSION

Synthesis and characterization

The synthesis step of new compounds is shown in Figure 1. The starting material was synthesized the reaction which was used sodium ethoxide as basic catalyst, initial triazole and 1-bromoheptane in absolute ethanol [21], Compound **(2)** was obtained from the reaction between compound (**1**) and 4-hydroxybenzaldehyde at 160-165 °C. The phthalonitrile compound **(3)** was synthesized by using compound **(2)**, 4-nitrophthalonitrile and K_2CO_3 in DMF. In the last step, the intended compounds **(4-7)** were obtained by the cyclotetramerization of the compound **(3)** in n-pentanol at reflux temperature and by the catalyst of DBU.

The IR spectrum of compound (**1**) displayed absorption bands at 3305, 3260 cm^{-1} corresponding to the NH_2 and at 1713 cm^{-1} corresponding to triazole C=O groups, respectively. In the ^{1}H NMR spectrum of compound (**1**), the aliphatic CH_2, CH_3 and CH_2-N protons were observed at between 0.83-3.64 ppm. The ^{13}C NMR signals for aliphatic carbons were recorded at between 11-46 ppm.

In the FT-IR spectrum of compound (**2**), the -NH_2 stretching vibration of the compound (**1**) at 3305 cm^{-1} disappeared and new –OH stretching at 3171 cm^{-1} appeared and in ^{1}H-NMR spectrum of the same compound the signals of the protons for the –NH_2 group of the compound **(1)** at 4.22 ppm disappeared and new signals at 6.73 and 9.62 ppm that belong to the protons of –OH and –CH=N groups, respectively, came along after the reaction and verifies the propounded structure. ^{13}C-NMR and mass spectral data promotes the framework of the compound **(2)**.

For compound **(3)**, in the FT-IR spectral data, evidence of the nascency of the phthalonitrile compound is the disappearence of the –OH stretching of compound **(2)** and the appearence of a novel vibration at 2234 cm^{-1} that belongs to C≡N group. From the ^{1}H NMR and ^{13}C NMR measurements, the absence of signal of the –OH proton of compound **(2)** and the new carbon signals at 116.84 and 116.33 ppm that belong to nitrile carbons verifies the formation of the anticipated product. Mass spectral values confirmed the desired structure.

Cyclotetramerization of a substituted phthalonitrile is a general way to synthesize of modified Pcs. It is necessary to use high boiling solvents (Dimethylaminoethanol, n-pentanol etc.) and catalysts (DBU) [3, 22]. During the preparation of Pc compounds **(4-7)** n-pentanol and DBU were used and obtained isomeric mixtures were not

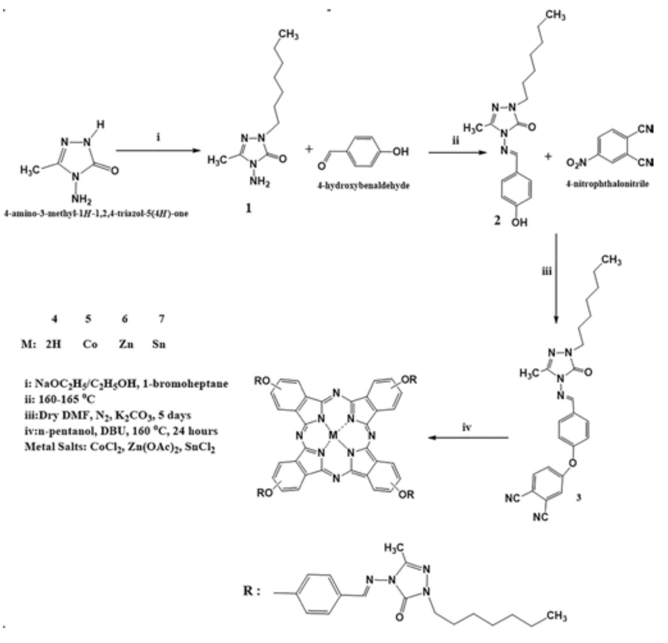

Figure 1. Reaction scheme of new compouds (**1-7**).

separated [23]. In the FT-IR spectra of Pcs **(4-7)**, the case of the achievement of the reactions is the disappearence of the vibration of the nitrile group of compound **(3)** at 2234 cm^{-1} in their spectra. Differently form metallophthalocyanines **(5-7)**, in the IR spectrum of metal-free phthalocyanine **(4)** the vibration of inner –NH group was also monitored at 3288 cm^{-1}. The rest of the spectrums of the compound **(3)** and Pcs **(4-7)** were similar. ^{1}H NMR measurement of compound **(5)** could not be carried out because of the paramagnetic central metal ion and the spectra of compounds **(4, 6, 7)** were similar to the spectrum of their starting material (compound **(3)**). Some signals were broad because of their isomeric mixture and probable aggregation at measured concentrations. However, the inner core –NH proton signal were also could not be determined because of aggregation of metal-free Pc molecule **(4)** at NMR measurement concentration [24]. Moreover, mass spectral data supported the proposed structures of the novel Pcs **(4-7)**.

Generally Pcs possess absorptions nearby 650-750 nm due to the π → π* transitions and named as Q-band and 300-350 nm -deeper π-levels to π* transitions are named as B band. Entire recent Pcs **(4-7)** were solvable in polar non aqueous solvents and their Electronic spectra were evaluated in trichloromethane (Fig. 2). Unlike the strong single absorption of Q-band of metallophthalocyanines, metal free phthalocyanines show as doublet in their electronic spectra [25]. The Q bands of the compounds **4-7** were observed at 700-665, 665, 676 and 705 nm, respectively (Fig. 2). The B bands of the substituted Pcs **(4-7)** were monitored at 324, 327, 315 and 315 nm, respectively. Furthermore the aggregation behavior of Pcs can be identified from their absorption spectra at measurement concentration and all Pcs did not show aggregation in chloroform 1x10^{-5} M concentration.

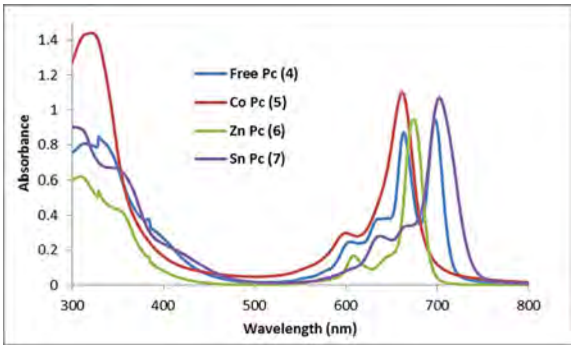

Figure 2. Electronic spectra of Pcs **(4-7)** in trichloromethane at 1x10^{-5} M concentration.

The fluorescence spectra of the Pcs were investigated in CH_2Cl_2 at 1×10^{-6} M concentration. The investigated compounds, except for Co-Pc, exhibited Stokes shift ranges from 19–42 nm in CH_2Cl_2. Fluorescence excitation and emission spectra of Sn- and Zn-Pc in CH_2Cl_2 were shown in Figure 3 and Figure S1 and data tabulated in Table 1. Fluorescence emission spectrum of Zn-Pc was of typical character for similar phthalocyanines – they mirrored

Table 1. Fluorescence data for compounds.

Compound	*Q-band wavelength (nm)*	*Excitation wavelength (nm)*	*Emission wavelength (nm)*
Free-Pc	*700, 655, 642, 609*	*703, 664, 637, 604*	*787, 723*
Zn-Pc	*676, 614*	*694, 677, 614*	*760, 699*
Co-Pc	*665, 608*	-	-
Sn-Pc	*705, 643, 670*	*699, 665, 638, 606*	*784, 738, 706, 666*

Table 2. Electrochemical data for Fc and Pcs

Compound	*E_{pa} (V)^a*	*E_{pc} (V)^a*	*$E^{o'}$ (V)^b*	*ΔE (V)^c*	*I_c/I_a*	*Egap(eV)^d*	*Egap(eV)^e*
Free-Pc	*0.445^f* *-1.129*	— *-1.262*	— *-1.196*	— *0.133*	— *2.22*	*1.65*	*1.65*
Co-Pc	*0.317* *-0.563* *-1.025*	*0.225* *-0.758* *-1.191*	*0.271* *0.661* *1.108*	*0.092* *0.195* *0.166*	*0.67* *2.59* *3.17*	*1.50*	*1.58*
Zn-Pc	*0.302* *-1.342*	*0.185* —	*0.244* —	*0.117* —	*0.72* —	*1.65*	*1.72*
Sn-Pc	*0.689^g* *-1.007* *-1.335*	— *-0.864* *-1.178*	— *0.936* *-1.257*	— *0.143* *0.157*	— *1.51* *4.10*	*1.70*	*1.59*

a: Potential (V) ***vs.*** Fc/Fc$^+$.

b: Formal standard potential ($E^{0'}$) = E_{pc} + E_{pa}/2.

c: ←E = E_{pa} - E_{pc}

d: HOMO-LUMO gap from electrochemical measurement

e: HOMO-LUMO gap from UV/vis spectroscopy

f: Potential (V) ***vs.*** Ag/AgCl.

g: Anodic peak potential for irreversible process.

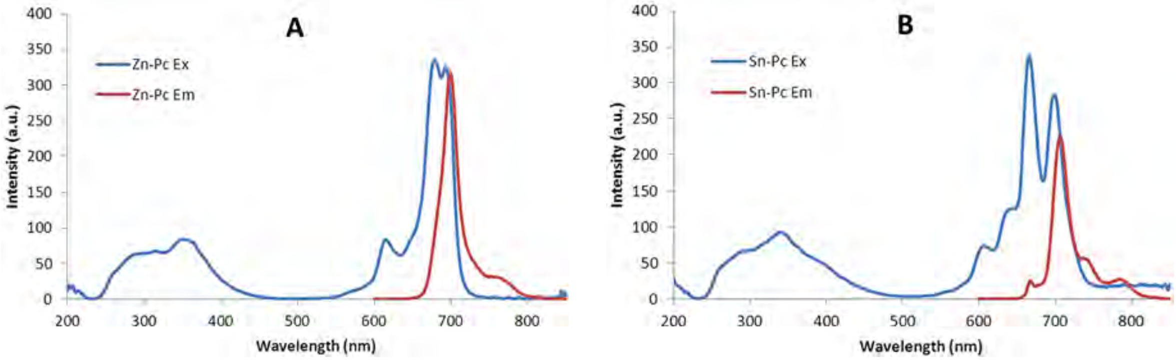

Figure 3. Fluorescence excitation and emission spectra of ZnPc (A) and SnPc (B); excitation wavelengths are 677 nm for ZnPc and 665 nm for SnPc.

the absorption Q-band with only small Stokes shift (20 nm). Because of the loss of symmetry and size of the Sn^{2+} ion coordinated to Pc ring, there was a characteristic disagreement of the absorption, excitation and emission spectra of Sn-Pc complex (Figure 3) [26]. Excitation spectra of Sn-Pc was not accordance with the absorption spectra proved that the compound was present exclusively in its aggregated state in electronic spectra [27]. Because of the enhanced spin–orbital coupling, or an energy or electron transfer mechanism properties of the paramagnetic transition metals, almost no fluorescence signal has been detected for Co-Pc (see Supplementary Fig. S1) [28, 29].

Electrochemical Studies

Electrochemical properties of compounds were investigated by using cyclic voltammetry technique in dichloromethane solution containing 0.1 M tetra-n-butylammonium perchlorate (TBAP, n-Bu_4NClO_4). The obtained electrochemical data were listed in Table 2 and voltammograms of compounds were given in Fig. 4. In order to establish electrochemical stability and reversibility criteria, cyclic voltammograms (CVs) of ferrocene were recorded in the same experimental conditions using Pt working electrodes (Figure S2). The formal standard potential ($E^{0\prime}$) of Fc^+/Fc under experimental conditions was calculated as 0.487 V vs. Ag/AgCl [ΔE_p (the anodic to cathodic peak-to-peak separation) = 0.082 V, I_{pc}/I_{pa} (the cathodic-anodic peak ratio) = 1.06].

As shown in Fig. 4, metal free Pc **(4)** gives ill-defined oxidation peak located in the positive area due to the aggregation of compound in working electrolyte system. According to literature data, this peak could be assigned to the irreversible oxidation of the Pc ring. On the other hand metal free Pc **(4)** exhibited diffusion-controlled quasi-reversible reduction features at -1.196 V. While coordination to Sn(II) center caused to shift higher potential, the broad oxidation wave of Pc ring shifted to negative potential values by coordination of Zn(II) and Co(II) metals due to the charge of the electron transfer center. Because the orbital energy level of first-row transition metal ions may be positioned between HOMO—LUMO levels of Pc ligand, coordination of metal ion to ring cavity could alter electrochemical properties of compounds. As a result of coordination through N atom of the Pc ring, CoPc **(5)** and ZnPc **(6)** compounds exhibited quasi-reversible oxidation processes at 0.271 (I_c/I_a = 0.67) and 0.244 V (I_c/I_a=0.72) vs. Fc/Fc^+, respectively (for the detailed electrochemical analysis see Supplementary Fig. S3) [30].

ZnPc **(6)** shows a totally irreversible reduction character at -1.342 V vs. Fc/Fc^+. On the other hand, reduction processes for CoPc **(5)** and SnPc **(7)** are not completely reversible in terms of both ΔE and the ratio of anodic to cathodic peak currents (Table 2). Ground state of the CoPc **(5)** corresponds to electronic configuration $(a_{1g})^2$ $(a_{1u})^2$ $(1_{eg})^3$, which yield ^2E_g state and one-electron oxidation occurs from the Pc a_{1u} orbital, the first reduction involves addition of an electron to the partially filled $1e_g$ corresponding Co-based d-orbitals [31]. Thus potential gap of the first oxidation and second reduction in cyclic voltammetry directly related to HOMO-LUMO gap. When the central metal atom is Zn or Sn, the 3d subshell is filled and removal of an electron from HOMO and addition of electron to LUMO corresponds the first oxidation and reduction couples [17]. For all the redox processes, the plots of square root of scan rate versus current were linear confirming diffusion control. The onset values of the absorption spectrum of compounds were used

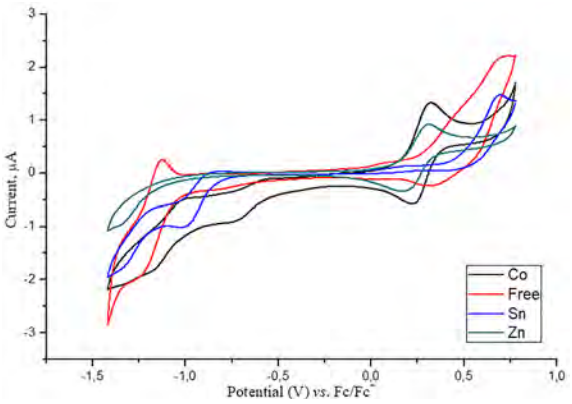

Figure 4. Cyclic voltammograms of compounds **(4-7)** at 100 mV s^{-1} scan rate in CH_2Cl_2 solution containing 0.1 M TBAP.

as an approach to estimate HOMO-LUMO gap energy of molecules and a correlation with electrochemical data have been established in Table 2 [32].

CONCLUSION

In conclusion, the preparation of metal free Co(II), Zn(II) and Sn(II) Pcs complexes bearing [1,2,4] triazole and Schiff base parts have been synthetized and electrochemical properties of these compounds have been investigated. The yields of the reactions pretty high and final obtained phthalocyanines have high solubility and did not show aggregation in organic solvents as intended. The electrochemical studies of novel compounds show that metal free Pc **(4)** exhibited diffusion-controlled quasi-reversible reduction features at -1.196 V and CoPc **(5)** and ZnPc **(6)** compounds exhibited quasi-reversible oxidation processes at 0.271 (I_c/I_a= 0.67) and 0.244 V (I_c/I_a=0.72) vs. Fc/Fc$^+$, respectively. ZnPc **(6)** shows a totally irreversible reduction character at -1.342 V vs. Fc/Fc$^+$. On the other hand, reduction processes for CoPc **(5)** and SnPc **(7)** are not completely reversible in terms of both ΔE and the ratio of anodic to cathodic peak currents.

When the central metal atom Zn or Sn the 3d subshell is filled and removal of an electron from HOMO and addition of electron to LUMO corresponds the first oxidation and reduction couples.

ACKNOWLEDGEMENT

Author thanks to Dr. Kaan Karaoğlu due to contributions to electrochemical studies.

REFERENCES

1. Kobayashi N. Optically active phthalocyanines. Coord. Chem. Rev. 99 (2001) 219–221.
2. Dede G, Bayrak R, Er M, Özkaya AR, Değirmencioğlu İ. DBU–catalyzed condensation of metal free and metallophthalocyanines containing thiazole and azine moieties: Synthesis, characterization and electrochemical properties. Journal of Organometallic Chemistry 740 (2013) 70–77.
3. Bayrak R, Dumludağ F, Akçay HT, Değirmencioğlu İ. Synthesis, characterization and electrical properties of peripherally tetra–aldazine substituted novel metal free phthalocyanine and its zinc(II) and nickel(II) complexes. Spectrochimica Acta Part A: Molecular and Biomolecular Spectroscopy 105 (2013) 550–556.
4. Ledwaba M, Masilela N, Nyokong T, Antunes E. Surface modification of silica–coated gadolinium oxide nanoparticles with zinc tetracarboxyphenoxy phthalocyanine for the photodegradation of Orange G. Journal of Molecular Catalysis A: Chemical. 403 (2015) 64–76.
5. Uzunmehmetoğlu HZ, Yenilmez HY, Kaya K, Koca A, Altındal A, Bayır ZA. Electrochemical, Spectroelectrochemical, and Dielectric Properties of Metallophthalocyanines Bearing Redox Active Cobalt and Manganese Metal Centers. Inorganica Chimica Acta. 459 (2017) 51–62.
6. Patel NB, Khan IH, Rajani SD. Pharmacological evaluation and characterizations of newly synthesized 1,2,4–triazoles. European Journal of Medicinal Chemistry. 45 (2010) 4293–4299.
7. Kharb R, Sharma PC, Yar MS. Pharmacological significance of triazole scaffold. J. Enzyme Inhib. Med. Chem. 26 (2011) 1–21.
8. Maddila S, Pagadala R, Jonnalagadda SB. 1,2,4–Triazoles: A Review of Synthetic Approaches and the Biological Activity. Lett. Org. Chem. 10 (2013) 693–714.
9. Bekircan O, Menteşe E, Ulker S, Küçük Ç. Synthesis of Some New 1,2,4–Triazole Derivatives Starting from 3–(4–Chlorophenyl)–5–(4–methoxybenzyl)–4H–1,2,4–triazol with Anti–Lipase and Anti–Urease Activities. Archive Der Pharmazie. 347 (2014) 387–397.
10. Akçay HT, Çoruh U, Bayrak R, Menteşe E, Vazquez Lopez EM. A spectroscopic study on new phthalonitrile derivative and its computational background: 4–[(4,5–Diphenyl–4H–1,2,4–triazol–3–yl)sulfanyl]benzene–phthalonitrile. Journal of Molecular Structure. 1127 (2017) 539–548.
11. Khanmohammadi H, Abnosi MH, Hosseinzadeh A, Erfantalab M. Synthesis, biological and computational study of new Schiff base hydrazones bearing 3–(4–pyridine)–5–mercapto–1,2,4–triazole moiety. Spectrochim. Acta A 71 (2008) 1474–1480.
12. Li Z, Gu Z, Yin K, Zhang R, Deng Q, Xiang J. Synthesis of substituted–phenyl–1,2,4–triazol–3–thione analogues with modified D–glucopyranosyl residues and their antiproliferative activities. Eur. J. Med. Chem. 44 (2009) 4716–4720.
13. Bagihalli GB, Avaji PG, Patil SA, Badami PS. Synthesis, spectral characterization, in vitro antibacterial, antifungal and cytotoxic activities of Co(II), Ni(II) and Cu(II) complexes with 1,2,4–triazole Schiff bases. Eur. J. Med. Chem. 43 (2008) 2639–2649.
14. Ferrer S, Haasnoot JG, Reedijk J, Muller E, Cingi MB, Lanfranchi M, Manotti AM, Ribas LJ. Trinuclear N,N–bridged copper(II) complexes involving a Cu3OH core: [Cu–3(mu(3)–OH)L(3)A(H2O)(2)]A center dot(H2O)(x) {L=3–acetylamino–1,2,4–triazolate; a = CF3SO3, NO3, ClO4; x = 0, 2} synthesis, X–ray structures, spectroscopy, and magnetic properties. Inorg. Chem. 39 (2000) 1859–1867.
15. Karaca H, Sezer S, Özalp–Yaman Ş, Tanyeli C. Concise synthesis, electrochemistry and spectroelectrochemistry of phthalocyanines having triazole functionality, Polyhedron. 72 (2014) 147–156.
16. Nas A, Fandaklı S, Kantekin H, Demirbaş A, Durmuş M. Novel organosoluble metal–free and metallophthalocyanines bearing triazole moieties: Microwave assisted synthesis and determination of photophysical and photochemical properties. Dyes and Pigments. 95 (2012) 8–17.
17. Demirbaş Ü, Kobak RZU, Akçay HT, Ünlüer D, Koca A, Çelik F, Kantekin H. Synthesis, characterization, electrochemical and spectroelectrochemical properties of novel peripherally tetra–1,2,4–triazole substituted phthalocyanines. Synthetic Metals. 215 (2016) 68–76.
18. Perrin DD, Armarego WLF. Purification of Laboratory Chemicals. Pergamon: Oxford; 1989.
19. Young GJ, Onyebuagu W. Synthesis and characterization of di–disubstituted phthalocyanines. J. Org. Chem. 55 (1990)

2155–2159.

20. Yildirim N, Bekircan O. Use of ester formylhydrazones for the synthesis of 1,2,4–triazole and 1,3,4–oxadiazole derivatives. 37 (2013) 160–163.
21. Biyiklioglu Z, Bekircan O. Synthesis and electrochemical properties of axially disubstituted silicon phthalocyanine and peripherally tetra substituted manganese(III) phthalocyanine bearing 1,2,4–triazole substituents. Synthetic Metals. 200 (2014) 148–155.
22. Demirbaş Ü. Göl C, Barut B, Bayrak R, Durmuş M, Kantekin H, Değirmencioğlu İ. Peripherally and non–peripherally tetra–benzothiazole substituted metal–free zinc (II) and lead (II) phthalocyanines: Synthesis, characterization, and investigation of photophysical and photochemical properties. Journal of Molecular Structure. 1130 (2017) 677-687.
23. Bayrak R, Akçay HT, Bıyıklıoğlu Z, Değirmencioğlu İ. Substituted phthalocyanines and their electropolymerization properties. Synthetic Metals. 220 (2016) 643-652.
24. Nas A, Kantekin H, Durmuş M, Gümrükçüoğlu N. Unmetallated and metallated phthalocyanines bearing oxadiazole groups: Synthesis, photophysical and photochemical studies. Journal of Luminescence. 154 (2014) 15-21.
25. Dilber G, Durmuş M, Kantekin H, Çakır V. Synthesis and characterization of a new soluble metal–free and metallophthalocyanines bearing biphenyl–4–yl methoxy groups. Journal of Organometallic Chemistry. 696 (2011) 2805-2814.
26. Demirbaş Ü, Pişkin M, Bayrak R, Ünlüer D, Dügdü E, Durmuş M, Kantekin H. The determination of photophysical and photochemical parameters of novel metal–free, zinc(II) and lead(II) phthalocyanines bearing 1,2,4– triazole groups. Synthetic Metals. 219 (2016) 76-82.
27. Demirbaş Ü, Pişkin M, Barut B, Bayrak R, Durmuş M, Kantekin H. Metal–free, zinc(II) and lead(II) phthalocyanines functioning with 3– (2H–benzo[d][1,2,3]triazol–2–yl)–4–hydroxyphenethyl methacrylate groups: Synthesis and investigation of photophysical and photochemical properties. Synthetic Metals. 220 (2016) 276-285.
28. Ghanem BS, Piskin M, Durmus M, El–Khouly ME, Al–Raqa SY. Synthesis, photophysical and photochemical properties of novel phthalocyanines substituted with triptycene moieties. Polyhedron. 90 (2015) 85-90.
29. Akçay HT, Piskin M, Demirbas Ü, Bayrak R, Durmus M¸ Mentese E¸ Kantekin H. Novel triazole bearing zinc(II) and magnesium(II) metallophthalocyanines: Synthesis, characterization, photophysical and photochemical properties. Journal of Organometallic Chemistry. 745–746 (2013) 379–386.
30. Demirbaş Ü, Akyüz D, Barut B, Bayrak R, Koca A, Kantekin H. Electrochemical and spectroelectrochemical properties of thiadiazole substituted metallo–phthalocyanines. Spectrochimica Acta Part A: Molecular and Biomolecular Spectroscopy. 153 (2016) 71-78.
31. Demirbas Ü, Akçay HT, Koca A, Kantekin H. Synthesis, characterization and investigation of electrochemical and spectroelectrochemical properties of peripherally tetra 4–phenylthiazole–2–thiol substituted metal–free, zinc(II), copper(II) and cobalt(II) phthalocyanines. Journal of Molecular Structure. 1141 (2017) 643–649.
32. Demirbaş Ü, Akyüz D, Mermer A, Akçay HT, Demirbaş N, Koca A, Kantekin H. The electrochemical and spectroelectrochemical properties of metal free and metallophthalocyanines containing triazole/piperazine units. Spectrochimica Acta Part A: Molecular and Biomolecular Spectroscopy. 153 (2016) 478-487.

Hittite Journal of Science and Engineering, 2018, 5 (1) 13-17
ISSN NUMBER: 2148-4171
DOI: 10.17350/HJSE19030000072

Cationic Dye Degradation by Means of an Efficient Photocatalyst Promoted by Aluminum Oxide

Kinyas Polat
Dokuz Eylul University, Department of Chemistry, Tınaztepe, Izmir, TURKEY..

Article History:
Received: 2017/08/25
Accepted: 2017/09/26
Online: 2017/12/28

***Correspondence to**: Kinyas Polat*
Department of Chemsitry, Dokuz Eylul University, Tınaztepe, Izmir, Turkey
Tel: +90 (232) 301-86 88
E-Mail: kinyas.polat@deu.edu.tr

ABSTRACT

A visible active magnetically separable two component MgFe2O4-Al2O3/Ag3VO4 photocatalyst was prepared in order to improve the catalytic activity of Ag3VO4 by utilizing Al2O3 (NPs Al2O3) adsorbent. Catalyst was characterized by using Fourier Transform Infrared spectrometer (FTIR). Photocatalytic activity of MgFe2O4-Al2O3/Ag3VO4 was measured by methylene blue (MB) degradation under visible light illumination emitted from 105 W tungsten light bulb. UV-vis spectrophotometer was employed to follow and identify the MB degradation and kinetics. Results suggested a first order kinetic model for the degradation having rate constant k, 0.03252 min-1. The half-life of catalytic degradation was found as 21.3 min. The photocatalytic activity of the neat Ag3VO4 was also measured and compared with the MgFe2O4-Al2O3/Ag3VO4. It was observed that rate constant of the degradation obtained with Ag3VO4 was 0.01577 min-1 and its half life 43.9 min. This revealed that an approximately twofold increase attained by using efficient nano Al2O3 adsorbent. At the end of the reaction catalyst particles were removed easily from the aqueous solution by a magnet.

Keywords:
Visible active photocatalyst, Methylene blue, Magnetic nanoparticle, First order kinetic, Degradation

INTRODUCTION

Rapid industrialization together with unconsciousness about environmental issues, business concerns and several other reasons prevent the factories to take robust preventing measures for released chemicals to water resources. This situation exposes extremely important health risk on the aquatic environment. Therefore, efficient technologies have to be employed to get rid of this problem. Recently photocatalytic degradation technologies by means of heterogeneous catalysis are of interest of the scientists. TiO_2 is the most heavily investigated photocatalysis to remove the dyes and other toxic chemicals from aqueous solutions up to now due to low cost, high chemical stability, high photoactivity and non-toxicity [1-3]. However, TiO_2 is only active under UV-light illumination which restricts to benefit from huge visible region of the solar spectrum because of its large band gap. Therefore, it is very important to develop photocatalysts sensitive to visible region. Several catalysts have been reported recently including $BiVO_4$, Bi_5O_7I/Bi_2O_3, $g\text{-}C_3N_4/BiOCl_xBr_{1-x}$, Ag/Ag_2CO_3-rGO, $g\text{-}C_3N_4/WO_3$ [4-9]. Among them Ag_3VO_4 attracts a lot of interest by scientist due to the appropriate band gap for the visible light adsorption, although photocatalytic activity of the catalyst is not sufficient due to the fast recombination. Recent efforts have been directed towards increasing the activity by using several strategies such as metal doping together with hybridizing [10-12], nanostructure engineering and using fast mediators such as graphene oxide and MoS_2 [13-15]. Other efficient strategy is combining photocatalytic material with a good adsorbent. By using this technique, the adsorption provides pre-concentration of molecules near the active sites of photocatalyst [16]. Other important issue in the heteregenous catalysis is the easy separation of catalyst from the medium without using conventional ways such as filtration and membrane separation. Therefore, recently $MgFe_2O_4$ nanoparticles have attracted interest of the scientist [17,18].

In this study magnetic $MgFe_2O_4$ particles and Al_2O_3 were used for the first time as an efficient adsorbent to improve the photocatlytic activity of Ag_3VO_4 in methylene blue degradation under visible light illumination from the aqueous solution.

MATERIALS AND METHODS

$FeCl_2.4H_2O$, $FeCl_3.6H_2O$, $Mg(OAc)_2.4H_2O$, NH_3 25 % solution and NaOH were taken from Merck. Al_2O_3, $AgNO_3$ and V_2O_5 were purchased from Aldrich.

Photocatalyst synthesis

V_2O_5 mixed with NaOH as 1:6 molar ratios in a round bottom flask by adding enough distilled water through continuous magnetic agitating. Then $AgNO_3$ solution was added resulting in yellow-orange precipitate. The related chemical reactions can be given as;

$$V_2O_5 + 6OH^- \xrightarrow{25\,°C} 2VO_4^{3-} + 3H_2O$$

$$3Ag^+ + VO_4^{3-} \xrightarrow{precipitation} Ag_3VO_4$$

The precipitate was left for 24 h at room temperature and washed with excess deionized water and dried at 70 °C. Calcination of the dried and cleaned precipitate was carried out at 300 °C for 4 h [19]. $MgFe_2O_4$ particles were synthesized by putting Al_2O_3 particles into the mixture of $FeCl_2.4H_2O$ and $FeCl_3.6H_2O$ in deionized water in oxygen-free Nitrogen atmosphere. Approximately 10 min later 25 % aqueous NH_3 (10 mL) was poured and stirred resulting in Fe_3O_4 particles. Co-precipitation occurred by subsequent drop wise addition of $Mg(OAc)_2.4H_2O$ to the suspension. $Mg(OH)_2$ was the final precipitate through addition of 1 M aqueous NaOH. The powder was cleaned with deionized water, filtered, dried and calcined at 550 °C for 6.5 h [20]. Subsequently, 0.5 g Ag_3VO_4 was blended with 0.5 % $MgFe_2O_4$-Al_2O_3 in an agate pestle for 30 min and calcined at 300 °C for 2 hours [21].

Photocatalytic performance evaluation

In order to determine the photocatalytic activity, MB solution including catalyst particles were illuminated under visible light of 105 W tungsten light bulb. MB concentration and the volume of the solution were $1x10^{-5}$ M and 50 mL. Photocatalyst was exposed to visible light at top of the continuously stirred beaker. Absorbance of the clear supernatants taken from the beaker at several time intervals was recorded at 664 nm wavelength by using a UV-visible spectrophotometer.

RESULTS AND DISCUSSION

Photocatalytic degradation mechanism

MB degradation or oxidation by visible light in the presence of a photocatalysis takes place mainly due to the creation of active species, such as peroxyl and hydroxyl radicals. By the attack of these radicals, MB molecule is mineralized into nontoxic products [22, 23]. A general mechanism reported frequently [23] can be given below;

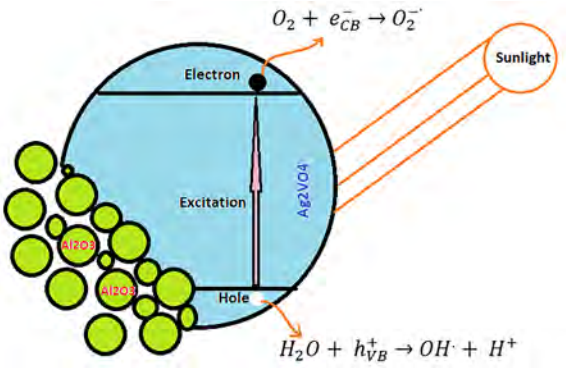

Figure 1. Schematic representation of a degradation mechanism of MB under visible light

$$Catalyst + h\gamma \xrightarrow{excitation} \left(e_{CB}^- + h_{VB}^+\right)$$

$$H_2O + h_{VB}^+ \rightarrow OH^\cdot + H^+$$

$$O_2 + e_{CB}^- \rightarrow O_2^{-}$$

$$O_2^- + H_2O \rightarrow H_2O_2$$

$$OH^\cdot\ or\ HOO^\cdot + MB \xrightarrow{degradation} inorganic\ degradation\ products\ of\ MB$$

The reaction mechanism that converts MB into final products may be represented as in the Figure 1.

Kinetics of photocatalysis

Langmuir–Hinshelwood (L–H) model is generally fitted to derive the kinetic model of the photocatalysis reactions. If MB concentration is maintained at low levels, degradation usually follows first order kinetic model [24, 25]. L-H kinetic expression is given in the equation 1.

$$r = \frac{dC}{dt} = \frac{kKC}{1+KC} \qquad (1)$$

In the L-H equation, r is the observed reaction rate, k is the intrinsic reactivity constant, K is the equilibrium adsorption constant, C is the reactant concentration. L-H expression can be reduced to first order kinetic equation for dilute solutions (1+KC equals to 1);

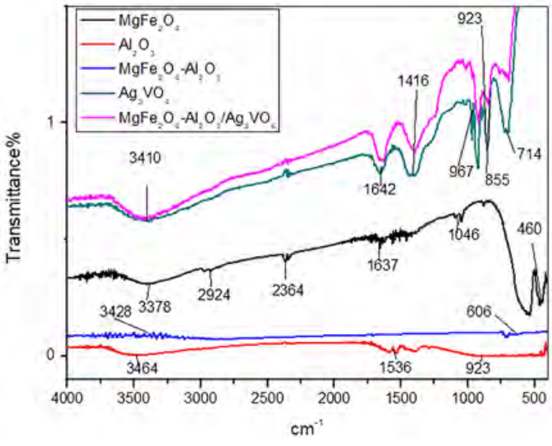

Figure 2. FTIR spectrums for $MgFe_2O_4$-Al_2O_3/Ag_3VO_4 and its individual ingredients

$$r = \frac{dC}{dt} = -k_g C \tag{2}$$

Integrating the equation 2 from C to C_0 (initial concentration of the dye) gives the linear relation of first order kinetic equation;

$$\ln\left(\frac{C}{C_0}\right) = -k_g t \tag{3}$$

C is the concentration of MB at time t, k_g is the observed rate constant. A plot of $\ln(C/C_0)$ versus t produces a linear relationship, the slope gives the observed rate constant, k_g. Half-life of the degradation is calculated by;

$$\begin{aligned}[\text{Ochratoxin A}]\left(\frac{\mu g}{ml}\right) &= \frac{\text{Abs(333nm)}\times\text{Molecular Weight}\times 1000}{\text{Ochratoxin A Extinction Coefficient}}\\ &= \frac{\text{Abs(333nm)}\times 403\times 1000}{5550}\\ &= \text{Abs(333nm)}\times 72.6\end{aligned} \tag{4}$$

Structural identity by FTIR

FTIR spectrums were collected as 50 scans at 4cm^{-1} resolution between 4000 and 400 cm^{-1} with a Perkin Elmer Spectrum BX-II FTIR spectrometer.

The absorption bands (Figure 2) at 3464-3378 cm^{-1} and 1637 cm^{-1} are due to the O-H stretching vibration of H_2O remaining after calcination. 2924 cm^{-1} and 1046 cm^{-1} represent the stretching and bending vibrations of C-H as impurities. The peak at 2364 cm^{-1} stands for the CO_2 in the air [26]. Specific bands observed at 606 and 460 cm^{-1} correspond to the metal-oxygen bonds in the tetrahedral and octahedral sites and suggest that $MgFe_2O_4$ has spinel structure [27-29]. In the spectrum of $MgFe_2O_4$/NPs-Al_2O_3 metal-oxygen band intensities showed a clear decrease. In the FTIR spectrum of Ag_3VO_4, 714 cm^{-1}, 855 cm^{-1}, 923 cm^{-1} and 967 cm^{-1} bands are due to the Ag_3VO_4. Absorptions at 923 cm^{-1} and 967 cm^{-1} represent the symmetric vibrations and 855 and 714 cm^{-1} represent the asymmetric stretching vibrations of V-O bonds in VO_3, respectively.

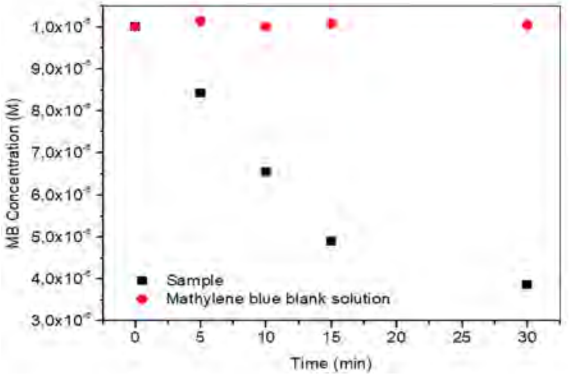

Figure 3. Decreasing MB concentration upon irradiation of $MgFe_2O_4$-Al_2O_3/Ag_3VO_4 with visible light

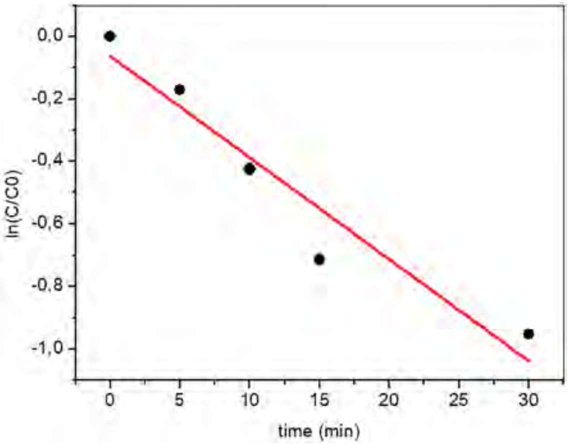

Figure 4. First order kinetic model fitting of MB degradation with $MgFe_2O_4$-Al_2O_3/Ag_3VO_4

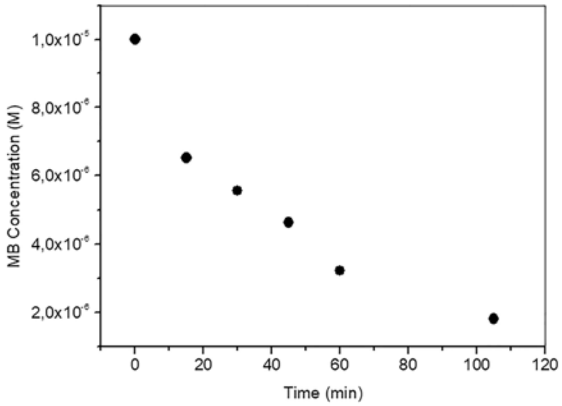

Figure 5. Decreasing MB concentration upon irradiation of Ag_3VO_4 with visible light

The absorption at 1416 cm^{-1} is due to the overtone. Since the amount of $MgFe_2O_4$-Al_2O_3 is 0.5 %, no difference was recorded between the FTIR spectrum of Ag_3VO_4 and $MgFe_2O_4$-Al_2O_3/Ag_3VO_4.

MB photocatalytic degradation

Photocatalytic MB degradation performance of $MgFe_2O_4$-Al_2O_3/Ag_3VO_4 was tested under visible light source. Remaining dye concentration in the aqueous solution upon interaction with light was measured by UV-vis spectrophotometer at 664 nm where the dye absorption reaches a maximum. The initial MB concentration was $1x10^{-5}$ M. The catalyst weight was 0,1 g. The change of MB degradation with time (Figure 3) suggests that an efficient reaction takes place upon irradiation with fast reduction in concentration of MB. Kinetic model of the degradation as seen from Figure 4 obeys to first order kinetics. Rate constant k was found to be 0,03252 min^{-1} and corresponding half-life which MB concentration decreases to half of its initial value is 21.3 min. During the experiment a methylene blue witness sample at the same concentration was placed near the main sample to

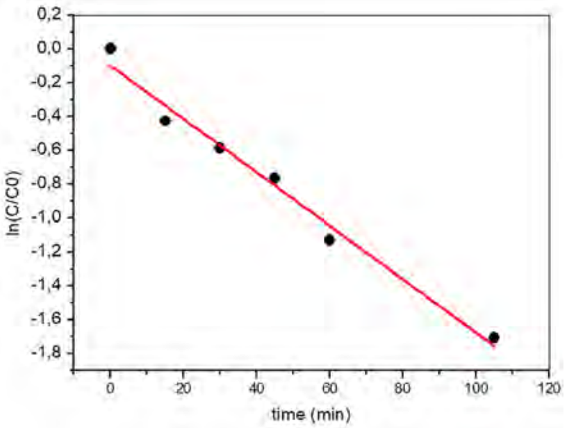

Figure 6. First order kinetic model fitting of MB degradation with Ag_3VO_4

indicate whether the experimental conditions have effect on the degradation. As seen from the Figure 4, MB blue concentration does not change during the experiment verifying that without catalyst no degradation occurs that stem from the experimental conditions.

For evaluating the effect of Al_2O_3 to the catalytic performance Ag_3VO_4 was tested separately. The change of MB concentration with time was given in Figure 5. The change of ln(C/C_0) with time was also given in Figure 6 to identify the rate constant of degradation. It is clear that MB blue degradation with Ag_3VO_4 lasts longer than that of $MgFe_2O_4$-Al_2O_3/Ag_3VO_4 when Figures 3 and Figure 5 are compared. Figure 6 suggest that degradation kinetics correspond to first order model again. Rate constant of the degradation with Ag_3VO_4 was 0,01577 min^{-1}. Half life was found as 43.9 min.

From the degradation half-lives which are 21.3 min for $MgFe_2O_4$-Al_2O_3/Ag_3VO_4 and 43.9 min for Ag_3VO_4, it is clear that incorporating Al_2O_3 particles to the Ag_3VO_4 acted positively to enhance the photocatalytic activity at least twofold when compared to neat Ag_3VO_4. This effect can be attributed to the adsorption of dye molecules by Al_2O_3. By the help of this adsorption, a pre-concentration of dye molecules near the catalyst is created which accordingly increases the rate of reaction [16]. A photograph of MB degradation with $MgFe_2O_4$-Al_2O_3/Ag_3VO_4 photocatalyst is given in the Figure 7.

The photograph (Figure 7) shows that how efficient does MB degradation take place in the presence of a photocatalyst under visible light. It is also seen that after the completion of reaction, catalyst particles consist of $MgFe_2O_4$ magnetic particles are easily attracted by a magnet without needing extra filtration step.

CONCLUSION

In this study visible active, magnetic $MgFe_2O_4$-Al_2O_3/Ag_3VO_4 photocatalyst was successfully synthesized and tested against MB degradation under visible light illumination by 105 W tungsten light bulb. The study showed that adsorbent (Al_2O_3 particles) adding strategy produced positive result in enhancing the photocatalytic activity of Ag_3VO_4 almost twofold. Reaction rate as inferred from the half life time of degradation with $MgFe_2O_4$-Al_2O_3/Ag_3VO_4 catalyst which is 21.3 min was nearly half of that (43.9 min) with neat Ag_3VO_4. Corresponding reaction rate constants, k for $MgFe_2O_4$-Al_2O_3/Ag_3VO_4 and Ag_3VO_4 were identified as 0.03252 min^{-1} and 0.01577 min^{-1}, respectively. The kinetic model of the MB degradation by these catalyst was well fitted by first order kinetics. The catalyst introduced in this study proved that it can be removed easily from the aqueous solution by a magnet bar due to the magnetic particles of $MgFe_2O_4$ eliminating the difficult conventional separation techniques.

ACKNOWLEDGEMENTS

I want to thank Prof.Dr.Mürüvvet Yurdakoc for valuable helps and to her MSc student Yıldıray Aldemir.

REFERENCES

1. Harraz FA, Abdel-Salam OE, Mostafa AA, Mohamed RM, Hanafy M. Rapid synthesis of titania-silica nanoparticles photocatalyst by a modified sol-gel method for cyanide degradation and heavy metals removal. Journal of Alloys

Figure 7. Photograph of the MB degradation steps under visible light

and Compounds 551 (2013) 1-7.

2. El–Toni AM, Yin S, Sato T, Ghannam T, Al–Hoshan M, Al–Salhi M. Investigation of photocatalytic activity and UV–shielding properties for silica coated titania nanoparticles by solvothermal coating. Journal of Alloys and Compounds 508 (2010) L1-L4.
3. Abbasi A, Ghanbari D, Salavati–Niasari M, Hamadanian M. Photo–degradation of methylene blue: photocatalyst and magnetic investigation of Fe_2O_3-TiO_2 nanoparticles and nanocomposites. Journal of Materials Science: Materials in Electronics 27 (5) (2016) 4800-4809.
4. Guo M, Qianglong H, Wenjie W, Jie W, Weimin W. Fabrication of $BiVO_4$: Effect of structure and morphology on photocatalytic activity and its methylene blue decomposition mechanism, Journal of Wuhan University of Technology–Materials Science Education 31 (4) (2016) 791-798.
5. Umaporn L, Khatcharin W, Sukon P, Wiyong K, Natda W. $InVO_4$-$BiVO_4$ composite films with enhanced visible light performance for photodegradation of methylene blue. Catalysis Today 278 (2) (2016) 291–302.
6. Cheng L, Kang Y. Bi_5O_7I/Bi_2O_3 composite photocatalyst with enhanced visible light photocatalytic activity. Catalyst Communucations 72 (2015) 16–19.
7. Shi S, Gondal MA, Rashid SG, Qi Q, Al–Saadi AA, Yamani ZH. Synthesis of g–C_3N_4/$BiOCl_xBr_{1+x}$ hybrid photocatalysts and the photoactivity enhancement driven by visible light. Colloids Surface A: Physicochemical Engineering Aspects 461 (2014) 202-11.
8. Song S, Chenga B, Wu N, Meng A, Cao S, Yu J. Structure effect of graphene on the photocatalytic performance of plasmonic Ag/Ag_2CO_3–rGO for photocatalytic elimination of pollutants. Applied Catalysis B: Environmental 181 (2016) 71-78.
9. Jin Z, Murakami N, Tsubota T, Ohno T. Complete oxidation of acetaldehyde over a composite photocatalyst of graphitic carbon nitride and tungsten(VI) oxide under visible–light irradiation. Applied Catalysis B: Environmental 150-151 (2014) 479-485.
10. Mohsen P. Visible–light photoactive Ag-AgBr/α–Ag_3VO_4 nanostructures prepared in a water–soluble ionic liquid for degradation of wastewater. Applied Nanoscience 6 (2016), 1119-1126.
11. Ming Y, Yilin W, Yan Y, Xu Y, Fangfang Z, Yinqun H, and Weidong S. Synthesis and Characterization of Novel $BiVO_4$/Ag_3VO_4 Heterojunction with Enhanced Visible–Light–Driven Photocatalytic Degradation of Dyes. ACS Sustainable Chemistry & Engineering 4 (3) (2016) 757-766.
12. Hui X, Huaming L, Li X, Chundu W, Guangsong S, Yuanguo X, Jinyu C. Enhanced Photocatalytic Activity of Ag_3VO_4 Loaded with Rare–Earth Elements under Visible–Light Irradiation. Industrial Engineering Chemistry Research 48 (24) (2009) 10771-10778.
13. Lei G, Zhonghua L, Jiawen L. Facile synthesis of Ag_3VO4/β–$AgVO_3$ nanowires with efficient visible–light photocatalytic activity. RSC Advances 7 (2017) 27515–27521.
14. Tingting Z, Liying H, Yanhua S, Zhigang C, Haiyan J, Yeping L, Yuanguo X, Qi Z, Hui X, Huaming L. Modification of Ag_3VO_4 with graphene–like MoS_2 for enhanced visible–light photocatalytic property and stability. New Journal of Chemistry 40 (2016) 2168–2177.
15. Ran R, Meng XC, Zhang ZS, Facile preparation of novel graphene oxide–modified Ag_2O/Ag_3VO_4/$AgVO_3$ composites with high photocatalytic activities under visible light irradiation. Applied Catalysis B: Environmental 196 (2016) 1–15.
16. Carl A, Allen JB. Improved Photocatalytic Activity and Characterization of Mixed TiO_2/SiO_2 and TiO_2/Al_2O_3 Materials. Journal of Physical Chemistry B 101 (1997) 2611–2616.
17. Iliya A, Maryam M, Nahid R. $MgFe_2O_4$ and $MgFe_2O_4$/$ZnFe_2O_4$ coated with polyaniline as a magnetically separable photocatalyst for removal of a two dye mixture in aqueous solution. Research on Chemical Intermediates 43 (2017) 4459–4474.
18. Nabiyouni G, Ghanbari D, Ghasemi J, Yousofnejad A. Microwave–assisted Synthesis of $MgFe_2O_4$–ZnO Nanocomposite and Its Photocatalyst Investigation in Methyl Orange Degradation. Journal of Nano Structures 5(3) (2015) 289–295.
19. Wang J, Wang P, Cao Y, Chen J, Li W, Shao Y, Zheng Y, Li D. A high efficient photocatalyst Ag_3VO_4/TiO_2/graphene nanocomposite with wide spectral response. Applied Catalysis B. Environmental 136-137 (2013) 94-102.
20. Sheykhan M, Mohammadnejad H, Akbari J, Heydari A. Superparamagnetic magnesium ferrite nanoparticles: a magnetically reusable and clean heterogeneous catalyst. Tetrahedron Letters 53 (2012) 2959-2964.
21. Zhang L, He Y, Ye P, Wu T, Enhanced photodegradation activity of Rhodamine B by $MgFe_2O_4$/Ag_3VO_4 under visible light irradiation. Catal Communications 30 (2013) 14–18.
22. Phaltane AS, Vanalakar SA, Bhat TS, Patil PS, Sartale SD, Kadam LD. Photocatalytic degradation of by hydrothermally synthesized CZTS nanoparticles. Journal of Materials Science: Materials in Electronics 28 (2017) 8186-8191.
23. Hassena H. Photocatalytic Degradation of by Using Al_2O_3/Fe_2O_3 Nano Composite under Visible Light. Modern Chemistry & Applications 4(1) (2016) 1–5.
24. Khataee AR, Fathinia M, Aber S. Kinetic Modeling of Liquid Phase Photocatalysis on Supported TiO_2 Nanoparticles in a Rectangular Flat–Plate Photoreactor. Industrial Engineering and Chemistry Research 49 (2010) 12358-12364.
25. Jiamei W, Can L, Hong Z, Jianhao Z. Photocatalytic degradation of methylene blue and inactivation of gram–negative bacteria by TiO_2 nanoparticles in aqueous suspension. Food Control 34 (2013) 372–377.
26. Yıldıray A, Magnetik özellikli taşıyıcılı nanokatalizörlerin hazırlanması ve karakterizasyonu, Yüksek Lisans Tezi, Dokuz Eylül Üniversitesi, İzmir, 2016.
27. Sheykhan M, Mohammadnejad H, Akbari J, Heydari A. Superparamagnetic magnesium ferrite nanoparticles: A magnetically reusable and clean heterogeneous catalyst. Tetrahedron Letters 53 (2012) 2959-2964.
28. Khot VM, Salunkhe AB, Thorat ND, Phadatare MR, Pawar SH. Induction heating studies of combustion synthesized $MgFe_2O_4$ nanoparticles for hyperthermia applications. Journal of Magnetism and Magnetic Materials 332 (2013) 48–51.
29. Hoque SM, Hakim MA, Mamun A, Akhter S, Hasan MT, Paul DP. Study of the bulk magnetic and electrical properties of $MgFe_2O_4$ synthesized by chemical method. Materials Sciences and Applications 2 (2011) 1564.

Hittite Journal of Science and Engineering, 2018, 5 (1) 19-24
ISSN NUMBER: 2148-4171
DOI:10.17350/HJSE19030000073

Failure Analysis of Graphene Sheets with Multiple Stone-Thrower-Wales Defects Using Molecular-Mechanics Based Nonlinear Finite Element Models

Cengiz Baykasoglu[1], **Ata Mugan**[2]
[1]Hitit University, Department of Mechanical Engineering, Corum, TURKEY
[2]Istanbul Technical University, Department of Mechanical Engineering, Istanbul, TURKEY

ABSTRACT

Experimental studies show that Stone-Thrower-Wales (STW) defects generally exist in graphene sheets (GSs) and these defects considerably affect the fracture strength of GSs. Thus, prediction of failure modes of GSs with STW defects is useful for design of graphene based nanomaterials. In this paper, effects of multiple STW defects on fracture behavior of GSs are investigated by employing molecular mechanics based nonlinear finite element models. The modified Morse potential is used to define the non-linear characteristic of covalent bonds between carbon atoms and geometric nonlinearity effects are considered in models. Different tilting angles of STW defects are considered in simulations. The analysis results showed that the fracture strength of GSs strongly depends on tilting angle of multiple STW defects and the STW defects cause significant strength loss in GSs. The crack initiation and propagation are also studied and brittle failure characteristics are observed for all samples. The results obtained from this study provide some insights into design of GS based-structures with multiple STW defects.

Article History:
Received: 2017/04/04
Accepted: 2017/06/09
Online: 2017/12/26

Correspondence to*: Cengiz Baykasoglu*
Hitit University, Department of Mechanical Engineering, Cevre Yolu Avenue, 19030, Corum, Turkey
Tel: +90 (364) 227-45-33
E-Mail:cengizbaykasoglu@hitit.edu.tr

Keywords:
Graphene sheet, Stone-Thrower-Wales (5-7-7-5) defects, Fracture, Tilting angle, Molecular mechanic

INTRODUCTION

Graphene sheet (GS) can be defined as a two-dimensional (2-D) sheet of covalently bonded carbon atoms arranged in a honeycomb lattice structure [1]. GSs have been considered as one of the most promising material for technological applications in many areas [2,3] due to its unique mechanical, thermal, electronic, and other physical properties [4-8]. On the other hand, mass production of ideal GSs is very challenging and many kinds of defects such as vacancy and Stone-Thrower-Wales (STW, 5-7-7-5) may emerge during manufacturing processes or may be induced due to stress [9-14]. At this point, several studies reveal that vacancy and STW defects significantly affect the fracture behavior of GSs [15, 16]. Thus, prediction of fracture characteristic of GSs with different kinds of defects is very crucial for design of graphene based nanomaterials.

Physical or experimental measurements for prediction of fracture behavior of carbon-based nanostructures are very limited due to challenges associated with designing experiments at the nanoscale. Thus, computational modelling approaches are widely used to investigate fracture behavior of these structures. At this point, atomistic modelling approaches such as Molecular Dynamics (MD) and Molecular Mechanics (MM) methods are commonly used to investigate the mechanical performance of defected GSs and carbon nanotubes (CNTs) [15-25]. Relevant works in literature are summarized as follows. Troya et al. [20] investigated effects of STW defects on failure stress of CNTs by using Quantum Mechanics (QM) method. Chandra et al. [21] examined local elastic properties of CNTs having STW defects. In another study, Mielke et al. [22] predicted the fracture strain and stress of STW-defected CNTs using MD and QM methods. Belytschko et al. [23] studied failure behavior of STW defected CNTs using atomistic simulations. Besides, Wang et al. [24] studied the failure of vacancy and STW defected GSs using MD simulations. Furthermore, He et al. [25] studied the effects of multiple STW defects on the mechanical performance of GSs employing MD simulations. All aforementioned atomistic studies [20-25] showed that the presence of STW defects negatively affect the mechanical performance of CNTs and GSs.

On the other hand, in spite of their accuracy, QM and MD approaches are computationally very expensive and not suitable for modeling large scale models. Hence, MM based modeling approaches have been widely used to investigate mechanical properties of defected graphene based structures due to their computational efficiencies [26-34]. These approaches construct a bridge between the MM and continuum mechanics by energy equivalence [35-37]. In a typical MM based model, the covalent bonds between carbon atoms are simulated using different kinds of structural elements such as springs, beams and rods [26-37]. Relevant MM based modeling studies are summarized as follows: Tserpes et al. [26] developed a Finite Element (FE) based failure model to examine the failure behavior of pristine and vacancy-defected CNTs. Tserpes et al. [27] also examined the effects of STW-defects on the fracture performance of CNTs and the reduction in failure strength is predicted in the range of range 18 to 25 %. Xiao et al. [28] used an atomistic based FE approach to predict failure behavior of STW- defected GSs and CNTs and the reduction in failure strength is predicted in the range of 12 to 32 %. Besides, Xiao et al. [29] also examined the tensile behavior of GSs and CNTs having multiple STW defects. Moshrefzadeh-Sani et al. [30] proposed a continuum model for STW-defected CNTs in which an STW defect is replaced by a crack with a definite length. Furthermore, Wang et al. [31] examined the mechanical properties of graphene nanofilms having STW defects using atomistic mechanics based FE models. Morever, we developed MM based nonlinear FE models and examined failure behavior of GSs and CNTs [32-34].

Although there are some published works about failure behavior of STW-defected GSs and CNTs, only a few studies are initiated to investigate fracture behavior of multiple STW-defected GSs [25, 29]. On the other hand, there is no comparative study on the fracture behavior of multiple STW defected-GSs by the use of MM based nonlinear FE models. Motivated by these facts, the fracture properties of multiple STW defected GSs are investigated using MM based nonlinear FE models in which both geometric and material nonlinearities are considered. Different tilting angles which are the angle between tensile direction and axis of STW defects are considered in simulations. The analysis results reveal that the tilting angle has a significant effect on fracture behavior of GSs and the STW defects considerable affect the failure behavior of GSs. Besides, the fracture initiation and propagation patterns are also examined and diagonal crack propagation patterns are observed for all cases. The brittle fracture characteristics are also observed for STW defected-GSs

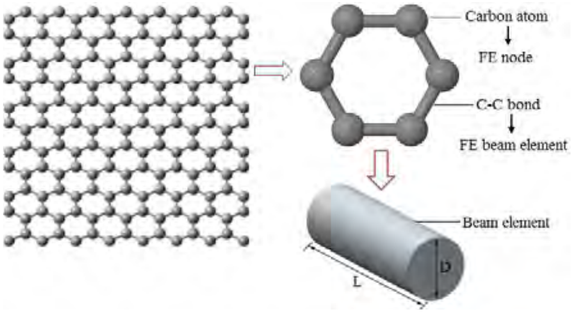

Figure 1. FE modeling of graphene

COMPUTATIONAL METHODOLOGY

We already developed a MM based nonlinear FE model to investigate failure behavior of carbon based nanostructures (e.g., CNTs and GSs) in our previous works [32-34]. In this study, the similar approach with Refs. [32-34] is employed to examine fracture behavior of multiple STW-defected GSs. Namely, 2-D Euler–Bernoulli (EB) beam elements are used to model bonds between carbon atoms and the characteristic of C-C bonds are simulated by employing the modified Morse interatomic potential (i.e., Fig. 1).

Nonlinear geometric effects are also included in the models. At this point, incremental displacement loading is applied to zigzag direction of GSs (i.e. Fig. 3), stiffness of the EB elements are calculated using the proposed atomistic potential and updated with the atomic positions at each incremental loading step. The stiffness matrix of 2-D EB beam element is given as [38]

$$\mathbf{K} = \begin{bmatrix} \frac{EA}{L} & 0 & 0 & -\frac{EA}{L} & 0 & 0 \\ 0 & \frac{12EI}{L^3} & \frac{6EI}{L^2} & 0 & -\frac{12EI}{L^3} & \frac{6EI}{L^2} \\ 0 & \frac{6EI}{L^2} & \frac{4EI}{L} & 0 & -\frac{6EI}{L^2} & \frac{2EI}{L} \\ -\frac{EA}{L} & 0 & 0 & \frac{EA}{L} & 0 & 0 \\ 0 & -\frac{12EI}{L^3} & -\frac{6EI}{L^2} & 0 & \frac{12EI}{L^3} & -\frac{6EI}{L^2} \\ 0 & \frac{6EI}{L^2} & \frac{2EI}{L} & 0 & -\frac{6EI}{L^2} & \frac{4EI}{L} \end{bmatrix} \qquad (1)$$

where E is the elasticity modulus, A is the cross-sectional area of beam element, I is the inertia moment and L is the initial length of a covalent bond. The initial secant modulus of EB beam elements is taken as 6.93 TPa which is calculated from the stress (σb) – strain (εb) curve of covalent bond using the modified Morse potential [32]. The geometric parameters of beam elements are given in Table 1.

Table 1. Geometric parameters of the EB beam element [39].

Thickness of beam , D	1.47 Å
Cross-sectional area of beam, A	1.687 Å^2
Moment of inertia of beam, I	0.22682 Å^4
Initial length of beam, L	1.421 Å

Table 2. The modified Morse potential parameters [23].

r_o	1.421 Å	ϑo	2.094 rad
β	2.625 $Å^{-1}$	$k\vartheta$	0.9 x 10^{-8} NÅ/rad^2
D_e	6.03105 x 10^{-9} NÅ	k_{sextic}	0.754 $Å^4$

The atomistic interactions are basically governed by the bond stretching and bond angle-bending terms for in-plane deformations problems of GSs. Hence, the modified Morse potential includes bond stretching (Ur) and angle-bending (Uθ) energy terms as given by

$$U_{total} = \sum U_r + \sum U_\theta \tag{2}$$

$$U_r = D_e \left\{ \left[1 - e^{-\beta(r-r_0)} \right]^2 - 1 \right\} \tag{3}$$

$$U_\theta = \frac{1}{2} k_\theta (\theta - \theta_0)^2 + \left[1 + k_{sextic} (\theta - \theta_0)^4 \right] \tag{4}$$

where r is the current C-C bond length, θ is the current angle of adjacent bond, β is the constant which controls the width of potential and De denotes the dissociation energy. The parameters of the modified Morse potential are presented in Table 2. Detailed information on the modified Morse potential and its parameters can be found in [23].

The bond stretching (Ur) term has the dominant effect on fracture behavior of GSs. Hence, the angle-bending term (i.e. Eq. 4) is neglected in analyses as done by the following references [26, 27, 32-34, 40]. By differentiating Eq. 3 by respect to bond length (r), the stretching force of C-C bonds is defined as follows:

$$F = 2\beta D_e \left(1 - e^{-\beta(r-r_0)}\right) e^{-\beta(r-r_0)} \tag{5}$$

Fig. 2 shows the relationship between force and bond strain for the covalent bond between carbon atoms. Belytschko et al. [23] investigated the fracture behavior of CNTs and reported that the fracture depends mainly on the inflection point of interatomic potential. Thus, after the inflection point, the shape of the modified Morse potential function is not critical since material damage takes place. Similarly, in this study, the cut-off distance value of 1.69 Å which corresponds to the inflection point at approximately 19 % strain (i.e. see Fig. 2) is employed in analysis. Beyond this value, the shape of the modified Morse potential is not critical because bond fracture occurs [23].

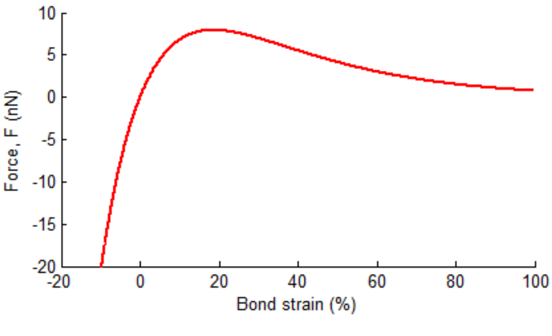

Figure 2. Force-strain curve of modified Morse interatomic potential

Geometries of STW-defected GS models are constructed using a Matlab code. Sufficiently large GS models are used in analyses in order to prevent the end effects. Finally, the GSs models having the dimensions of 125.52 x 126.46 is employed in analysis. The models contain 6180 atoms and 9159 covalent bonds. The details about the modeling approach and update procedure can be found in [32, 33]. Fig. 3 shows the proposed STW-defected GS model.

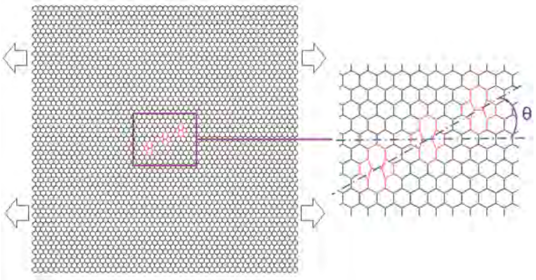

Figure 3. The defected GSs having three STW-defects and definition of the tilting angle

RESULTS AND DISCUSSION

In numerical models, all the atoms (i.e., nodes) at the one end (in this study, armchair edge) of GSs are fixed and the incremental displacement loading is applied to the atoms at the other end. The stiffness and nodal positions (atomic positions) of each element (i.e., bond) are updated at each incremental loading step. Stress- strain curve of the C-C bond are shown in Fig. 4.

When a bond breaks, then its stiffness matrix is multiplied by a very small number to simulate bond breaking phenomena. The total strain and stress are respectively calculated using the following equations:

$$\varepsilon = \frac{(L - L_0)}{L_0}, \quad \sigma = \frac{F}{wt} \tag{6}$$

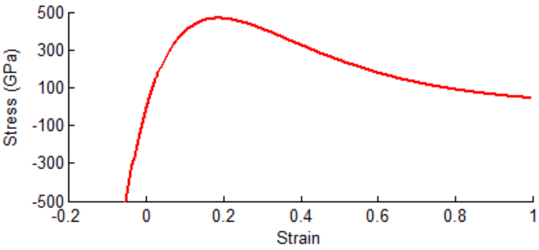

Figure 4. Stress- strain curve of C-C bond

where, L is the current length, L_0 is the initial length, w is the width, t is the thickness of the GSs and F is the applied tensile force which is calculated by summing of the reaction forces at the fixed nodes. The thickness of the GSs is considered as 3.4 Å. In addition, strain increment of 0.1 % is employed in the analyses. In which, we assume that one STW defect is located in the middle of the GSs and other two STW defects are located around the middle defects. Different tilting angle are considered in analyses and the distance between the STW defects is selected to be constant (i.e. Fig. 3).

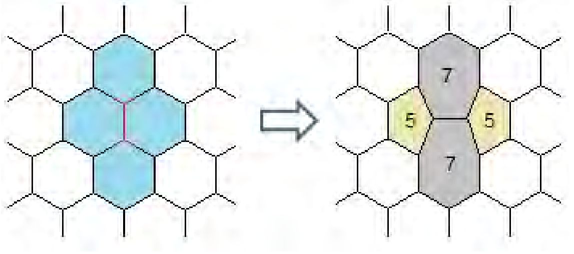

Figure 5. Schematic model showing the transformation of four adjacent hexagons into STW defect

The STW (5-7-7-5) is a topological defect [41,42] and may be induced due to stress. Namely, when GSs are subjected to tensile loading, GSs release their excess tension via formation of STW defects. Nardelli et al. [13, 14] pointed out that defect nucleation happens via STW transformation at the strain of 5% in armchair CNTs and somewhat later in GSs. Besides, Zhang et al. [43] showed that the STW transformation happens at strain of 6 % for armchair CNTs. In this work, we proposed critical strain for the formation of the STW defects as 6 %. At this point, we used the pristine GSs up to critical strain of 6 % and then, the corresponding bond configurations are modified at this formation strain. After STW transformation occurs, four hexagons change into two heptagons and two pentagons. The total number of the atoms does not change in this transformation. Fig. 5 shows schematic representation of STW (5-7-7-5) formation. Also note that, after the STW transformation occurs, a prestrain is employed to minimize energy configuration of atoms and calculation is continued until fracture happens.

Fig. 6 illustrates stress–strain curves of some selected multiple STW-defected GSs for different tilting angles. It can be observed in Fig. 6 that the failure stress and failure strain values of defect-free (pristine) GSs (which are respectively 102.15 GPa and 0.174) reduced by the presence of STW-defects due to the stress concentration in vertical bonds that occurs after bond rearrangement. Hence, more STW defects may cause higher stress concentration at the multiple STW defects areas. The fracture stress of pristine GSs the reduced by 19.5- 29.2 %, if three STW defects exist in the GS structure. It is also seen in Fig. 6 that the fracture stress of GSs decreases with the increasing tilting angle. Namely, the fracture stress value of multiple STW-defected GSs having the tilting angle of 0° is approximately 14 % higher than STW-defected GSs having the tilting angle of 83.4°. He et al. [25] predicted that the fracture strength value of two STW-defected GSs having the tilting angle of 0° is approximately 14.1 % higher than that of 83.4°. Thus, our prediction is in good agreement with the MD simulation result in Ref. [25].

On the other hand, as can be observed in Fig. 6, the stress curve suddenly drops to zero when the stress reaches to a certain value. Thus, it is concluded that the failure of pristine and defected GSs are brittle type which is in good agreement with the results of [23-28].

Fig. 7 shows the fracture stress of STW-defected GSs having different tilting angles. In addition, the fracture stress value of one STW-defected GS (i.e., 77.88 GPa) is also given in Fig. 7. It is observed that the fracture stresses of multiple STW- defected GSs are higher than that of one STW defected GS when titling angle is smaller than approximately 45°. It is also observed that the reduction of the fracture stress values in the range 30° < θ < 60° is higher than other angle ranges. He et al. [25] showed that the ultimate strength of graphene sheets decreases much slower when the angle is larger than 55.4°. Hence, our prediction is in good agreements with the MD result of Ref. [25].

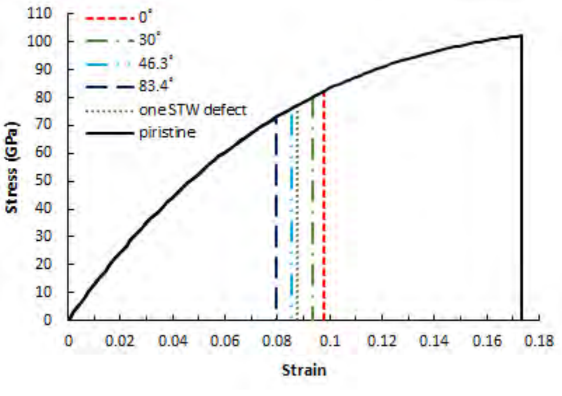

Figure 6. Tensile stress–strain curves of GSs having STW-defects

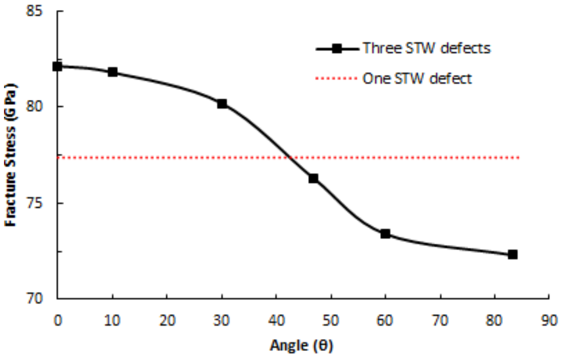

Figure 7. Comparison of the fracture stress of multiple STW-defected GSs for different tilting angles with the one STW-defected GS

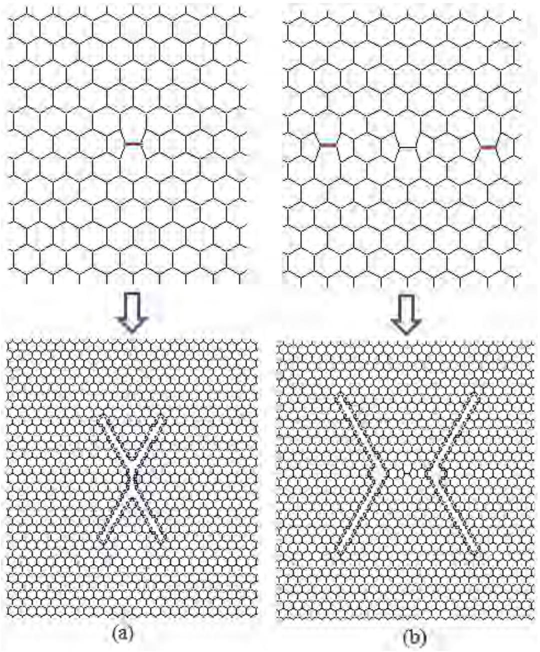

Figure 8. Fractured profile of the one (left) and multiple STW-defected GS (tilting angle of 0°) (right) under tension

The fracture initiation and post failure characteristic of STW-defected GSs can be predicted by employing the proposed approach. Fig. 8 shows the crack initiation and propagation directions (deletion of failed bonds based on the proposed failure criterion) of one and multiple STW-defected GS. As can be seen in Fig. 8a, for the GSs with one STW defect, the first bond fracture is initiated from the longitudinal bond which connects the two pentagons. Then, the fracture propagated in the ±45° maximum shear stress directions. The similar propagation patterns are also observed in Ref. [23, 28] for STW defected graphitic structures. On the other hand, as can be observed in Fig. 8b that the failure initiated from the right and left horizontal bonds of GS having three STW defects (i.e., represented in red color) and continued along the diagonal crack paths similar to the one STW defected sample. This prediction is reasonable since stresses are concentrated at the left and right STW-defected regions and the no bond failure is observed in the region around the middle STW-defect. Once first bond failure initiated, stresses are concentrated on the diagonal neighboring bonds causing subsequent fractures. The similar fracture patterns are also observed for other tilting angles. This failure patterns which shown in Fig. 8 is also in good agreement with the results in Ref. [23,29].

CONCLUSION

In this paper, the fracture behavior of multiple STW-defected GSs is investigated using MM based nonlinear finite element models. The effect of tilting angle on fracture characteristic of GS is also investigated in the analyses. The results show that multiple STW defects cause significant reduction in strength values of the GS structures. Namely, the strength of pristine GSs is reduced by 19.5- 29.2 % if three STW defects exist in the structure. It is observed that the tilting angle (θ) is also an important geometric parameter and strongly affects the fracture strength of GSs. Higher reduction in fracture strength is observed in the range 30° < θ < 60°. Besides, crack initiation and propagation are examined. It is concluded that the failure of GSs are in a brittle manner.

REFERENCES

1. Meyer, J. C., Geim, A. K., Katsnelson, M. I., Novoselov, K. S., Booth, T. J., & Roth, S. The structure of suspended graphene sheets. Nature 446(7131) (2007) 60–63.
2. Huang, X., Yin, Z., Wu, S., Qi, X., He, Q., Zhang, Q., Yang, Q., Boey, F., & Zhang, H. Graphene–based materials: synthesis, characterization, properties, and applications. Small 7(14) (2011) 1876–1902.
3. Avouris, P., & Dimitrakopoulos, C. Graphene: synthesis and applications. Materials today 15(3) (2012) 86–97.
4. Lee, C., Wei, X., Kysar, J. W., & Hone, J. Measurement of the elastic properties and intrinsic strength of monolayer graphene. Science 321(5887) (2008) 385–388.
5. Neto, A. C., Guinea, F., Peres, N. M. R., Novoselov, K. S., & Geim, A. K. The electronic properties of graphene. Reviews of modern physics 81(1) (2009) 109.
6. Pop, E., Varshney, V., & Roy, A. K. Thermal properties of graphene: Fundamentals and applications. MRS bulletin 37(12) (2012) 1273–1281.
7. Civalek, Ö., & Akgöz, B. Vibration analysis of micro–scaled sector shaped graphene surrounded by an elastic matrix. Computational Materials Science 77 (2013) 295–303.
8. Akgöz, B., & Civalek, Ö. Free vibration analysis for single–layered graphene sheets in an elastic matrix via modified couple stress theory. Materials & Design 42 (2012) 164–171.
9. Banhart, F., Kotakoski, J., & Krasheninnikov, A. V. Structural defects in graphene. ACS nano 5(1) (2010) 26–41.
10. Lee, G. D., Wang, C. Z., Yoon, E., Hwang, N. M., Kim, D. Y., & Ho, K. M. Diffusion, coalescence, and reconstruction of vacancy defects in graphene layers. Physical review letters 95(20) (2005) 205501.
11. Lusk, M. T., & Carr, L. D. Creation of graphene allotropes using patterned defects. Carbon 47(9) (2009) 2226–2232.
12. Sun, Y. J., Ma, F., Ma, D. Y., Xu, K. W., & Chu, P. K. Stress–induced annihilation of Stone–Wales defects in graphene nanoribbons. Journal of Physics D: Applied Physics 45(30) (2012) 305303.
13. Nardelli, M. B., Yakobson, B. I., & Bernholc, J. Mechanism of strain release in carbon nanotubes. Physical Review B 57(8) (1998) R4277.
14. Nardelli, M. B., Yakobson, B. I., & Bernholc, J. Brittle and ductile behavior in carbon nanotubes. Physical review letters 81(21) (1998) 4656.
15. Zhang, T., Li, X., & Gao, H. Fracture of graphene: a review. International Journal of Fracture 1–31 (2015).
16. Xu, L., Wei, N., & Zheng, Y. Mechanical properties of highly defective graphene: from brittle rupture to ductile fracture.

Nanotechnology 24(50) (2013)505703.

17. Cao, G. Atomistic studies of mechanical properties of graphene. Polymers 6(9) (2014) 2404–2432.
18. Ansari, R., Motevalli, B., Montazeri, A., & Ajori, S. Fracture analysis of monolayer graphene sheets with double vacancy defects via MD simulation. Solid State Communications 151(17) (2011) 1141–1146.
19. Yanovsky, Y. G., Nikitina, E. A., Karnet, Y. N., & Nikitin, S. M. Quantum mechanics study of the mechanism of deformation and fracture of graphene. Physical Mesomechanics 12(5) (2009) 254–262.
20. Troya, D., Mielke, S. L., & Schatz, G. C. Carbon nanotube fracture-differences between quantum mechanical mechanisms and those of empirical potentials. Chemical Physics Letters 382(1) (2003) 133–141.
21. Chandra, N., Namilae, S., & Shet, C. Local elastic properties of carbon nanotubes in the presence of Stone–Wales defects. Physical Review B 69(9) (2004) 094101.
22. Mielke, S. L., Troya, D., Zhang, S., Li, J. L., Xiao, S., Car, R., Ruoff, R.S., Schatz, G. C., & Belytschko, T. The role of vacancy defects and holes in the fracture of carbon nanotubes. Chemical Physics Letters 390(4) (2004) 413–420.
23. Belytschko, T., Xiao, S. P., Schatz, G. C., & Ruoff, R. S. Atomistic simulations of nanotube fracture. Physical Review B 65(23) (2002) 235430.
24. Wang, M. C., Yan, C., Ma, L., Hu, N., & Chen, M. W. Effect of defects on fracture strength of graphene sheets. Computational Materials Science 54 (2012) 236–239.
25. He, L., Guo, S., Lei, J., Sha, Z., & Liu, Z. The effect of Stone-Thrower-Wales defects on mechanical properties of graphene sheets-A molecular dynamics study. Carbon 75 (2014) 124–132.
26. Tserpes, K. I., Papanikos, P., & Tsirkas, S. A. A progressive fracture model for carbon nanotubes. Composites Part B: Engineering 37(7) (2006) 662–669.
27. Tserpes, K. I., & Papanikos, P. The effect of Stone-Wales defect on the tensile behavior and fracture of single–walled carbon nanotubes. Composite Structures 79(4) (2007) 581–589.
28. Xiao, J. R., Staniszewski, J., & Gillespie, J. W. Fracture and progressive failure of defective graphene sheets and carbon nanotubes. Composite structures 88(4) (2009) 602–609.
29. Xiao, J. R., Staniszewski, J., & Gillespie, J. W. Tensile behaviors of graphene sheets and carbon nanotubes with multiple Stone-Wales defects. Materials Science and Engineering: A, 527(3) (2010) 715–723.
30. Moshrefzadeh–Sani, H., Saboori, B., & Alizadeh, M. A Continuum Model For Stone–wales Defected Carbon Nanotubes. International Journal of Engineering–Transactions C: Aspects 28(3) (2015) 433.
31. Wang, S. P., Guo, J. G., & Zhou, L. J. Influence of Stone-Wales defects on elastic properties of graphene nanofilms. Physica E: Low–dimensional Systems and Nanostructures 48 (2013) 29–35.
32. Baykasoglu, C., & Mugan, A. Nonlinear fracture analysis of single–layer graphene sheets. Engineering Fracture Mechanics 96 (2012) 241–250.
33. Baykasoglu, C., Kirca, M., & Mugan, A. Nonlinear failure analysis of carbon nanotubes by using molecular–mechanics based models. Composites Part B: Engineering 50 (2013) 150–157.
34. Baykasoglu, C., & Mugan, A. Coupled molecular/continuum mechanical modeling of graphene sheets. Physica E: Low–dimensional Systems and Nanostructures 45 (2012) 151–161.
35. Odegard, G. M., Gates, T. S., Nicholson, L. M., & Wise, K. E. Equivalent–continuum modeling of nano–structured materials. Composites Science and Technology 62(14) (2002) 1869–1880.
36. Li, C., & Chou, T. W. A structural mechanics approach for the analysis of carbon nanotubes. International Journal of Solids and Structures 40(10) (2003) 2487–2499.
37. Baykasoglu, C., & Mugan, A. Dynamic analysis of single–layer graphene sheets. Computational Materials Science 55 (2012) 228–236.
38. Liu, G. R., & Quek, S. S. The finite element method: a practical course. Butterworth–Heinemann, 2013.
39. Tserpes K I and Papanikos P. Finite element modeling of single–walled carbon nanotubes Composites Part B 36 (2005) 468-477.
40. Baykasoglu, C., Icer, E., Celebi, A. T., & Mugan, A. Nonlinear fracture analysis of carbon nanotubes with stone–wales defects, 3rd South–East European Conference on Computational Mechanics, SEECCM 2013; Kos Island; Greece; 12 June 2013, (2013) 446–454.
41. Stone, A. J., & Wales, D. J. Theoretical studies of icosahedral C 60 and some related species. Chemical Physics Letters, 128(5) (1986) 501–503.
42. Thrower, P.A. The study of defects in graphite by transmission electron microscopy. Chemistry and Physics of Carbon 5 (1969) 217-320.
43. Zhang, P., Lammert, P. E., & Crespi, V. H. Plastic deformations of carbon nanotubes. Physical Review Letters, 81(24) (1998) 5346.

Hittite Journal of Science and Engineering, 2018, 5 (1) 25-29
ISSN NUMBER: 2148-4171
DOI: 10.17350/HJSE19030000074

A New Demodulator For Inverse Pulse Position Modulation Technique

Mehmet Sönmez
Osmaniye Korkut Ata University, Department Electrical and Electronics Engineering, Osmaniye, TURKEY

ABSTRACT

Inverse pulse position modulation is one of the modulation techniques for Visible Light Communication (VLC) systems. In this paper, a new demodulator scheme, which is named as Slot Period Detector (SPD), is proposed by using frequency detection technique. The proposed architecture computes the period time for each slot. Thanks to SPD technique, the complexity of I-PPM receiver is dramatically reduced. However, the traditional receiver has better Bit Error Rate (BER) performance than that of proposed SPD structure. The important issue is that whether the proposed receiver is practicable for real-time systems hence, the SPD is implemented on Field Programmable Gate Arrays (FPGA) board to demonstrate an applicable receiver.

Article History:
Received: 2017/05/05
Accepted: 2017/09/30
Online: 2018/03/28

Correspondence to*: Mehmet Sönmez,*
Osmaniye Korkut Ata University,
Department of Electrical and Electronics
Engineering, Osmaniye, TURKEY
E-Mail: mehmetsonmez@osmaniye.edu.tr

Keywords:
I-PPM, Demodulator, Visible light communication

INTRODUCTION

To provide data transmission in indoor communication systems, Visible Light Communication (VLC) is a promising technique which uses Light Emitted Diode technology. On the contrary wireless RF communication systems, VLC systems are generally operated at short distance due to light power of LED. However, VLC can serve with different systems since VLC doesn't affect any electromagnetic interference compared with RF communication systems. The receiver side uses a photodiode to obtain electrical signal from light energy. Therefore, the line of sight is very important issue for VLC systems.

In order to achieve data transmission in the VLC systems, pulse based modulation techniques were proposed in the literature. The On-Off Keying (OOK) is the simplest modulation method in the communication systems. Another modulation technique is the Pulse Position Modulation (PPM) scheme. The PPM scheme has very advantage with respect of BER performance, complexity and bandwidth efficiency. A new PPM scheme, which is named as Variable Pulse Position Modulation (VPPM), was proposed to control brightness of LED by using variable pulse width technique [1]. I-PPM that is one of the PPM types was proposed in [2]. This modulation method was improved by inversing the traditional PPM technique. Therefore, I-PPM scheme consumes further energy compared with traditional PPM technique.

In [3], the overlapping PPM (OPPM) that is integrated with trellis coded modulation was compared with I-PPM and PPM techniques with respect of data transmission rate. That study is theoretically analyzed to performance of modulation schemes. However, a few papers focused on practical design for implementation of PPM technique. The dimming level is very important issue in the V-PPM (Variable-PPM) scheme. A VPPM transmitter architecture was proposed to reduce resource utilization of VPPM technique for adjustable dimming level [4]. A VPPM demodulator scheme was designed without knowledge dimming level. The proposed architecture was implemented on real-time FPGA board [5]. The demodulator was improved to provide a rapid dimming environment in the paper [6]. The target dimming level is determined by step-step to accomplish synchronization hence target dimming level can't be suddenly obtained. In this paper, we propose a new PPM demodulator architecture to reduce complexity of traditional PPM receiver. The proposed scheme is based on period detector. The empty slot is determined by using a slot period detector. Additionally, the demodulator is implemented on real-time FPGA board. The advantages of proposed receiver are explained as follows:

1. In traditional receiver, the signal generator is used to multiply received signal. Hence, the signal generator must be designed for traditional receiver. However, the proposed architecture doesn't consist of signal generator block.
2. In order to determine empty slot, decision block must use the output values of integrators. The input values of integrators are obtained at the output of multipliers' blocks. The multiplier block must be operated at the traditional receiver side. There isn't any multiplication unit in the proposed receiver.

I-PPM TECHNIQUE

This section gives the traditional I-PPM transmitter and receiver schemes. I-PPM signal is obtained by changing position of empty slot. The empty slot is situated on appropriate locate considering to data bits' condition. In order to generate I-PPM signal, one of the most widely used modulator structures is mux-based techniques because mux-based architectures operates using codeword table. In this scheme, the code that matches with the value of data bit is activated at the output of modulator structure. If *i* can be expressed as the decimal equivalent of data bit, an explanation of I-PPM technique can be written as

$$IPPM_i(t) = \begin{pmatrix} 0 & for\, t \in \left[\frac{i}{2^n} T_b, \frac{i+1}{2^n} T_b \right] \\ V & elsewhere \end{pmatrix} \tag{1}$$

where, T_b and n represent one symbol period and bit number in one symbol, respectively. The *i* value signifies decimal equivalent of data bit. As shown in the Fig. 1, the location of empty slot is determined by using decimal equivalent of data bit.

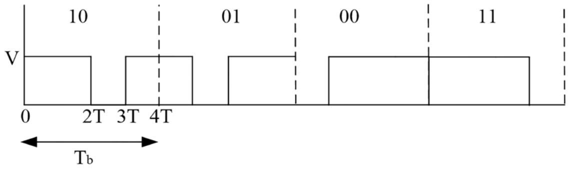

Figure 1. I-PPM signal

In Fig. 2-a, it is shown that traditional I-PPM receiver. As shown in the figure, multiplier and integrator blocks are used to provide correlator-based receiver system. Moreover, signal generator blocks, which are presented as SG-1, SG-2, SG-3 and SG-4, are used to multiply received modulated signal with carrier signal. Firstly, modulated signal is multiplied by carrier signal. Then, the output of multiplication is applied on integrator block which accumulates to received signal through one symbol period. Fig. 2-b gives an example of signal generator architecture. The counter block is used as common block for all SG blocks. The Th-2 and Th-3 are presented as 2T and 3T in Fig. 1, respectively. For interval between 2T and 3T, the algorithm provides that output is being '0'.

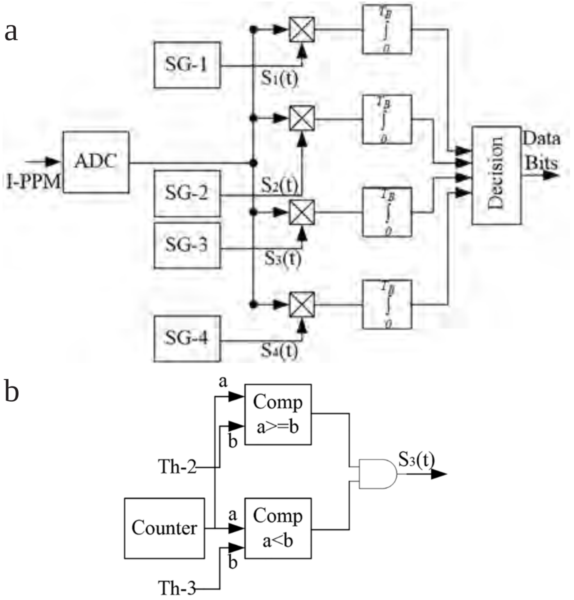

Figure 2. The I-PPM receiver, a. The traditional I-PPM receiver, b. The signal generator architecture.

PROPOSED SLOT PERIOD DETECTOR SCHEME

In this section, we present the proposed demodulator architecture which is referred to as slot period detector (SPD). We count high frequency pulse when amplitude of modulated signal is lower than that of the threshold value which is equal to V/2. The Fig. 3 emphasizes to this situation. As shown in the Fig. 3, empty slot is filled by high frequency pulses because high frequency pulses and the output of comparator block are passed through AND gate. If the amplitude of I-PPM signal is higher than V/2, one of input signals of AND gate is being '1'. This input signal is the output of comparator block. Therefore, the output of AND gate is obtained a square wave. The proposed receiver can be expressed as follows:

$$e = \begin{pmatrix} 0 & for\, IPPM \;=>Th \\ 1 & for\, IPPM \;<Th \end{pmatrix} \tag{2}$$

$$C_k = \sum_{i=1}^{T/4} e_i \tag{3}$$

where, Th and e present threshold value and output of comp (comparator) as shown in Fig. 4. For k ∈ {1, 2, 3, 4}, the output of the counter is presented as Ck. The one symbol period is expressed as T. As shown in the Eq. (2) and (3), the counter computes binary '1' level time during

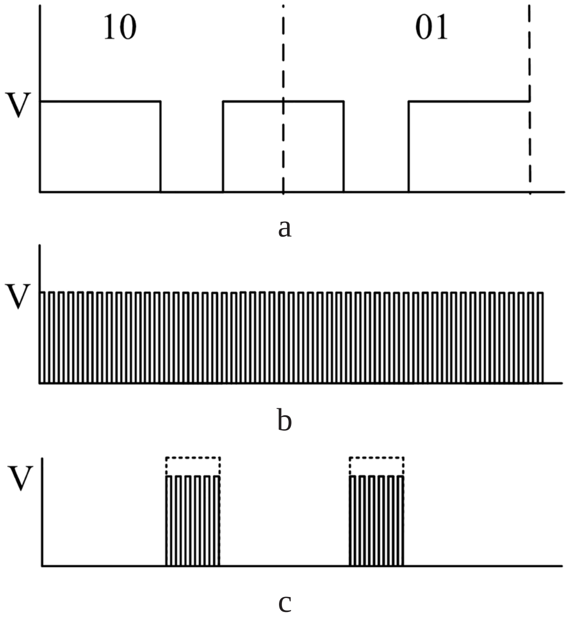

Figure 3. I-PPM demodulation process. (a) I-PPM signal according to data bits. (b) High frequency pulses. (c) AND gate output

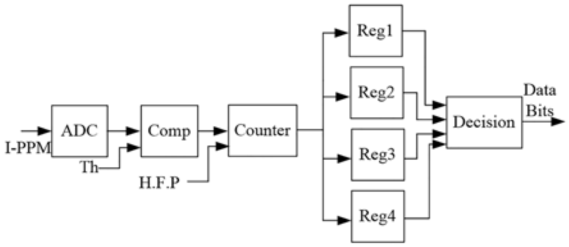

Figure 4. Proposed I-PPM Structure

quarter symbol period. Our aim is to find the maximum Ck among C1, C2, C3 and C4.

In experimental application, the optical I-PPM signal is converted to electrical I-PPM signal by using a photodetector. The electrical I-PPM signal is received by ADC (Analog to Digital Converter). The received modulated signal is compared with a threshold value (Th). This stage determines the structure of received I-PPM signal. The output of comparator block (Comp) acts as an enable signal for counter block. The clock signal of counter block is H.F.P (High Frequency Pulse) hence the output of counter increases when en and H.F.P. is logical '1'. Register (Reg) blocks are used to hold sum value of counter block during quarter symbol period. The decision block determines data bits according to output of register blocks. The filled slot given in the Fig. 3.a is determined by decision block.

SIMULATION AND EXPERIMENTAL RESULTS

In this section, we give simulation and experimental results for proposed demodulator architecture. From experimental and simulation results, we show that proposed serial scheme is suitable for demodulation of I-PPM signal.

The Fig. 5 and Fig. 6 give simulation results of proposed receiver. In the Fig. 5, H.F.P signal is represented as high frequency pulse. The *data*, *g.data* and *d.data* are defined as input data, grouped data and detected data, respectively. The *data* signal is applied on input of I-PPM modulator. In order to generate I-PPM signal, data signal is grouped by two bits because the one symbol consists of two bits. In output of our receiver, the *d.data* is obtained at the output of decision block. The modulated I-PPM signal is successfully demodulated at the receiver side because it is shown from the Fig. 5 that the data and *d.data* bits are same. The *e* signal is generated by comparator block. According to comparison result of I-PPM signal with threshold value, the *e* signal gets '1' or '0'. If threshold value is greater than I-PPM signal, the *e* signal will be '1'; otherwise the *e* signal becomes logic '0'. In the Fig.6, simulation results illustrate BER performance of the traditional (T.D.) and proposed (P.D.) demodulator. As shown in the figure, traditional demodulator has better BER performance than that of proposed demodulator. This is because that the location of empty slot is determined by correlation based receiver.

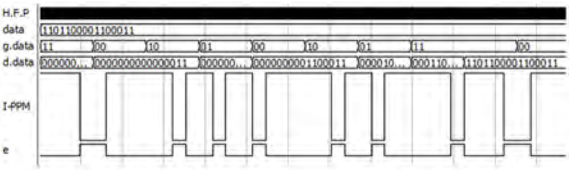

Figure 5. Simulation results of the proposed SPD.

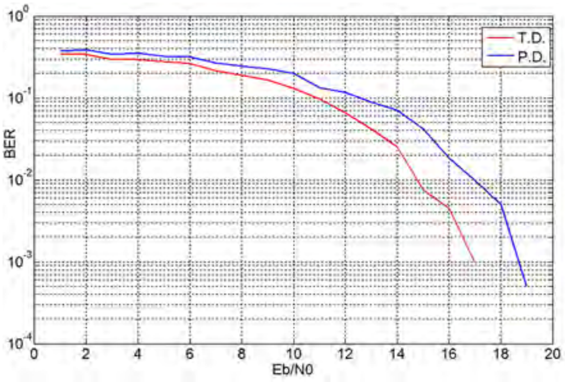

Figure 6. BER performance of the receiver architectures.

The Fig. 7 gives the receiver architecture implemented on FPGA board. We obtain experimental results by oscilloscope. Firstly, we designed modulator and demodulator by using FPGA complier. The designed demodulator is shown in the Fig. 7. Then, we operated on real-time FPGA and observed experimental results on output of the oscilloscope. In Fig. 8 and Fig. 9, we give

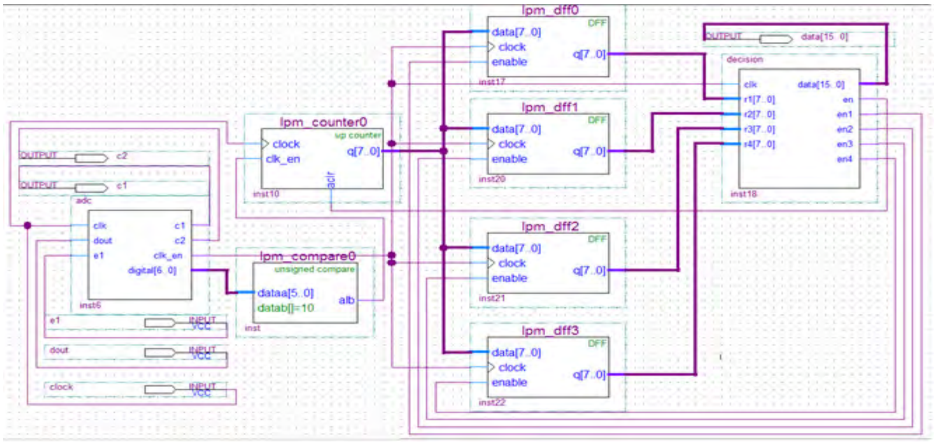

Figure 7. The receiver scheme implemented on FPGA board.

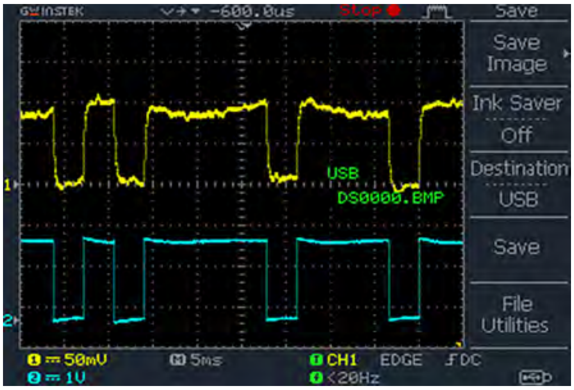

Figure 8. Modulated (blue line) and received (yellow line) signals for low frequency.

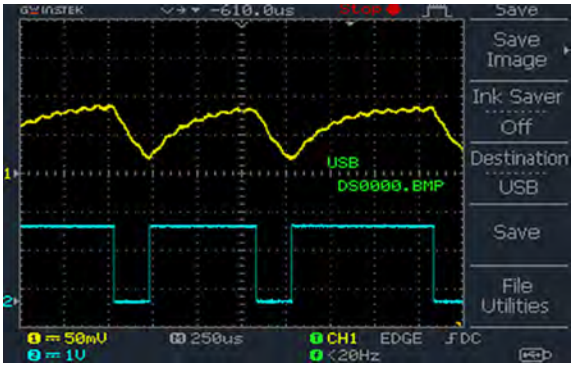

Figure 9. Modulated (blue line) and received (yellow line) signals for higher frequency.

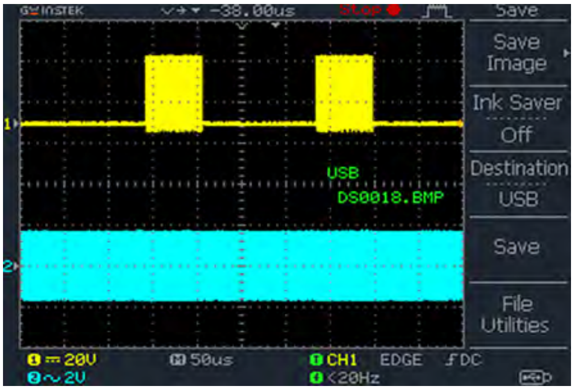

Figure 10. H.F.P (blue line) and clock signal of counter (yellow line).

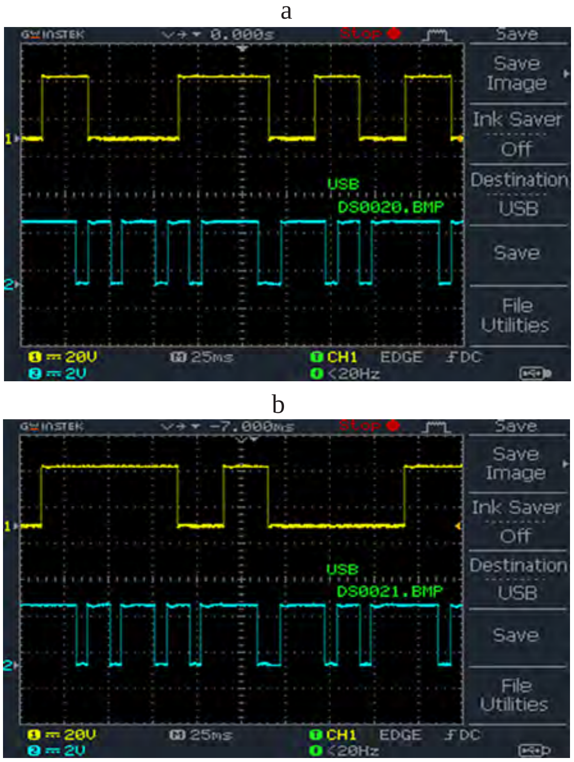

Figure 11. Modulated signals according to data bits. (a) LSB (Yellow Line) and I-PPM (Blue Line) signal. (b) MSB (Yellow Line) and I-PPM (Blue Line) signal.

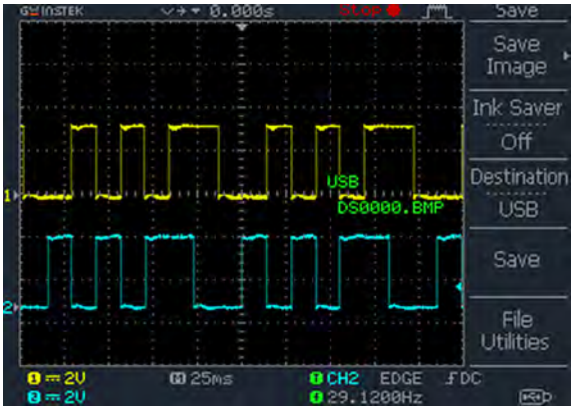

Figure 12. Transmitted (blue line) and received (yellow line) data bits.

modulated signal (blue line) and received signal (yellow line).

In Fig. 8 and Fig. 9, data rate is different hence received signal with higher frequency has further distortion than that of received signal with lower frequency. Fig. 10 shows H.F.P signal (blue line) and clock signal (yellow line) of counter block. The output of counter is increased depending on yellow line signal.

In Fig. 11, we give modulated signal according to data bits. The Fig. 11 (a) illustrates LSB (Least Significant Bit) bit and modulated signal while MSB (Most Significant Bit) and I-PPM signal are shown in Fig. 11 (b).

The Fig. 12 shows received (yellow line) and transmitted (blue line) bits. As shown the figure, transmitted bits are successfully estimated at receiver side.

CONCLUSION

In this paper, we propose a new receiver to demodulate I-PPM signals. The proposed architecture, which is referred to as Slot Period Detector (SPD), has lower complexity structure than that of the traditional scheme. However, the traditional scheme gives further BER performance compared with proposed structure. It can be shown the difference between the traditional and proposed architectures from the Fig. 2 and the Fig. 4. The proposed scheme is applied on real-time FPGA board. From experimental and simulation results, we prove that the proposed architecture is suitable for visible light communication systems.

References

1. IEEE Standard 802.15.7–2011, pp. 1–309, Jun. 2011.
2. Sugiyama H, Haruyama S, Nakagawa M. Experimental investigation of modulation method for visible–light communications. IEICE Trans.Communications, vol. E89–B (2006) 3393–3400.
3. Ma X, Lee K, Lee, K. Appropriate modulation scheme for visible light communication systems considering illumination. Electron. Lett., 48 (2012) 1137-1139.
4. Jeong JD, Lim SK, Jang IS, Kim MS, Kang TG, Chong JW. Novel Architecture for Efficient Implementation of Dimmable VPPM in VLC Lightings. ETRI Journal, 36 (2014) 905–912.
5. Noh J, Lee S, Kim J, Ju M, Park Y. A dimming controllable VPPM–based VLC system and its implementation. Optics Communications 343 (2015) 34–37
6. Lee S, Ahn BG, Ju M, Park Y. A modified VPPM algorithm of VLC systems suitable for fast dimming environment. Optics Communications 365 (2016) 43–48.

Hittite Journal of Science and Engineering, 2018, 5 (1) 31-35
ISSN NUMBER: 2148-4171
DOI: 10.17350/HJSE19030000075

Rotor Slot Distance Effects on Output Parameters in Single Phase Induction Motors

Merve Şen Kurt[1] and **Ahmet Fenercioğlu**[2]
[1]Amasya University, Department of Electric and Electronic Engineering,Amasya, TURKEY.
[2]Gaziosmanpaşa University, Department of Mechatronic Engineering,, Tokat, TURKEY

Article History:
Received: 2017/06/23
Accepted: 2017/09/30
Online: 2018/03/28

***Correspondence to**: Merve Sen Kurt,*
Amasya University, Department of Electric and Electronics Engineerin, Amasya, TURKEY.
Tel: +90 (358) 260-0066 (1468)
E-Mail: mervesenkurt@gmail.comcoils,

ABSTRACT

In this paper, single phase induction motor which has different rotor slot distances are analyzed with 2-D Finite Element Method (FEM). The analyses are carried out using ANSYS/Maxwell program which solves equations with FEM. The model has same stator and rotor slot geometry. The variable parameter is slot distance which is between outer diameter of rotor core and top border of slot. The single phase induction motor model has 2 poles, 96 W shaft power and run capacitor. It is connected to 220 V, 50 Hz AC network under the full load. Slot distance is varied from 0.2 to 1 mm in 0.1 mm steps. Magnetic model is solved for each distance. Electrical performance characteristics which are speed, efficiency, current, torque and power factor (PF) are determined. Magnetical flux density (B), flux lines and current density on bars are demostrated visually. Motor performance is improved as the slot distance decrease.

Keywords:
Efficiency, Design and optimization, Single phase induction motor, Finite element method, Rotor slot distance

INTRODUCTION

Single phase induction motors (SPIMs) nowadays are widely used in domestic and commercial areas because of cheap cost, simple structure, low noise and small dimensions etc. Split phase, start and run-capacitor single phase induction motors are well known SPIM motor types [1]. Although a lot of advantages have mentioned, a SPIM has some disadvantages. Its efficiency is low and starting performance is not so good to compare the other electrical machines types.

The optimal design of an induction motor in terms of electromagnetic torque means starting and breakdown torques are higher value [2]. Many researchers have investigated to improve the starting torque and efficiency of a SPIM. Some of them have focused the influence of rotor slot geometry like rotor slot type, shape, skewing, number of rotor slot, slot opening and core material.

Zhou Rui et al [3], have modeled two single phase induction motors with Maxwell 2D software and changed their dimensions in Maxwell 2D to find optimal slot geometry with respect to starting performance and efficiency. In similar studies; S. Sobhani et al [4] have examined dimensions of two SPIMs and mechanical shaft torque, rated slip, efficiency and power factor are compared. Literature [5,6] have investigated air gap flux densities for pear-shaped, circular and trapezoidal slots. They have simulated and analyzed with FEM. The literature [7] presents the advantage of double cage rotor over the single cage rotor induction motor. The literature [8] investigated the effect of rotor slots opening on torque and efficiency on SPIM. It was concluded that torque is destroyed around the slot opening because of the the rotating magnetic field. Optimal stator slot opening and closing have minimal effect of negative torque [8]. In the literature, effects of rotor slot shapes which are pear, trapezoidal and rounded shaped on harmonics of airgap flux densities were investigated and reported 1st, 3th, 5th, 27th and 29th harmonics [9]. Literature show that rotor slot geometry has an incredible effect in the motor performance. In this paper, rotor slot distance influences on SPIM with run capacitors have been examined. Speed, currents, shaft torque, power factor, efficiency have predicted and compared by 2D FEM for each slot distance.

MATHEMATICAL APPROXIMATIONS

The motor performance is affected by the parameters of rotor resistance and rotor leakage reactance in a squirrel cage induction motor. Rotor slot leakage flux depends on rotor slot geometry, saturation of magnetic material, rotor frequency and current density in the rotor.

Rotor bar inductance is derived from magnetic co-energy is calculated by using Eq. 1 [10].

$$W_m = \frac{1}{2}\iiint \overrightarrow{B}.\overrightarrow{H}.dV = \frac{1}{2}i^2 L \qquad (1)$$

Ampere's law is applied by using Eq. 2. Where *l* is the length of bar, *B* is the magnetic flux density (T), *I* is bar current and m_0 is permeability of vacuum [10].

$$\oint \vec{B}.\vec{dl} = \mu_0 I \qquad (2)$$

Bar inductance is calculated from Eq. 3

$$L_b = \frac{1}{2i^2}\mu_o.l\int_0^{h_{s2}+r} H^2(h).b(h).dh \qquad (3)$$

Where, h_{s2} is rotor bar depth, *dh* is variable of bar depth, *r* is total radius of bar circles (r_1+r_2). The inductance of rotor bar is depend on magnetic permeability coefficient (λ) by using Eq. 4 [10].

Table 1. The rotor slot dimensions of the SPIM

Symbol	Quantity	Size
hs2	The depth of rotor slot	4 mm
bs1	The upper width of rotor slot	3.67 mm
bs2	The lower width of rotor slot	2.96 mm
bso	The edge width of rotor slot	1 mm
hso	The distance of rotor slot from rotor core	0.2 – 1 mm
A	Slot area	21.856 mm²
r1	Radius of slot top circle	1.835 mm
r2	Radius of slot bottom circle	1.48 mm

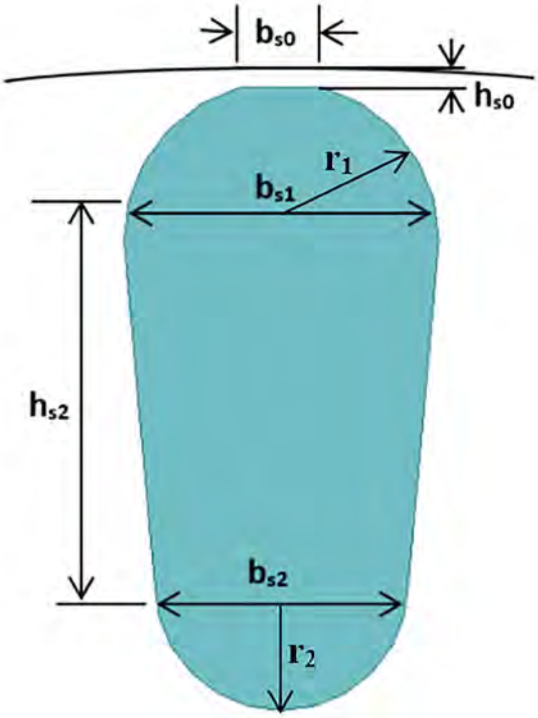

Figure 1. The geometry of drip-shaped rotor slot.

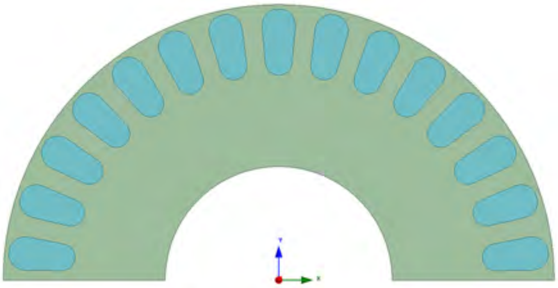

Figure 2. The cross section of rotor half model

$$L_b = \mu_o.l.N^2.\lambda \qquad (4)$$

Magnetic permeability coefficient (λ) differs according to rotor slot types. The literature [11-13] have presented detailed calculations for different rotor slot types. In this study, designed model has drip-shaped rotor slot. Fig. 1 shows the geometry of drip-shaped rotor slot, Table 1 shows the dimensions of the SPIM.

The coefficient λ is calculated by using Eq. 5 [10]. Where k_2 parameter is defined a value 0.645 to 0.785, the inductance attenuation factor, k_1 is a value less than 1.

$$\lambda = \frac{hs2}{3.bs1}k_1 + k_2 - \frac{hs0}{2.bs1} + \frac{hs0}{bs0} \qquad (5)$$

METHODS OF ANALYSIS

2D analyses of motor and external circuits for excitations were carried out using ANSYS/Maxwell FEA software and symmetrical half model was analyzed in transient and steady state conditions under full load which is 0.31 Nm load torque. Analysis sampling frequency is 18 Khz, analysis period is 1 second and starting speed is 0, rated speed is about 2950 rpm.

Model of the SPIM

Model SPIM has squirrel-cage rotor, 96 W shaft power, 2950 rpm speed, 0.31 Nm load torque. It is connected 220 V, 50 Hz AC network. Fig. 2 shows the rotor cross section. Main and auxiliary windings are placed in 24 slots of the stator magnetic core. Rotor and stator cores made of laminated steel material with 0.95 stacking factor to reduce eddy current losses on its periphery.

As shown in Fig.2 the rotor has 30 slots which are drip-shaped and parallel tooth. The squirrel cage rotor consists of cast aluminium bars with bulk conductivity is 23x10^6 S and relative magnetic permeability is 1.000021.

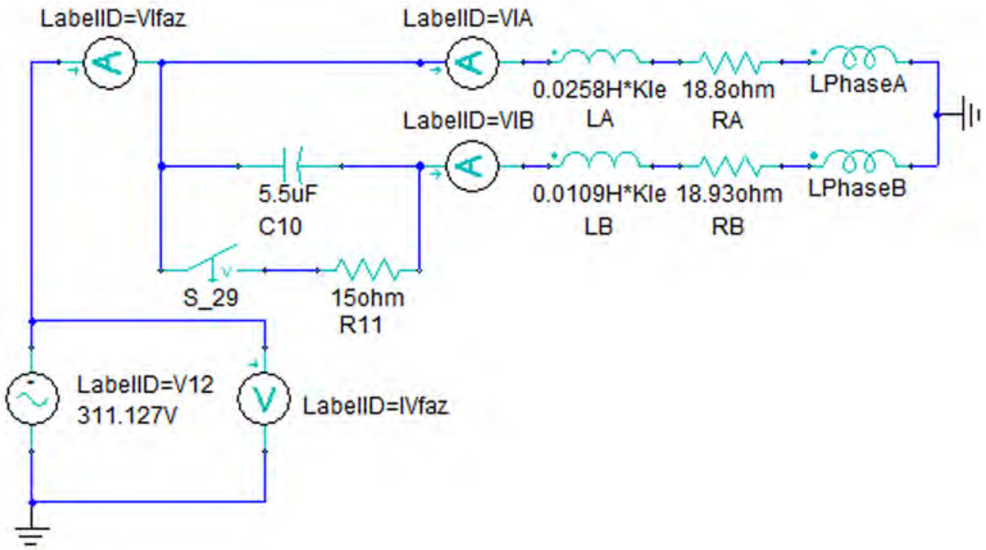

Figure 3. External circuit of the SPIM

External Electric Circuit

The major problem which is a single-phase network does not produce a rotating magnetic field. Instead, the magnetic field produced by a single-phase source remains stationary in position and pulses with time. Since there is no net rotating magnetic field, conventional induction motors cannot function, and special designs are necessary [14]. So, the single phase motor needs an auxiliary winding which produces phase angle and rotating magnetic field. The external circuit of the model is given in Fig. 3.

Each horizontal branch represents main and auxiliary windings. R_A, L_A, L_{phaseA}, R_B, L_B and L_{phaseB} are respectively main winding resistance, end winding inductance, phase inductance, auxiliary windings resistance, end winding inductance and phase inductance. Phase inductances depend on magnetic flux. Run capacitor is serial connected to auxiliary winding, starting resistor is parallel connected to run capacitor. Starting resistor is switched off after starting.

FINITE ELEMENT ANALYSIS (FEA)

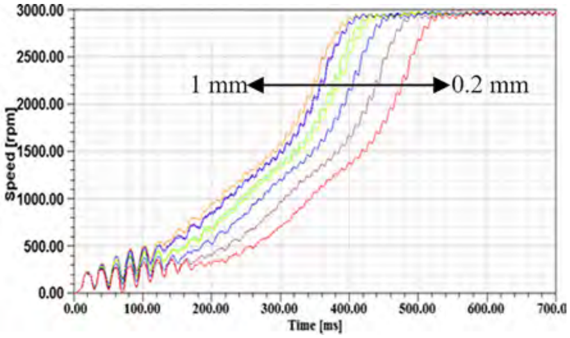

Figure 4. Acceleration and transient time

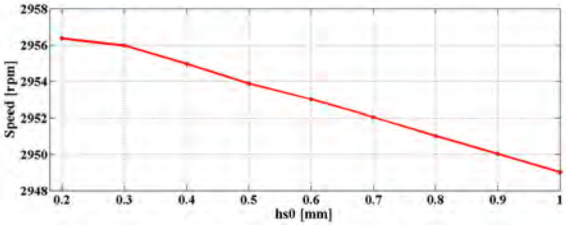

Figure 5. Rated speed versus to rotor slot distance

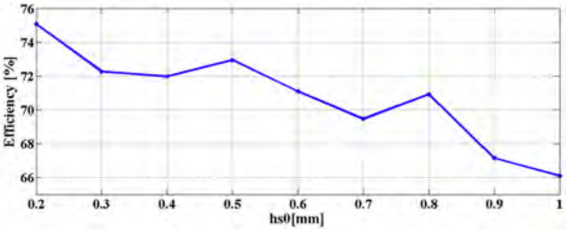

Figure 6. Efficiency versus to rotor slot distance

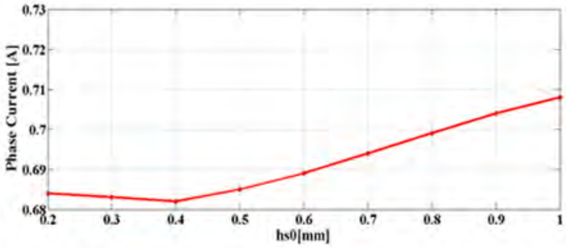

Figure 7. Phase current versus to rotor slot distance

2D transient analyses of motor were carried out by using FEA method. The calculations were obtained from different rotor slot distances (*hs0*) from 0.2 to 1 mm in 0.1 mm steps. Fig. 4 shows the change in speeds for transient and steady states. The smaller slot distance is the longer starting time. Fig. 5 shows changing in average value of speed according to the rotor slot distance for steady-state condition. As it can be seen in Fig. 4, the motor reaches

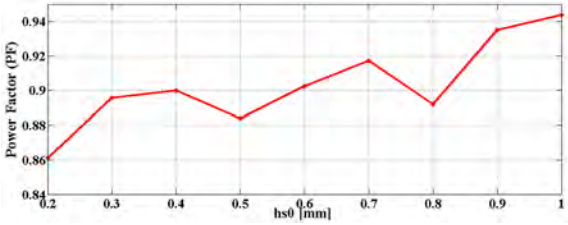

Figure 8. Power factor versus to rotor slot distance from the core

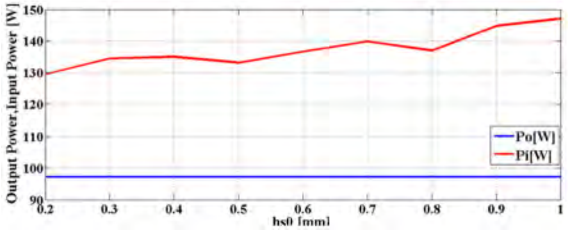

Figure 9. Output power according to rotor slot distance

steady state after 600 ms and average speed values are very close for all of the rotor slot distances. As the distance increases 0.2 to 1 mm in 0.1 mm steps, motor speed decreases because of changes the inductance of rotor bar (Eq. 4 and Eq.5).

Fig. 6 shows that the rotor slot distance increases from 0.2 to 1 in 0.1 mm steps. When it was reach to 1 mm, the efficiency was decreased by 11,96%.

The phase current which is the sum of the main and auxiliary windings currents is shown in Fig. 7. The maximum value of phase current is calculated as 0.71 A in 1 mm slot distance.

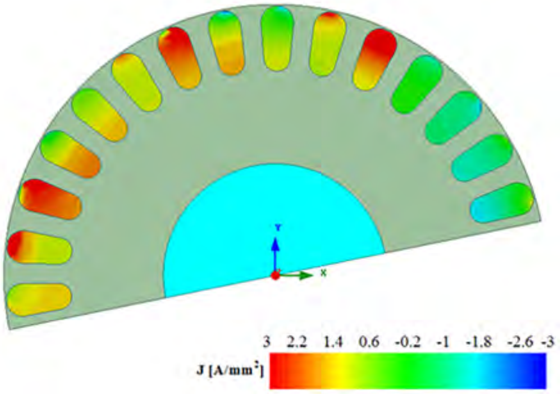

Figure 10. Current density distribution on rotor slots

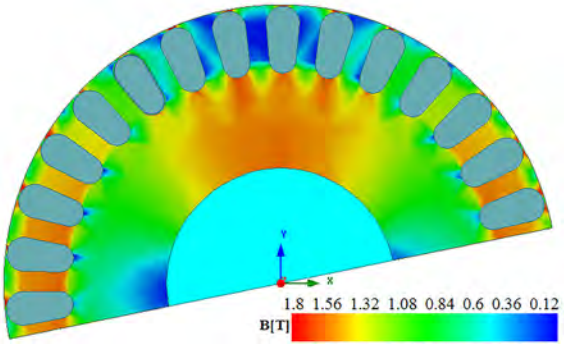

Figure 11. The distribution of the magnetic field density on stator and rotor cores

Table 2. Limit values of flux density [16,17]

Position B_g	Flux Density[16]	Maximum Flux Density[17]
Airgap,	*0,65-0,82 T*	
Stator yoke	*1,1-1,45 T*	*1,7 T*
Stator teeth	*1,4-1,7 T*	*2,1 T*
Rotor yoke	*1,2 T*	*1,7 T*
Rotor teeth	*1,5-1,8 T*	*2,2 T*

The power factor varies according to rotor slot distance is shown in Fig. 8 It is depended on magnetic flux in air gap. Magnetic flux density varies according to flux path length. The longer slot distance is increase flux path and leakage reactance. For this reason power factor is rised. The output torque is constant for each slot distance. It is shown in Fig. 9.

Bar current density and core magnetic flux density have to take into consideration besides electrical performance variables when an optimal slot geometry is chosen. Current density (J) on the rotor bars have to be in range 2,2 < J < 4,5 A/mm2 for small motors with aleminum rotor bars [15]. Bar current density distributions on rotor slots have been shown in Fig. 10.

Magnetic flux densities in air gap, stator yoke, stator teeth, rotor yoke and rotor teeth have to be in range of Table 2 which shows the permitted limit values in the literature. Fig. 11 shows the distribution of the magnetic field density on stator and rotor cores.

As can be seen in Fig. 11 maximum values of flux density is 1.118 T in rotor yoke, 1.577 T in rotor teeth, 1.224 T in stator yoke and 1.186 T in stator teeth, respectively. It can be concluded that rotor yoke and rotor teeth, stator yoke and stator teeth don't exceed permitted limit values in Table 2.

Table 3. Rotor slot distances effects on performance

Parameters	*Slot distance (0.2 mm)*	*Slot distance (1 mm)*
Transient time	*420 ms*	*540 ms*
Rated speed	*2956 rpm*	*2949 rpm*
Phase current	*0.684 A*	*0.708 A*
Electromagnetic Torque	*0.337*	*0.339*
Load torque	*0.314*	*0.315*
Power Factor	*0.86*	*0.94*
Input Power	*129.510*	*147.076*
Output power	*97.223*	*97.209*
Efficiency	*75.070*	*66.094*

CONCLUSION

This study investigates the impact of rotor slot distance on the electrical performance of single phase induction motor. Rotor slot distance is between rotor core outer diameter and top border of rotor slot. The distance is increased from 0.2 mm to 1 mm in 0.1 mm steps. Motor performance is determined for each distance. The longer slot distance, the motor starting time is shorter, the rated speed and the efficiency are lower. As the slot distance is increased, the phase current, the electromagnetic torque and the power factor are increased. Performance values are given in Table 3 for 0.2 mm and 1 mm slot distances. The λ coefficient in Eq. 4 and Eq. 5 depends on slot distance (h_{so}) If the rotor slot distance is smaller, motor electrical performance is improved. 0.2 mm slot distance is the optimal solution in this study.

ACKNOWLEDGEMENT

This paper is presented in ICAT'17 at Istanbul Conference, and published in proceeding book as abstract. It is supported by 2016/81 numbered Gaziosmanpasa University BAP Project.

References

1. Mademlis C, Kioskeridis I , Theodoulidis T. Optimization of single–phase induction motors–part I: maximum energy efficiency control. IEEE Transactions on Energy Conversion 20(1), (2005) 187–195.
2. Fireteanu V, Tudorache T, Turcanu OA. Optimal design of rotor slot geometry of squirrel–cage type induction motors, 2007 In. Conf. on Electric Machines & Drives, Antalya, Turkey, 2007, pp. 537–542.
3. Rui Z, Qunjing W, Guoli L, Guanghui F. Optimal design of single–phase induction motor based on maxwell 2D rmxprt. 15th Int. Conf. on Electrical Machines and Systems, Incheon, South Koreo, 2010.
4. Sobhani S, Yaghobi H, Samakoosh M. Optimize efficiency and torque in the single–phase induction motor by adjusting the design parameters. 12th Int. Conf. on Environment and Electrical Engineering, Wroclaw, Poland, 2013.
5. Zhang K, Jiang X, Wu Y, Zhang L, Wu X. Effect of slot shape in rotor of electrical motor with high–speed spindle on slot ripples. 2nd Int. Conf. on Modelling, Identification and Control (ICMIC), Okayama, Japan, 2010, pp. 670–675.
6. Turcanu OA, Tudorache T, Fireteanu V. Influence of squirrel–cage bar cross–section geometry on induction motor performances. 23rd Int. Conf. on Power Electronics, Electrical Drives, Automation and Motion (SPEEDAM), Taormina, İtaly, 2006, pp. 9–15.
7. Yahaya Enesi, Omokhafe T, Agbachi EO, James AG. Advantage of double cage rotor over single cage rotor induction motor, Innovative Systems Design and Engineering, 6 (12), (2015) 1–4.
8. Jang GH, Park SJ, Characterization of a single–phase induction motor due to the effect of slot opening, IEEE Transactions on Magnetics, 40 (4), (2004) 2065–2067.
9. Negoita A, Scutaru G, Peter I. Influence of rotor static eccentricity on the noise level of a single phase squirrel cage induction motor, 13th International Conference on Optimization of Electrical and Electronic Equipment (OPTIM), Brasov, Romania, 2012, pp. 373–378.
10. Şal S, İmeryüz M, Ergene L. Kafesli asenkron motorlarda maliyet kısıtı altında rotor çubuklarının analizi, EMO Bilimsel Dergi, 2(3), (2012) 23–28.
11. Boldea I, Nasar SA. The Induction Machine Handbook, second ed. CRC Press, New York, 2002.
12. Pyrhönen J, Jokinen T. Design of Rotating Electric Machines, second ed. Wiley Press, New Delhi, 2008.
13. Gürdal O. Elektrik Makinalarının Tasarımı, first ed. Nobel Press, İstanbul, 2006.
14. Chapman SJ. Elektrik Machinery Fundamentals, fourth ed. McGraw–Hill, New York, 2005.
15. Fu F, Tang X. Induction Machine Design Handbook, China Machine Press, Beijing, 2001.
16. Say MG. Performance and Design of AC Machines, third ed. Pitman Publishing, London, 1970.
17. Lipo TA. Introduction to AC machine Design, third ed. Wiley–IEEE Press, Madison, 2004.

Hittite Journal of Science and Engineering, 2018, 5 (1) 37-48
ISSN NUMBER: 2148-4171
DOI: 10.17350/HJSE19030000076

Rehabilitation of Francis Turbines of Power Plants with Computational Methods

Kutay Celebioglu[1] **Selin Aradag**[1,2] **Ece Ayli**[1,3] **and Burak Altintas**[1,2]
[1] TOBB University of Economics and Technology, Hydro Energy Research Laboratory, Ankara, TURKEY
[2] TOBB University of Economics and Technology, Department of Mechanical Engineering, Ankara, TURKEY
[3] Cankaya University, Department of Mechanical Engineering, Ankara, TURKEY

Article History:
Received: 2017/05/08
Accepted: 2017/11/14
Online: 2018/03/28

***Correspondence to**: Kutay Celebioglu, TOBB University of Economics and Technology, Hydro Energy Research Laboratory (ETU Hydro), Ankara, TURKEY*
Tel: +90 (312) 292-4473
E-Mail: tkcelebioglu@etu.edu.tr

ABSTRACT

Rehabilitation of existing hydroelectric power plants (HEPP) by redesigning the hydraulic turbines is usually more elaborate than designing a tailor-made turbine for a new plant. Some of the parts are buried and the space is limited with the size of the old turbine; therefore, this increases the number of constraints imposed on the design. This article presents a Computational Fluid Dynamics (CFD) based rehabilitation procedure involving the state of the art redesign of the turbine of a hydroelectric power plant for better performance at design and off-design conditions of several head and flow rates. Runner and guide vanes of the Francis turbine are designed per the design head and flow rates available for the turbine at the site. The simulations for the designed parts are performed both separately and using all turbine parts as full turbine analyses. Both the design and off-design conditions are simulated for the newly designed and existing turbines for comparison purposes. Cavitation performance of the new design is also determined. The proposed methodology is applicable to any Francis type turbine and any HEPP that needs rehabilitation.

Keywords:
Francis turbine; Rehabilitation; Efficiency; Runner; Guide vane

INTRODUCTION

Rehabilitation of hydraulic turbines of existing power plants is an important topic because of the low performance, poor reliability, frequent maintenance intervals and undesirable cavitation properties of old turbines at the plants. Rehabilitation projects increased worldwide to improve turbine designs and to reach the desired performance characteristics, especially with the improvements in computational power and Computational Fluid Dynamics (CFD) technology. However, rehabilitation of old power plants is often more difficult than the design of the turbines for new power plants since most of the existing parts cannot be altered because some of the parts are buried and the space is limited with the size of the old turbine.

Both experimental and numerical methods are common in the design [1] and rehabilitation of Francis turbines. Performing numerical simulations is an efficient approach as an alternative to model tests. Steady state and transient Francis turbine simulation results are presented in the study of Beatove et al. [2]. Interactions between turbine components (such as rotor and stator) are investigated and fluctuating pressure dynamics are obtained with transient simulations. Experimental measurements are also performed using dynamic pressure sensors and strain gages. Numerical results agree well with the experiments. Qian et al. [3] worked on three-dimensional, unsteady, multiphase flow simulations for the whole Francis turbine. Numerical analysis is performed with a commercial CFD software and sliding mesh model is used to obtain time dependent results. Pressure pulsations are analyzed via Fast Fourier Transform (FFT). Their experimental and numerical results agree well. Su et al. [4] computed the three-dimensional turbulent flow in Francis turbines using Large Eddy Simulations (LES). They used unstructured meshes for the spiral case and the runner, while structured meshes were utilized for the remaining components. They found out that cavitation was observed at the suction side of the blade under partial load conditions. Patel et al. [5] also performed three-dimensional, unsteady CFD simulations for Francis turbines. They investigated the effect of partial loading on turbine performance. The efficiency first increases up to full operating load and then it starts to decrease. Head loss variations are investigated in detail by using velocity plots. Turbine performance is predicted both at the best efficiency point and at partial load conditions which shows improvement over the existing design. Kaniecki et al. [6] re-engineered the runner and guide vanes of the Grodek and Kamienna hydroelectric power plants. The efficiency of Kamienna HEPP increased from 75% to 85%. Akin et al. [7] developed a design methodology for Francis turbines. Overall turbine efficiency can reach up to 92.3% with their design methodology. Gohil and Sanini [8] considered a Francis turbine with a capacity of 225 kW power in their simulations. CFD results agree with model tests. Shukla et al. [9] aimed to validate their three dimensional CFD results with experimental findings, as well.

There are several rehabilitation studies worldwide; however, the results are usually neither generalized nor published in archival publications. Bornard et al [10] report the results of several rehabilitation projects. Xi-de and Yuan [11]. In some of these projects, the guide vanes and the runner are the only modified parts as in this study. However, in some of them, rehabilitation of other components were also found feasible and performed. In two of the projects reported by Bornard et al. [10] stay vanes are modified and efficiency gains of less than 1% are obtained. However, when the guide vanes and runners are altered, the efficiency gains are more than 3% as in Chute des Passes, Shasta and Yinxiuwan projects explained in detail by Bornard et al. [10], Michel and Kunz [12] and Xi-de & Yuan [11]. Cavitation characteristics can also be improved when the runner is modified as in Kelsey project, reported by Bornard et al. [10].

Kepez 1 hydroelectrical power plant, located in Antalya, Turkey, was constructed in 1960's. It has three identical Francis type turbines. Redesign of the turbine is performed based on CFD. The design criteria are higher efficiency, power output, no cavitation and wider operating range. The plant has been utilized for several years and accumulation of lime on pipe surfaces is unavoidable because of the water characteristics in the area. How lime accumulation affects the friction factor is an important concern because the losses in the pipe can alter the head and flow rate specifications of the turbine to be designed, drastically. Therefore, the friction factor of the pipes and equipment of the plant is determined through experimental measurements at the site and analysis of the whole pipe and power system as a network. The new turbine is designed per the design head and flow rates determined based on this experimentally obtained friction factor. Off-design performance of the runner is also tested using several possible operating points.

The scope of this work includes redesign of the guide vanes and runner using available data for other turbine parts and on-site measurement of the geometries. The simulations for the designed parts are performed both separately and using all turbine parts as full turbine analyses. Both the design and off-design conditions are simulated for the designed and existing turbines for comparison purposes. Cavitation performance of the new design is also determined. The proposed methodology is applicable to any Francis type turbine and any HEPP that needs rehabilitation.

METHODOLOGY

The first step in the turbine rehabilitation process is to decide on the head and flow rate values of the power plant. The friction factor was found to be 0.014 for the pipes based on experimental measurements of pressure values and system analysis using Watercad, which is a commercial software to perform network analysis of pipe systems [13]. The friction factor is utilized to obtain head losses, then to determine the available head for the turbine. The whole CFD study is based on this head value. The expected performance values of the plant, based on the hydraulic analysis of the system are summarized in

Table 1 General performance values for the HEPP.

Head (m)	*162*
Power (MW)	*8.8 MW/turbine*
Rotational Speed (rpm)	*750*
Flowrate (m³/s)	*6.1*
Turbine efficiency	*92%*

The existing turbines cannot produce the expected power. Vibration and noise occur at partial load conditions, as well. Erosion and damage are also observed at the trailing edge of the guide vane and at the suction side of the runner as shown in Fig. 1, most probably due to cavitation.

Original guide vanes and runner are redesigned. Other parts are buried to concrete, they cannot be changed; however, they play an important role in full turbine CFD simulations. The design procedure starts with the CFD part for rehabilitation since the geometry is restricted with the

Figure 1. Picture of the existing guide vane and the runner

parts that are buried. Critical parameters for the guide vane and runner, blade angle distribution, blade thickness, inlet and outlet diameter are optimized to reach higher efficiencies with no cavitation. Fig. 2 shows the flow chart of the entire design process. First step is the preparation of the geometry for simulations. CAD models of the replaceable turbine parts are obtained through laser scanning of the actual parts at the site. Measured geometries are compared with the available technical drawings. The technical drawings of the buried parts, which are the spiral case, stay vane and draft tube of the turbine, are used in the CFD analysis. CAD model of the existing turbine is shown in Fig.3.

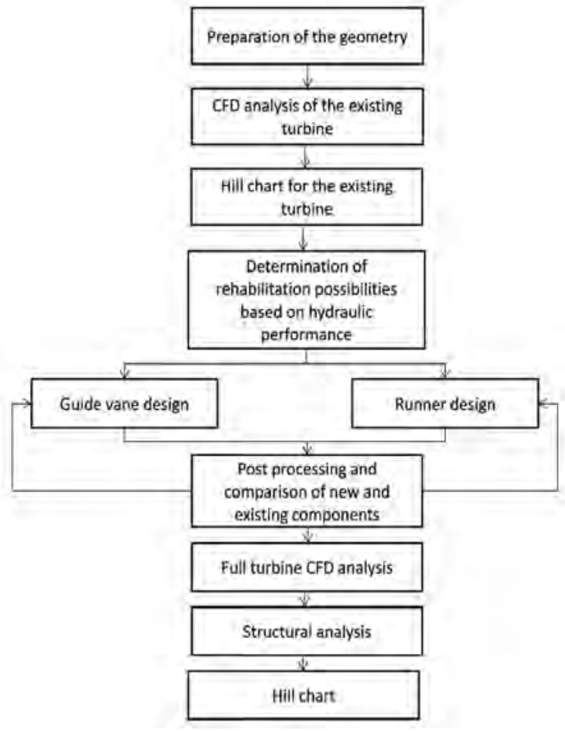

Figure 2. Design flow chart

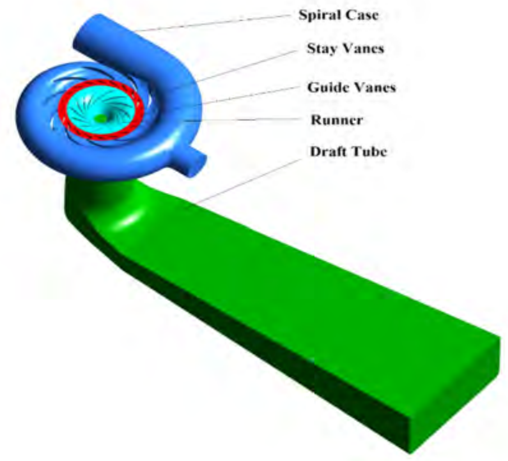

Figure 3. CAD model of the existing turbine

After conducting separate CFD analysis of the components, full turbine analyses for nominal and partial loads are performed to obtain a hill chart that shows the performance of the turbine. The analyses at off-design points help to examine the performance of the turbine at partial load conditions, as well. The problems of the existing turbine are examined through turbine efficiency curves, flow angles and pressure distributions. The guide vanes and runner are redesigned to ensure better cavitation characteristics and hydraulic performance for both nominal and partial loads. The hill chart for the newly designed turbine is also constituted.

ANSYS CFX [14] software is utilized. Finite Volume Method that solves the incompressible pressure-based Reynolds Averaged Navier-Stokes (RANS) equations is employed. k- ε turbulence model is used. High order upwind and second order centered schemes are used for the convection and diffusion terms, respectively.

Cavitation simulations are implemented with homogeneous multiphase model which allows modeling the mixture as a pseudo-fluid. Thus, the governing equations consist of mass conservation, a set of momentum equations and a transport equation for the volume fraction. Shear Stress Transport (SST) is used as turbulence model to solve Reynolds Averaged Navier-Stokes (RANS) equations, which combines k-ω and k-ε turbulence models. It resolves flow separations accurately near the walls. Rayleigh Plesset model is implemented for the detection of cavitation. Steady-state cavitation simulations are performed using the solution of the corresponding steady-state simulations without cavitation as an initial condition. The convergence level is set to $1x10^{-5}$.

Multi frame reference model (MFR) is used to model the interaction of the parts with each other [15]. Runner is attached to the guide vane and draft tube by frozen rotor interface. There are several recent studies in literature in which the interactions between runner-guide vane and runner-draft tube are included via frozen rotor interface. For example, Lenarcic et al. [16] simulated incompressible turbulent flow for a high head Francis turbine under steady operating conditions which is computed using an open source code. Influences of the coupling methods are compared with each other and with experimental data. Frozen rotor coupling method results are compatible with the experimental results. Tonello et al [17] worked on steady-state operation of Francis-99, Tokke turbine at different loads. Simulations are carried out using both the frozen rotor approximation and unsteady sliding mesh technique. It is found out that sliding mesh approach does not offer significant advantage when compared to the frozen rotor model based on comparisons with each other and experimental

Table 2. Mesh properties for runner.

Mesh quality	Number of nodes	Number of elements	Min y+	Number of elements in the boundary layer
Low	240771	221100	100	10
Medium	417911	388320	50	10
High	708700	664950	25	10
Very high	917472	865050	10	10

data. Laouari and Ghenaiet [18] used frozen rotor interface to simulate the turbulent flow through a small horizontal Francis turbine. Hydraulic performance is presented for different rotational speeds. Predicted performance shows that at the nominal point, maximum hydraulic efficiency reaches 79.28% and there is an important drop with increased discharge.

Pressure inlet, mass flow outlet boundary conditions are used for the design of the runner and guide vanes. For full turbine analyses, which comprise the simulations of all turbine components, mass flow inlet and pressure outlet are utilized as boundary conditions. All other parts are considered as no slip wall condition with a smooth wall assumption. In the design phase, it is found sufficient to model only one guide vane and runner and to use circumferential averaging, therefore periodic interfaces. However, for full turbine analyses, whole system containing the guide vanes, stay vanes and runner blades are used to observe the general performance of the system.

Computational domain for the design of the runner is only the runner itself. Therefore, CFD analyses are performed using HP Z840 workstations, which have Intel(R) Xeon(R) CPU E5-2640 v3 2.60GHz 16 (32 cores) and 64.0 GB installed RAM. One solution takes approximately 30 minutes using this computer. When the runner design is finished, full turbine analyses, the computational domain of which is composed of the spiral case, stay vanes, guide vanes, runner and draft tube, are performed by using a supercomputer clustered from 11 nodes HP Proliant DL380p Gen8, which have Intel(R) Xeon(R) E5-2695v2 2.40 GHz Turbo 3.2GHz (12 Cores) and 64.0 GB installed memory (RAM) in each node. A solution for head and flow rate combination takes 7-8 hours using this supercomputer facility with 120 processors.

Mesh independency study is performed separately for all components. As runner is the major component of the turbine, it is crucial to check the mesh independency of the solution to have accurate runner parameters such as runner hydraulic efficiency and power. Mesh properties for the runner are given in Table 2, as a representation of the mesh independency study performed.

The result of mesh independency study for runner in terms of output parameters is given in Table 3. High quality meshes are used for further runner computations based on the results of the grid refinement study.

Summary of mesh independency study is given in Table 4. For single turbine analysis that comprises five components, 36x106 mesh elements are used. Separate meshes are used for rotating and stationary components due to the complexity of the geometries. Using same number of elements, cell size and distribution for all simulations is very difficult; therefore, Generalized Grid Interface (GGI) method is used to transfer all flow gradients through nonconformal meshes [19].

Table 4. Summary of the mesh independency study.

Component	Number of Elements
Spiral Case & Stay Vane	20,193,590
Guide Vane	222,690 x 20 = 4,453,800
Runner	664,950 x 13 = 8,644,350
Draft Tube	3,068,834
Total number of element	36,360,574

RESULTS AND DISCUSSION

Analysis of the existing turbine

Different opening percentages and different volumetric flow rates for each opening of guide vanes are necessary to develop a numerical hill chart for constant rotational speed. Analyses are performed for a range of head values (from 142 m to 173 m). For all head values, CFD analyses are performed for an operating range of %20 to %130 loading which is accomplished by adjusting the guide vane angles.

Table 3. Mesh independency study result for runner.

Control parameters	Low Quality Mesh	Medium Quality Mesh	Relative Error (%)	High Quality Mesh	Relative Error (%)	Very High Quality Mesh	Relative Error (%)
ΔH	0.909	0.905	0.442	0.905	0.033	0.905	0.011
Head (m)	157.987	156.412	1.007	155.170	0.800	155.620	0.289
Efficiency (%)	96.915	97.195	0.288	97.322	0.130	97.367	0.046

Head-discharge operating characteristics of the existing turbine are shown in Fig. 4. The graph shows the isoclines of the efficiency (η). 52 full turbine simulations for different guide vane openings and head values, with 36 million grid points each, are simulated to obtain hill chart that demonstrates the behavior of the turbine for a wide range of head and flow rates representing the off-design conditions of turbine operation. The area between the black lines, denote the turbine operating range. In an efficient design, design point should be in the middle of the hill chart and the operating range with maximum efficiency value. On the other hand, in the existing design, the design point cannot reach the maximum efficiency of the system, and the operating region is not settled at the high efficiency zone. When the turbine is used off limits, keeping the efficiency as high as possible is an important constraint. Therefore, in the new design, the operating range should be widened and must be inside the maximum efficiency region.

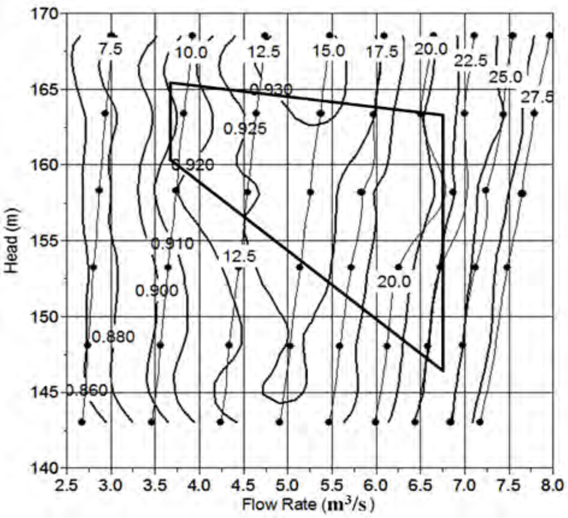

Figure 4. Hill chart for the existing turbine.

Hydraulic energy is converted to mechanical energy by decreasing the pressure significantly inside the runner. Pressure can be below the vapor pressure which induces cavitation at high loads. This is a very aggressive process which can cause material damage and performance drop in the overall turbine efficiency. To investigate cavitation in the turbine, pressures are examined. Cavitation occurs when the pressure is less than the vapor pressure (Pv) determined by site conditions as 4.24 kPa. In Fig. 5, pressure distribution on the existing runner blade at the design conditions is shown. It is seen that the pressures are below vapor pressure near the shroud, which causes cavitation.

To minimize this low-pressure zone, introducing a leaning from the shroud in the direction of rotation can be a solution [20]. Fig. 6 shows the meridoinal view of the turbine blades. Hub and shroud, as well as the leading and trailing edges of the runner are shown in the figure. The important angles that define the runner geometry are shown in Fig. 7. Here, $\beta 1$ (for inlet) and $\beta 2$ (for outlet) are known as “Beta angles of the runner blade” or “the metal angles of the blade” [20]. In the same figure V_{1u} and V_{2u} are the circumferential velocities. w_2 is the relative speed at the outlet of the runner.

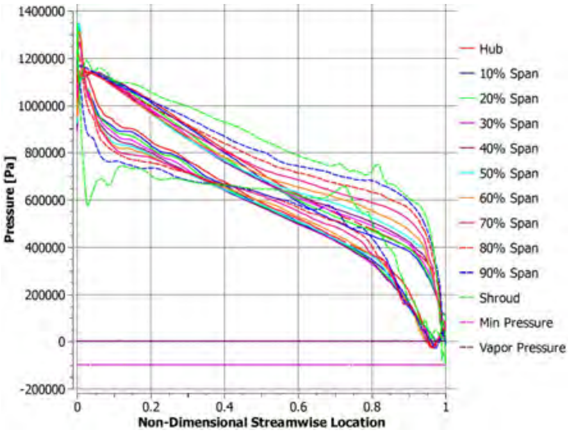

Figure 5. Pressure distribution on the existing runner blade at the design condition.

Velocity streamlines around the runner blades are shown in Fig 8. Vortices and seperation are observed at the pressure side of the runner blade. These cause performance

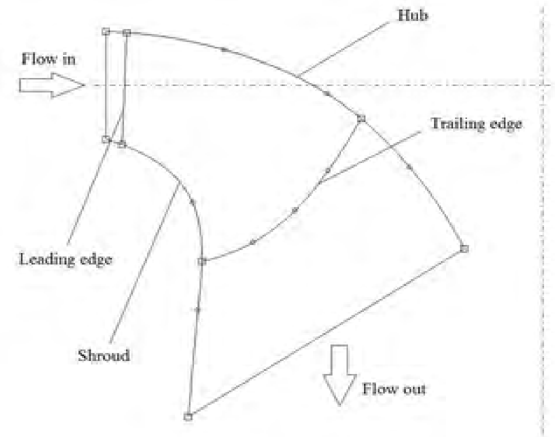

Figure 6. Meridional view of the runner.

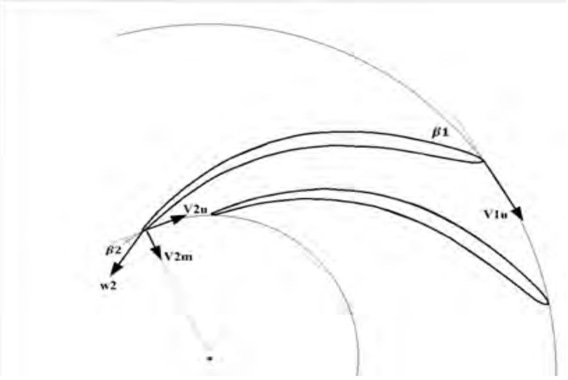

Figure 7. Axial view of the turbine runner blades.

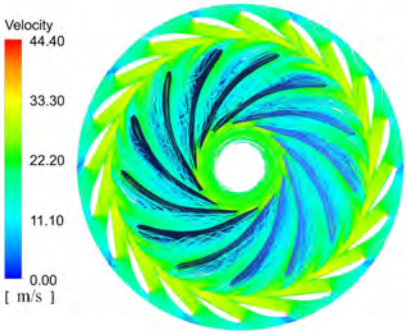

Figure 8. Velocity streamlines for full loading operation of the existing turbine (Head=162 m, 17.5^0 guide vane opening, 63.6% of full opening).

reduction in the runner. These formations are also one of the reasons of cavitation. Uniform flow distribution around the blade should be provided for the design conditions for rehabilitation of the turbine.

CFD based design of the new turbine

NACA 0016 profile is used for the final guide vane design (Fig. 9). Numerical weighted average efficiency increase is about 2.2 % for NACA0016 geometry at a net head of 157 m (Fig. 10). As seen in Fig. 10, when NACA 0018 profile is used for the guide vanes, the efficiency gain is not as high as the gain obtained with NACA 0016 profile. One important reason of this efficiency rise is the fact that the old guide vane is much rougher than the new one. The roughness is because of being in usage for several years and material erosion.

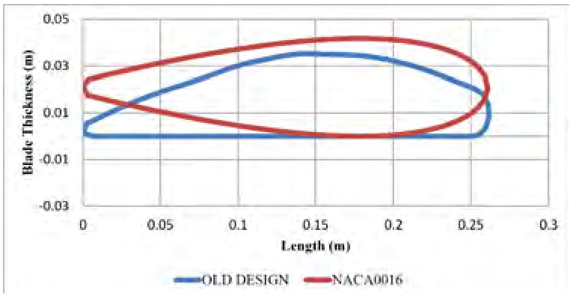

Figure 9. New and existing design geometries for the guide vanes.

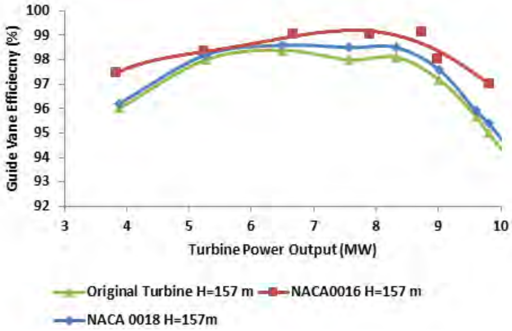

Figure 10. Guide vane efficiency versus turbine power output for the existing and new guide vanes.

The angle of guide vanes and their profile should be reasonably designed to achieve flow stability with no separation and vortices and maximum efficiency for design conditions. For some of the simulated guide vane opening angle alternatives, runner pressure distribution is shown in Fig. 11. For 20^0 and 17.5^0 guide vane openings, water hits to the suction side of the blade. Whereas, when the guide vane opening is changed to 15^0, the flow hits to the leading edge of the runner blade.

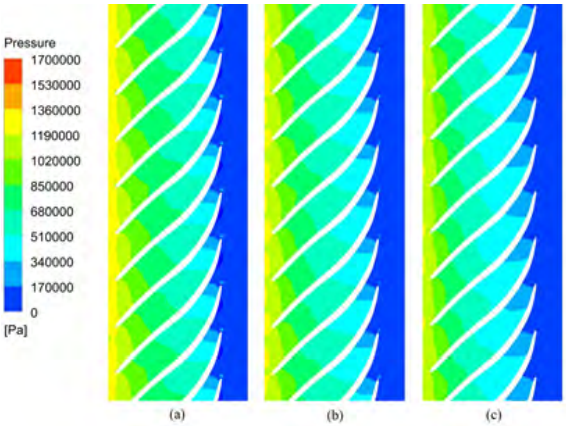

Figure 11. Runner pressure distribution for (a) 20^0 (b) 17.5^0 (c) 15^0 guide vane opening angles.

The angles of the runner blades, flow angles, blade length and thickness are important for runner design process. Several simulations are performed by changing these parameters. The required head, flow rate, power with maximum efficiency are obtained by making improvements in the design. In Table 5, all design cases are tabulated. Some of the designs are analyzed and compared with each other to observe the effect of each parameter on runner performance and cavitation characteristics.

The aim is to attain the required head and power values with high runner efficiency and better cavitation characteristics. The parameters that are optimized in the design are blade inlet and outlet edge slopes, beta and theta angle distribution for each layer of the blade and blade thickness profile. Blade profile lengths are increased near the hub layer by using beta angle distribution to improve the cavitation characteristics. In addition, guide vane angle is one of the most important parameters that control the uniform flow distribution through the leading edge to the trailing edge of the blade and it is modified, as well. It is kept around 16^0 for smooth velocity distribution and cavitation free performance.

Smooth beta distribution for the runner, which provides higher head and flow rate, is important. Leaning is provided from the leading edge of the runner from 1^0 to 5^0 to obtain balanced pressure distribution which is very important when using X-blade design. Leading edge beta value is adjusted to make sure that leading edge separation disappears, however leading edge cavitation becomes the limit in the process of increasing leading edge beta angles. Trailing edge beta angles are changed between 11^0 and 19^0. This improves cavitation characteristics but the power can decrease if the angle becomes higher.

Shorter blade lengths and thick edges for the leading and trailing edges can decrease friction losses which increases efficiency. However, shorter blade lengths can make the blades prone to cavitation. Therefore, the blade length is only decreased twice in 2 cm increments. Beta angles for the hub and shroud are important for power increase and they are increased from 3^0 to 7^0. Theta distribution must be as linear as possible for cavitation; therefore, this fact is also kept in mind during the design process.

In Fig. 12, meridional profiles, which demonstrate full pattern of water flow in the runner, for the existing and new runners are shown. Blade length is gradually shortened. This decreases the friction losses on the blade and increases the efficiency for higher flow rates. However, shorter blade promotes cavitation.

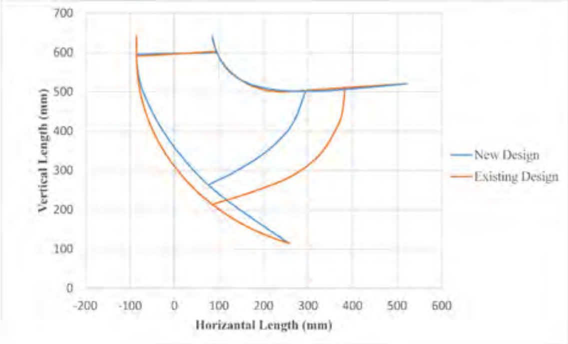

Figure 12. Meridional profile of the existing and new runners.

In Fig. 13, runner blade thickness change is shown. The original thickness distribution was changed to a NACA-profile (V18). The final runner blade is thicker than the existing runner which can also increase the mechanical strength of the runner. On the other hand, due to the contraction of the flow field, the possibility of exposure to cavitation increases. Leaning is defined from the hub to decease cavitation. Per previous studies of Ayli et al. [20, 21] and the results examined in this research, (V20 to V23), it is observed that increasing the lean in the direction of rotation improves the cavitation characteristics.

Conventional Francis turbine runners like the one under investigation in this research, are prone to cavitation damage on the suction side of the blade, especially to leading edge cavitation. Leading edge cavitation is one of the most hazardous types for Francis turbines. As it occurs at the inlet of the runner, damage is heavy; it causes vibration and provokes pressure fluctuations [22]. X-blade technology is improved by Billdall and Holt [23] to eliminate leading edge cavitation and to increase the performance of the runner during the development of the Three Gorges Project in China. A pressure balanced design must be performed when using X-blade shapes. If the design is not pressure balanced, the dynamic loads which are larger at part-load conditions, increase the risk of blade cracking [24]. Although the manufacturing of X-blades is more difficult and costly and pressure balanced blade design is crucial, X-blade technology has been popular in the 2000's because of its advantages.

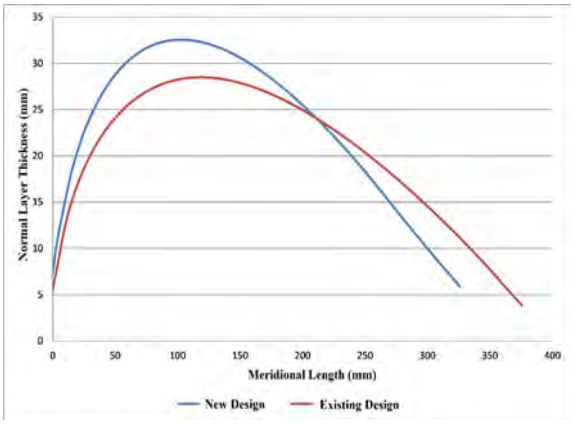

Figure 13. Runner thickness for the existing and new runner.

One series of runner blade versions comprise modifications that focus on improving the V_u distribution at the outlet of the blade [25]. The modifications are mainly focused on the trailing edge of the blade. In Fig.14, circumferential distribution of V_u for the existing and new runners is shown. Here, x-axis denotes the dimensionless spanwise location on the blade. 0 and 1 correspond to hub and shroud. Defining leaning from the hub inhibits the separations and low pressure zones in the flow which contribute to more energy release in the runner. As the result of this series of arrangements, circumferential velocity becomes more uniform.

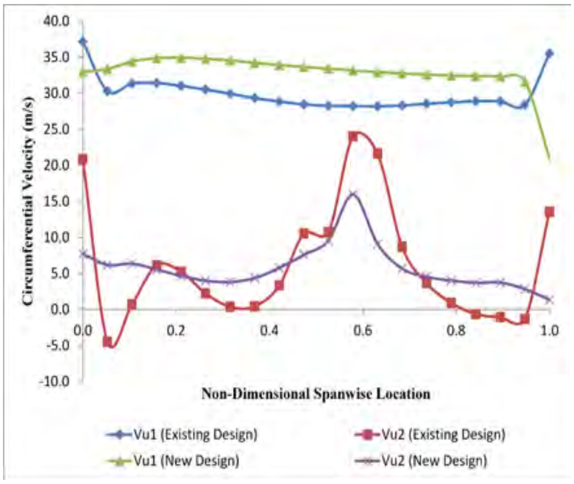

Figure 14. Circumferential velocity distribution at the inlet (V_{u1}) and outlet (V_{u2}) of the runner for the existing and new designs.

Table 5. Runner optimization through several CFD aided designs.

Version	*Changed Parameter*	*Optimization Results*	*Runner Efficiency (%)*	*Head in-out (m)*	*Power (MW)*
V01	*Beta distribution of the original runner is smoothed. NACA 0040 profile is used.*	*Rise in head and flow rate.*	*95.0*	*140.3*	*8.01*
V02	*Blade is turned into an X shape with defining 1^0 to 5^0 lean angle from leading edge*	*Improvement in pressure distribution.*	*96.1*	*143.6*	*8.27*
V03	*Blade length is shortened 2 cm. Leading and trailing edge are thickened 1 mm.*	*Decreasing the blade length decreased the friction losses. Rise in power.*	*96.2*	*144.3*	*8.32*
V04	*Blade length is shortened 2cm more. Leading and trailing edges are thickened 2 mm.*	*Decreasing the blade length decreased friction losses. Rise in power. Cavitation characteristics worsen.*	*96.3*	*145.6*	*8.4*
V05	*Leading edge beta values are settled to 30^0 (from V3)*	*Leading edge separations disappeared. Travelling bubble cavitation is observed. Power decreased.*	*95.6*	*143.6*	*8.23*
V06	*Meridional profile is tightened by decreasing the beta angles from hub and shroud layers 3^0 to 7^0.*	*Power and efficiency increased. Velocity vectors are improved.*	*96.0*	*143.4*	*8.24*
V07	*Blade theta distribution is linearized.*	*Improvement in cavitation characteristics, drop in performance.*	*95.2*	*140.6*	*8*
V08	*Trailing edge beta angles are changed between 11^0-19^0 (from V6)*	*Improvement in power and efficiency; however, no important change in cavitation characteristics, separations are seen.*	*96.8*	*142.6*	*8.26*
V09	*Leading edge beta angles are increased 5^0 for all layers*	*Leading edge cavitation. No important change in performance*	*96.8*	*142.5*	*8.26*
V10	*Stronger X-Blade design*	*For several layers, separations disappear. Efficiency increases. (From V 6)*	*96.4*	*143.2*	*8.26*
V11	*Meridional profile is widened by decreasing the beta angles from hub and shroud 10^0.*	*Power and efficiency drop*	*95.3*	*141.8*	*8.1*
V12	*The change is made on V8. Blade trailing edge beta values are increased 3^0*	*Improvement in cavitation characteristics and drop in power.*	*96.8*	*140.8*	*8.15*
V13	*The change is made on V8. Blade trailing edge beta values are increased 1^0*	*Improvement in cavitation characteristics and drop in power.*	*96.8*	*140.7*	*8.16*
V14	*Second layer beta values are increased 2^0*	*More homogenous V_m and V_u distribution. The performance is similar to V11.*	*95.4*	*141.3*	*8.08*
V15	*The change is made on V12. Second layer beta values are increased 5^0*	*Separations increased, drop in head and power.*	*96.1*	*138.6*	*7.98*
V16	*The change is made on V13. Leading edge beta values are decreased and linear distribution is ensured*	*Separations substantially decrease. Performance is improved.*	*96.8*	*141.6*	*8.21*
V17	*Guide vane angle is settled to 16.3^0 (From V16)*	*Stagnation point is at the blade tip, drop in power, separations reappear.*	*96.7*	*140.9*	*8.16*
V18	*Blade thickness profile is turned to a NACA profile*	*Better cavitation characteristics, efficiency decreases.*	*96.4*	*140.8*	*8.13*
V19	*10^0 leaning is defined from shroud layer in the rotation direction*	*Better cavitation characteristics and drop in power.*	*96.5*	*140.5*	*8.12*
V20	*5^0 leaning is defined from shroud layer in the rotation direction (Based on V16)*	*Better cavitation characteristics and no change in power.*	*96.6*	*140.1*	*8.11*
V21	*5^0 leaning is defined from shroud layer in the reverse of the rotation direction (Based on V16)*	*Power rises and adverse impact on cavitation characteristics*	*96.3*	*142.6*	*8.22*
V22	*10^0 leaning is defined from shroud layer in the reverse of the rotation direction (Based on V16)*	*Power rises and adverse impact on cavitation characteristics*	*95.5*	*144.2*	*8.25*
V23	*Leading edge beta values are decreased 2^0 for central layer (Based on V19)*	*Uniform velocity distribution. Head losses are decreased.*	*96.0*	*143.5*	*8.25*
V24	*Leading edge beta values are decreased 4^0 for central layer (Based on V23)*	*Cavitation characteristics get worse.*	*95.8*	*145.0*	*8.33*
V25	*Beta values are decreased 6^0 for middle layer. (Based on V23)*	*Non-uniform pressure distribution.*	*96.6*	*144.7*	*8.36*
V26	*Guide vane angle is changed to 16^0. (Based on V23)*	*Better velocity distribution and cavitation properties.*	*96.8*	*144.6*	*8.38*
V27-V40	*Leading edge beta angles settled to their optimum values*	*Required performance is obtained with no separation phenomena*	*96.9*	*143.9*	*8.33*

Full turbine analyses are performed and power versus efficiency graph is obtained for different guide vane angles. The modification of guide vane and efficiency brings 3% efficiency gain to the system on average. Fig. 15 shows the efficiency versus power values for a head of 167 m as a representative graph for the efficiency gain.

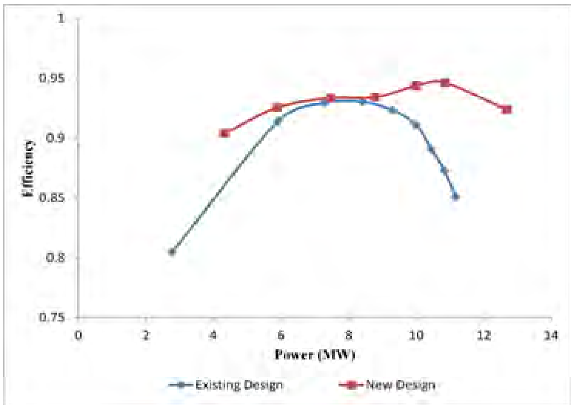

Figure 15. KEPEZ-I efficiency gain with new runner and guide vane design (for 167 m head)

Fig. 16 shows that static pressure decreases from the leading edge to the trailing edge on both suction and pressure sides. The pressure difference between these two sides generates angular momentum and it imparts a rotational motion to the turbine. Suction side trailing edge has the lowest pressure values which can lead to cavitation damage at the runner. In the existing design, there is an insufficient pressure distribution on the suction side of the blade especially close to the shroud, which causes trailing edge cavitation.

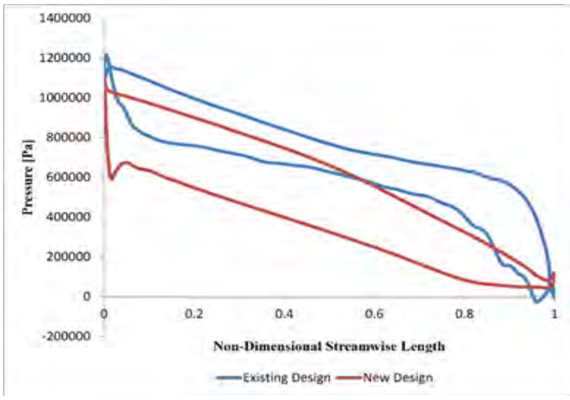

Figure 16. Blade loading for the existing and new designs (80% span)

Full turbine analyses are carried out for different heads and guide vane openings with new guide vane and runner design. A hill chart is generated as shown in Fig. 17. Head range of the turbine is changed between 141 m to 167 m and guide vane opening is changed from 15^0 to 30^0. 40 full turbine analyses are conducted to observe the behavior of the turbine for different flow rate and head combinations. When pure hydraulic efficiency without leakage and disk friction and losses is taken into consideration, maximum efficiency value reaches 94.54%.

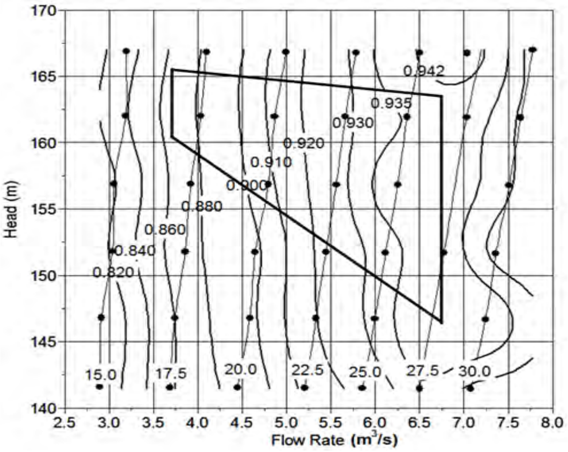

Figure 17. Hill chart for the new design

Cavitation damage is an important problem in the existing design. New design prevents cavitation damage. Figure 18 shows pressure distribution for the newly designed blade. The pressures are higher than the vapor pressure. Fig. 19 shows the vapor volume fraction isosurfaces. As seen in the figure, there is no vapor on the runner surface.

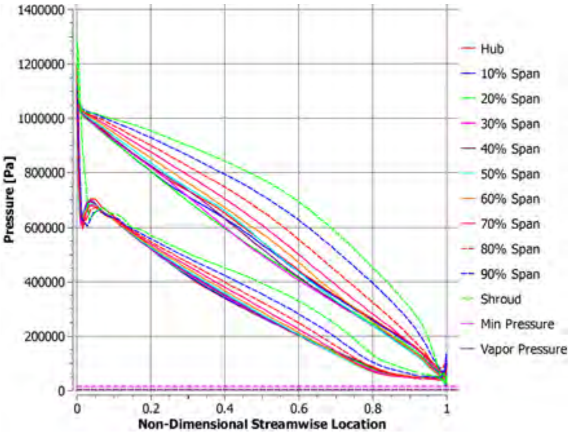

Figure 18. Pressure distribution on the new runner blade at the design condition

Figure 19. Vapor volume fraction isosurfaces on the new runner blades at the design condition

Structural analysis of the new runner and guide vane designs

The structural analyses of the guide vanes and the runner are performed using Ansys software based on Finite Element Method (FEM). Pressure distribution on the blade surface is used as input for the structural analyses. The runner blade surface is divided into eight different regions and overall pressure is identified for each region based on the blade loading. High pressure region refers to the pressure side and low pressure region refers to the suction side of the runner blade. Fixed support is used for the runner-shaft connection region. The material is selected as X3CrNiMo 13-4 (1.4313) stainless steel for the runner. The gravitational acceleration is also used in the simulations. Tensile strength of the material is 700 MPa. The results are evaluated based on the von-Mises and shear stresses. It is checked whether these stresses are below the tensile strength for structural safety. Fig. 20 shows the von Mises and shear stresses for the runner. As seen from the figure, the maximum von-Mises stress is computed to be 267 MPa. This maximum occurs on the shroud and the trailing edge. The safety factor is calculated to be 2.6 per the most critical point which shows that the blade is safe for operation. The maximum of the shear stress is 142 MPa at the same point, which is also in the safe zone.

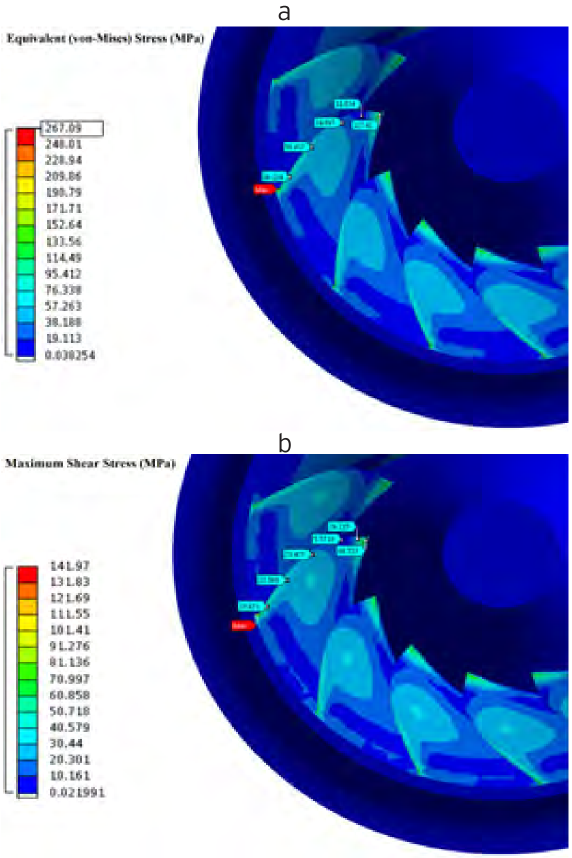

Figure 20. Stress distribution on the new runner blade, a. Von Misses stresses, b. Shear stresses

Structural analysis of the guide vane is performed using the same methodology as the runner blade. Maximum von Misses and shear stresses are computed as 278 and 157 MPa, respectively. Fig. 21 shows the stress distribution on the guide vanes. The safety factor is calculated to be 2.5 for the critical point. It is observed that the guide vane geometry is safe for operation, as well.

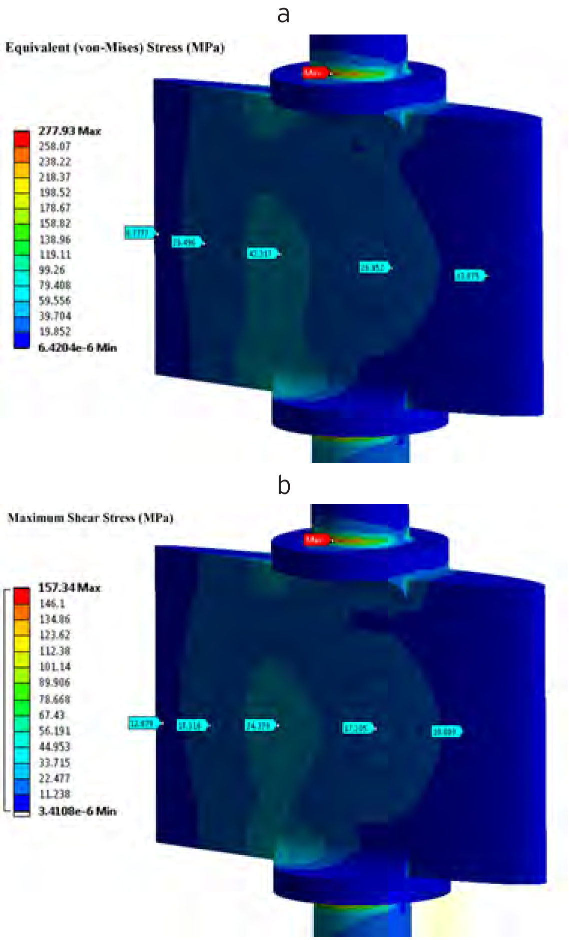

Figure 21. Stress distribution on the new guide vanes, a. Von Misses stresses, b. Shear stresses

CONCLUSION

CFD allows improvements in design. Robust, economic and efficient design can be achieved with the usage of computational techniques. Full turbine and part by part simulations of an existing turbine are performed. The design is improved with the help of computational techniques, by redesigning the guide vanes and runner of the turbine which are the only parts that are not actually buried.

The new design provides an increase in power and efficiency for the design point, as well as better cavitation characteristics. The general points of this specific rehabilitation study that can be applicable for all Francis turbine rehabilitation processes can be summarized as:

(1) Not only the technical drawings, but also the laser scanning measurements for the turbine components that will not be changed in the rehabilitation process are necessary for turbine design, since some of the parts may be different than the technical drawings because of time dependent wear of the material.

(2) Using X shaped blade runners instead of traditional runner geometries, improves the cavitation characteristics of the turbine and it contributes to efficiency and power rise.

(3) If there is a negative pressure zone which causes a reduction in the generated power and efficiency, introducing a lean from the hub in the direction of rotation can result in an increase in performance.

(4) To compare the conventional and the new state of the art CFD aided design, the best way is to generate a hill chart using the simulation results for many operating points including the design point, as with a hill chart, not only operating point but also operating region and part load behaviors of the turbine can be investigated.

The work is limited to steady-state simulations since full turbine analyses are performed for both design and off-design conditions. The next step in terms of the computational study is to perform unsteady simulations to observe the time dependent nature of the flow if there is. The next step in this research is to manufacture a model and perform model tests of the designed turbine based on IEC 60193 standards.

ACKNOWLEDGEMENTS

This work is financially supported by Tübitak Kamag under grant number 113G109. The computations are performed at TOBB ETU Hydro Energy Research Laboratory (ETU Hydro) financially supported by Turkish Ministry of Development.

REFERENCES

[1] Choi HJ, Zullah MA, Roh HW, Oh SY, Lee YH. CFD validation of performance improvement of 500 kW Francis turbine. Renewable Energy, 54 (2013) 111–123.

[2] Beatove SL, Ruiz GM, Arboleda, BQ, Bustamante OS. CFD: Numerical simulations of Francis turbines. Rev. Fac. Ing Univ. Antioquia, 51 (2010) 31–40.

[3] Qian ZD, Yang J.D, Huai WX. Numerical simulation and analysis of pressure pulsation in Francis hydraulic turbine with air admission. Journal of Hydrodynamics, Ser. B 19 (2007) 467–472.

[4] Su WT, Li FC, Li BX, Wei XZ, Zhao Y. Assessment of LES performance in simulating complex 3D flows in turbo–machines. Engineering Applications of Computational Fluid Mechanics, 6(3) (2012) 356-365.

[5] Patel K, Desai J, Chauhan V, Charnia S. Development of Francis turbine using Computational Fluid Dynamics. 11st Asian International Conference on Fluid Machinery and 3rd Fluid Power Technology Exhibition, 2011.

[6] Kaniecki M, Lojek A, Hajdarowicz M. Rehabilitation of medium–head hydropower plants with exploited Twin–Francis Turbines, Congress SHP, 2014.

[7] Akin H, Aytac Z, Ayancik F, Ozkaya E, Arioz E, Celebioglu K, Aradag, S. A CFD aided hydraulic turbine design methodology applied to Francis turbines. IEEE 4th International Conference on Power Engineering, Energy and Electrical Drives (POWERENG), 2013.

[8] Gohil PP, Saini RP. CFD: Numerical analysis and performance prediction in Francis turbine. IEEE 1st International Conference on Non–Conventional Energy (ICONCE), 2014.

[9] Shukla MK, Jain R, Prasad V, Shujla SN. CFD Analysis of 3–D Flow for Francis Turbine, MIT International Journal of Mechanical Engineering, 1 (2011) 93–100.

[10] Bornard L, Debeissat F, Labrecque Y, Sabourin M, Tomas L. Turbine hydraulic assessment on optimization in rehabilitation projects. IOP conference series: Earth and Enviromental Science, 22 (2014).

[11] Xi–de L, Yuan H. Numerical simulation–driven hydrodynamic optimization for rehabilitation and upgrading of hydro turbines. Power and Energy Engineering Conference, Asia–Pacific, 2009.

[12] Michel B, Kunz T. Rehabilitation of hydro generating units. Power Russia Conference, Moscow, Russia, 2006.

[13] Sepetci, G, Cetinturk H, Ozkan SY, Yuksel O, Karadeniz C, Celebioglu K, Tascioglu Y, Aradag S. Conceptual design of a hydroelectric power plant for a rehabilitation project. HEFAT 2016 conference, Malaga, Spain, 2016.

[14] Ansys CFX Users's Manual v16, 2016.

[15] Keck H, Sick M. Thirty years of numerical flow simulation of Francis Turbines. Rev. Fac. Ing. Univ. Antioquia, 51 (2010) 34–33.

[16] Lenarcic M, Eichhorn M, Schoder SJ, Bauer C. Numerical investigation of a high head Francis turbine under steady operating conditions using foam–extend, Journal of Physics: Conference Series, 2015.

[17] Tonello N, Eude Y, Meux BL, Ferrand M. Frozen Rotor and Sliding Mesh Models Applied to the 3D Simulation of the Francis–99 Tokke Turbine with Code_Saturne, IOP Conf. Series: Journal of Physics: Conf. Series, 2017.

[18] Laouari A, Ghenaiet A. Simulations of Steady Cavitating Flow in a Small Francis Turbine, International Journal of Rotating Machinery, 2016.

[19] Kapoor H. Open Source Mesh Generation and CFD Simulations for Francis Turbine. MSc Thesis, Chalmers University of Technology, Sweden, 2014.

[20] Ayli E, Celebioglu K, Aradag S. Determination and generalization of the effects of design parameters on Francis turbine runner performance. Engineering Applications of Computational Fluid Mechanics, 10 (1) (2016) 547–566.

[21] Ayli E, Kaplan A, Cetinturk H, Kavurmaci B, Demirel G, Celebioglu K, Aradag S. CFD analysis of 3D flow for 1.4 MW Francis turbine and model turbine manufacturing. 35th Computers and Information in Engineering Conference, Boston, MA, USA, 2015.

[22] Michel B, Couston M, Francois M. Hydro turbines rehabilitationperformance. Engineering Applications of

Computational Fluid Mechanics, 10 (1) (2016) 547–566.

[23] Billda, J T, Holt BG. Three Gorges Project: Review of GE Energy Norwy's hydraulic design. Symposium on Hydraulic Machinery and Systems, 20th IAHR Symposium, Charlotte, NC, USA, 2010.

[24] Brekke H. Design, performance and maintenance of Francis turbines. Global Journal of Researches in Engineering, Mechanical and Mechanics Engineering, 13 (5) (2013).

[25] Krivchenko GI. Hydraulic machines: turbines and pumps. Boca Raton, FL: Lewis publishers, 1994.

Hittite Journal of Science and Engineering, 2018, 5 (1) 49-55
ISSN NUMBER: 2148-4171
DOI: 10.17350/HJSE19030000077

Synthesis, characterization and electrochemical performance of Nb doped $LiFePO_4/C$ cathodes

Cengiz Bağcı and **Öncü Akyıldız**
Hitit University, Department of Metallurgical and Materials Engineering, Corum, TURKEY.

Article History:
Received: 2017/08/14
Accepted: 2017/10/11
Online: 2018/03/28

***Correspondence to**: Cengiz Bağcı*
Department of Metallurgical and Materials Engineering, Hitit University, 19030, Corum, Turkey.
E-Mail: cengizbagci@hitit.edu.tr

ABSTRACT

We synthesized Nb-doped $LiFePO_4/C$ nano composite cathode materials by mechanochemical activation followed by a single step calcination. The starting chemicals of Li_2CO_3, $FeC_2O_4.2H2O$, $NH_4H_2.PO_4$ and $C_6H_8O_7$ as lithium, iron, phosphate, and carbon sources are mixed in a high energy ball mill (250 rpm, 5h) and calcined at 650 °C and 10 hours. The resultant materials are structurally (XRD, SEM, TEM) and electrochemically characterized and high purity $LiFePO_4$ with high electrochemical performance is obtained. Voltage vs. specific capacity, discharge capacity vs. cycle number in manufactured battery is presented. An initial specific discharge capacity of 153 $mAhg^{-1}$ and a specific discharge capacity of 128.4 $mAhg^{-1}$ after the 8th charge/discharge cycling at 1C is recorded.

Keywords:
$LiFePO_4$, Lithium ion battery, Mechanochemical activation, Nb doping

INTRODUCTION

Rechargeable lithium-ion battery with lithium iron phosphate ($LiFePO_4$, LFP) cathode has found worldwide use in the consumer electronics, hybrid and electric automotive sectors due to its long cycle life, thermal stability, and high reliability. Cathodes consisting of LFP particles can achieve high charge/discharge rates and capacity, only if a conductive carbon mesh covers the surface of the particles to provide electronic conduction between the particles and if the distance between the particles is reduced to decrease the diffusion path. Accordingly, it has been shown that composite cathode batteries consisting of carbon coated nano-sized LFP particles can reach high charge / discharge rates and capacities [1]. Moreover, doping of metal ions (such as ions of Nb, V, Mg, etc.) are also used to distort the olivine lattice of LFP and result in an increased Li-ion transport and conductivity [2].

There are several solid-state and solution-based production methods available for the production of this cathode material, yet one of the most frequently used method is the mechanochemical activation [3]. The method is based on the principle of increasing the chemical reactivity of the mixture in a high-energy ball milling through attritors. By this method powders with low particle size and high surface area can be prepared. Similarly, LFP powders prepared by mechonochemical activation reported to have high purity, uniform and well-crystallized structure and exhibit high specific capacity as detailed in the following paragraph.

Franger et al. [4] observed formation of well crystallized, phase pure homogeneous $LiFePO_4/C$ particles after adding sucrose to iron (II) phosphate ($Fe_3(PO_4)_2.5H_2O$), tri-lithium phosphate (Li_3PO_4) starting materials, milling 24 hours in planetary ball mill and calcining them at 550 ° C for 15 minutes under nitrogen atmosphere. Crystallization occurred at low temperature (432 ° C) due to deep grinding. In another work, Franger et al. [5] produced same material using saccharose and boron phosphate (BPO_4) for enhancing electronic conductivity and reported an improved electrochemical performance. Park et al. [6] observe that wet-mechanochemical activation in acetone provides approximately 74% capacity increase over dry grinding. Shin et al. [7] characterized carbon coated and chromium doped $LiFePO_4$ materials synthesized by mechanochemical activation and calcination of lithium carbonate (Li_2CO_3), iron oxalate dihydrate

($FeC_2O_4.2H_2O$) and ammonium dihydrogen phosphate ($(NH_4)_2.PO_4$) starting materials. Compared to bare $LiFePO_4$, carbon coated $LiFePO_4$ showed a significant increase in the rate performance, while the highest enhancement was achieved in Cr doped and carbon coated $LiFePO_4$. Li et al. [8] investigated the electrochemical properties of $LiFe_{1-x}Mn_xPO_4/C$ (glucose as carbon source) composite material produced by Mn addition during mechonochemical activation. It is observed that Mn doping improve electrochemical performance especially at high charge/discharge rates. Park et al. [9] investigated the main causes of the increase in the charge/discharge rate with the Al^{3+}, Cr^{3+} ve Zr^{4+} cation doping on the LFP samples produced by a single calcination step after mechanochemical activation. To this end, the bonding energies of $LiFePO_4/C$ and $LiFe_{0.97}M_{0.03}PO_4/C$ (M=Al^{3+}, Cr^{3+}, Zr^{4+}) materials were measured by XPS. The weakening of the Li-O bond and the facilitation of lithium diffusion have been reported as the main cause of the increase in rate performance with metal addition. Similarly, Ma et al. [10], Zhou et al. [11], and Zhao et al. [12] have prepared Nb doped $LiFePO_4/C$ powders with improved electrochemical activity.

The mechanochemical method is also used as a second process to reduce the particle size or to obtain a composite powder for powders previously produced by other methods. For example, Morales et al. [13] compared the performance $LiFePO_4$ particles after applying mechanochemical activation. Some of the most commonly used starting materials in the literature for the production of $LiFePO_4$ by mechanochemical activation are lithium carbonate (Li_2CO_3), iron oxalate dihydrate ($FeC_2O_4.2H_2O$) and ammonium dihydrogen phosphate. Table 1 provides a list of references that have been compiled for mechanochemical activation of these materials.

In Table 1, parametric studies carried out on the amounts of carbon and additive metal, ball to powder ratio or calcination temperature is listed. Table 2 gives the

Table 1. A list of elements used in lithium, iron, phosphate, carbon sources and doping elements used for LFP - LFP/C synthesis by mechanochemical activation method. Thermal and structural analysis methods can be read from the relevant columns.

#	Source of				Dopant	Thermal analysis*	Structural analysis*	Reference
	Li	Fe	PO_4	C*				
1	Li_2CO_3	FeC_2O_4•$2H_2O$	$NH_4H_2PO_4$	CB	Cr^{3+}	-	isXRD,SEM	[7]
2				-	-	-	XRD,HRTEM	[6]
3				CB	Cr^{3+}, Al^{3+}, Zr^{4+}	-	XRD,SEM	[9]
4				-	Nb^{5+}	-	ABF-STEM	[14]
5				CA	-	TG/DSC	XRD,FTIR,SEM	[15]
6				-	-	-	XRD	[16]
7				AC	-	-	XRD,SEM,TEM	[17]
8				-	-	-	XRD,SEM	[18]
9				-	-	-	XRD	[19]
10				-	-	TG	XRD,FE-SEM	[20]
11				-	-	TG/DTG	XRD,EDS,SEM,TEM	[21]
12				MA	-	DSC	XRD,SEM,TEM,EDS	[22]
13				MA	-	-	XRD,SEM,TEM/EDS	[23]
14				PVA	-	TG	XRD,SEM	[24]
15	LiF			-	-	TG/DSC	XRD,SEM	[25]
16	$Li(OH)H_2O$	$FePO_4$•$2H_2O$		-	-	-	-	[8]
17				CS	-	-	XRD,SEM,TEM	[26]
18	Li_2CO_3			SC		TGA	isXRD	[27]
19	Li_3PO_4	$Fe_3(PO_4)_2$•$5H_2O$		SC	-	TGA/DSC	XRD,SEM	[4]
20					-	-		[5]
21	LiH_2PO_4	Fe_2O_3	LiH_2PO_4	CA	Nb^{5+}	NA	XRD,FE-SEM	[27]

*
CA: Citric acid
CB: Carbon black
SC: Saccharose
TA: Tartaric acid
PEG: Polyethylene glycol
AC: Acetylene black
CS: Cane sugar
MA: Malic acid

TGA: Termogravimetric analysis
DTA: Differential thermal analysis
DSC: Differential scanning calorimetry
isXRD: in situ X-ray diffraction
SEM: Scanning electron microscopy
HRTEM: High resolution transmission electron microscopy
EDS: Energy dispersive spectroscopy
FE-SEM: Field emission SEM

D: Doping
C: Carbon
T: Temperature
mt: Milling time
BP: Ball/powder ratio
w: Wet milling
RT: Room temperature
atm: Atmosphere

Table 2. Details of carbon and metal doping type and amount, calcination and mechano-chemical activation methods used in the studies given in Table 1.

#	C (w %)	Dopant	Calcination			Activation				
			°C	hr	atm	b:p	hr	°C	rpm	atm
1	3	Cr^{3+}, 0.02	600/750	10	Ar+%5 H_2	20:1	3	RT	250	
2	-	-	600	10	Ar+%5 H_2	20:1	3	RT	250	
3	3	Cr^{3+},Al^{3+},Zr^{4+}	750	10	Ar+%5 H_2	20:1	3	RT	250	
4	-	Nb^{5+}, 0.02	800	10	Ar					
5	0/5/6/6.75/8	-	700	20	N_2, dyn	10:3	2	RT	400	Ar
6	-	-	700	10	Vakum		1			
7	7.8/4.7	-	600	10	N_2	10:3	15	RT	1000	Ar
8	-	-	600+700	0.5	N_2		2			
9	-	-	400/600	2/4	Ar	20:1/40:1	0.5		660	
10	-	-	50+350+650	16+4+10	Ar+%5 H_2		24			
11	-	-	350+600+800	8+8	Ar	1:20	2			
12	50	-	873	12	Ar+%5 H_2	1:20	3/12/18		300	
13	60	-	60+320+600	10+12	Ar+%5 H_2		3			
14	0/1/3/5/10/30	-	800/300+800/500+800	9/6+9	Ar		24			
15	-	-	300/400/500/600/700/800	8/24	Ar+%8 H_2					
16		-								
17	20	-	60+650	8.5	N_2	15/20/25/30:1	2.5		3000	
18	-	-	500+120+600	6+5	Ar		2		450	
19	-	-	550	0.25	N_2		24			
20	-	-	700		N_2					
21	5	Nb^{5+},0.005/0.01/0.015/0.025	700	12/4	N_2		5/6			

details of carbon and metal doping sources and amounts, calcination and mechanochemical activation methods for the studies given in Table 1.

In light of the literature review presented above, the aim of this work is to produce $LiFePO_4$/C nano composite cathode material with high purity and high electrochemical performance using the mechanochemical activation method by selected process parameters from Table 1 and 2.

MATERIALS AND METHODS

Lithium carbonate (Li2CO3, Abcr, Germany), iron oxalate dihydrate (FeC2O4.2H2O, Alfa Aesar, USA) and ammonium dihydrogen phosphate (NH4H2.PO4, Merck, Germany) were used as lithium, iron and phosphate sources respectively. Citric acid (C6H8O7, Merck, Germany) was used as a carbon source and niobium pentaoxide (Nb2O5, Sigma Aldrich, USA) as a niobium source. These precursor materials were mixed in stoichiometric

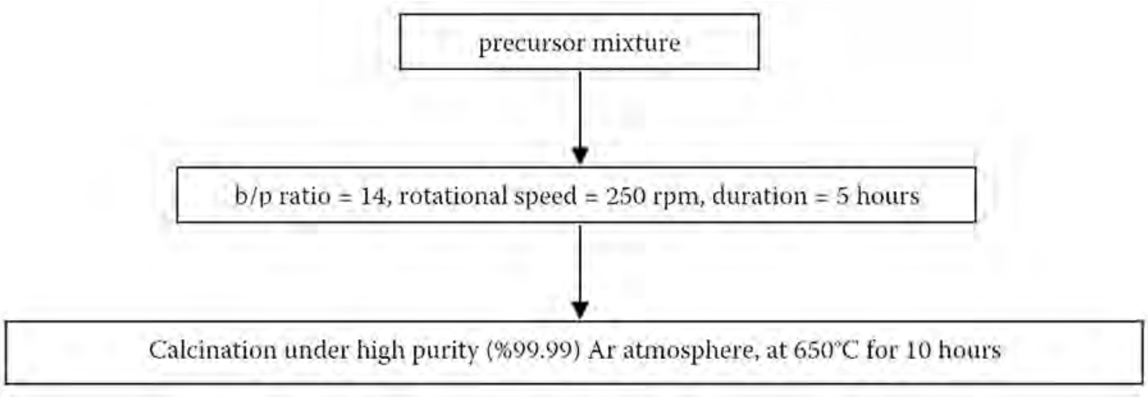

Figure 1. Flowchart of the synthesis method.

amounts for 2.4 at. % Nb and at. 6.4% carbon and then ball-milled for 5 h in a planetary mill using zirconium dioxide vessel and balls (diameter 10mm) with a ball to powder ratio of 14.0. The resulting mixture was calcined in a tubular furnace (Protherm PTF 16/75/450) under argon flow at 650 °C for 10 h in order to obtain the Nb-doped LiFePO4/C composite powders. Flowchart for the synthesis method is presented in Fig. 1.

XRD analysis was performed using a Bruker D8 Advance diffractometer equipped with a Cu Kα source (λ = 0.15406 nm). Tests were carried out at 40 kV, 30 mA, and the Bragg angle (2θ) varied from 5° to 80° with a scan rate of 1°/min. Powder morphologies were investigated using a SEM (FEI / Quanta 450 FEG) and TEM (FEI-TECNAI).

Cast electrodes were prepared from a 500 mg mixture of 85 wt % of LFP/C active material, 10 wt % of carbon black (Abcr, Germany) conductive additive and 5 wt % of PVDF (polytetrafluoroethylene, (Sigma Aldrich, USA) binder was mixed in N-methylpyrrolidone (NMP, Merck, Germany) for 1.5 hours to obtain a thick slurry. This slurry was then cast on an aluminum foil with a blade spacing of 100 µm and dried in an oven at 100° C for 12 hours. Discs of 9.525 mm in diameter punched from these films in glove box (Inert I-Lab 2GB) were used as cathode. For anode, discs were cut from a metallic lithium rod (Alfa Aesar, USA) with a diameter of 12.7 mm. 1M $LiPF_6$ (lithium hexafluorophosphate, Abcr, Germany) solution in 1:1 ethylene carbonate ($C_3H_4O_3$, Abcr, Germany): dimethyl carbonate ($C_5H_{10}O_3$, Abcr, Germany) was prepared as the liquid electrolyte.

Cathode and anode discs, bottom and top covers of CR2032 button battery cell, spring and spacers and electrolyte-impregnated (16 mm in diameter) glass fiber filter paper separator (691 VMR, France) were assembled using an electric coin cell crimping machine (MTI – MSK-160D) inside the glovebox. The electrochemical measurements were conducted with a custom designed (max. 30mV) battery tester (UBA 5, Vencon Technologies, Canada).

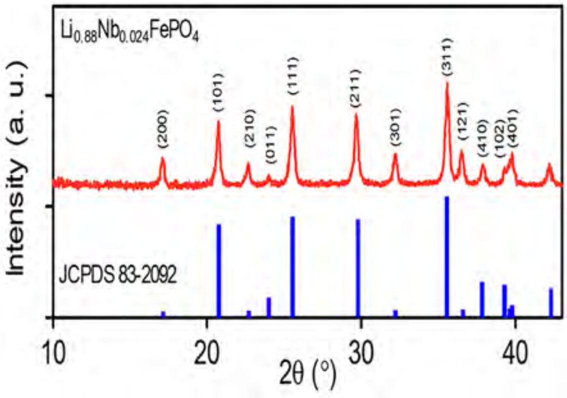

Figure 2. XRD pattern of 2.4% Nb-doped $LiFePO_4$/C powders.

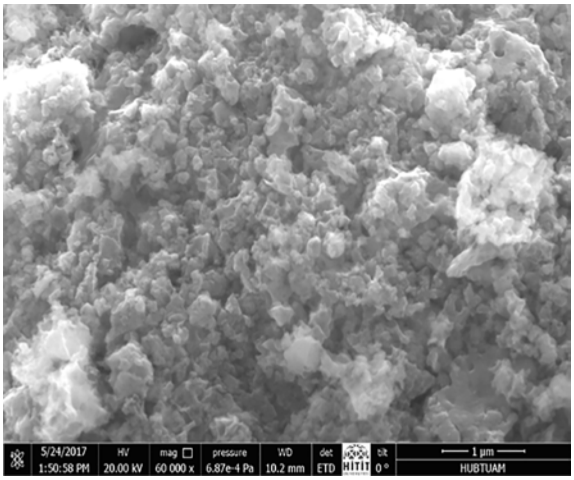

Figure 3. SEM image of 2.4% Nb-doped LiFePO4/C powders.

In order to determine the specific capacity of the cell, weight of the electrode disc with the current collector (W_{ED}), weight of the uncoated current collector disc of the same diameter (W_{CC}) were measured and weight of electrode material were calculated by taking their difference. Then the weight of active material in the electrode is calculated by: W_{AM} = 85 % (W_{ED} - W_{CC}). Multiplying this value with the theoretical specific capacity of LFP (C = 170 $mAhg^{-1}$) the theoretical specific capacity of the electrode disc (C_{ED}) is obtained: C_{ED} = C x W_{AM} [28]. Then the coin cell was first charged under a constant voltage of 3.6V, rested for five minutes and discharged at constant current at 1C (discharge in 1 hour). This charge and discharge cycle has been repeated eight times.

RESULTS AND DISCUSSION

Fig. 2 shows the XRD pattern of 2.4 at. % Nb-doped $LiFePO_4$/C powders. The crystal phase is ordered olivine structure indexed orthorhombic Pnma, and no other impurity peak is detected. Comparing the $Li_{1-5x}Nb_xFePO_4$ (x=0.024) pattern with that of JCPDS card number 83-2092, one can conclude that doping this amount of Nb do not affect the structure of the sample. Yet considering the ionic radii of Nb5+ (78 pm) is larger than that of Li+ (68 pm), the enlarged crystal cell volume with Nb ion doping is expected to improve the lithium ion diffusivity [27] and in turn electrochemical performance.

The crystallite diameter (d) was calculated from the XRD line width using the Scherrer equation, d = 0.9λ/($\beta_{1/2}$ cosθ), where λ is the X-ray wavelength, $\beta_{1/2}$ is the calculated width at half-maximum of the diffraction peak, and θ is the diffraction angle. Value of d is measured at the angle corresponding to the (311) line and found as 52 nm.

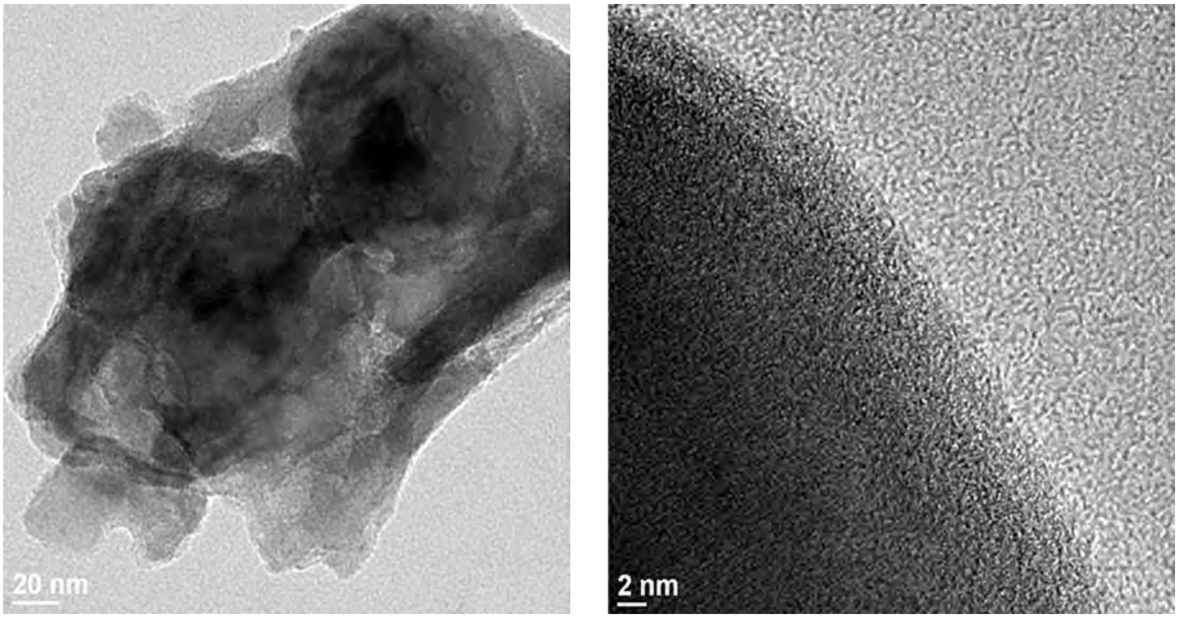

Figure 4. TEM images of 2.4% Nb-doped LiFePO4/C powders.

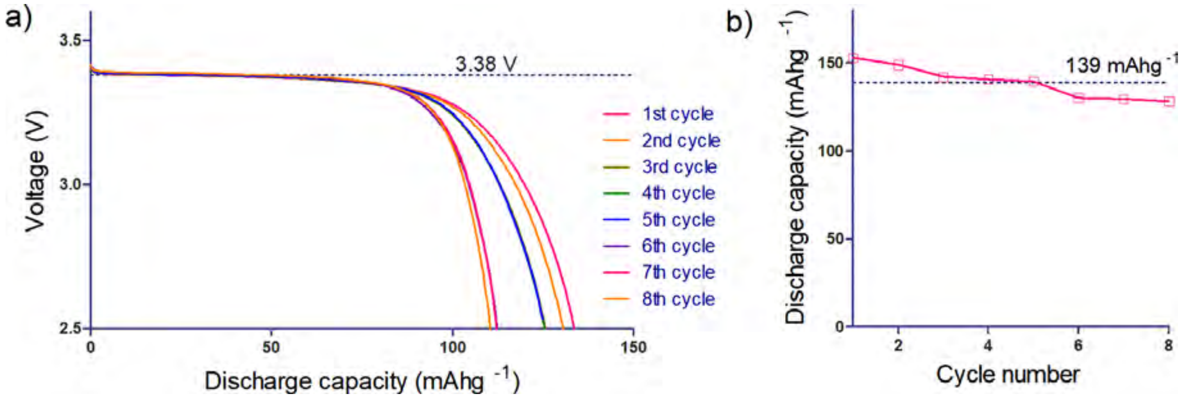

Figure 5. a) Discharge curves and b) cycle life performance of CR2032 button battery cell with a positive electrode prepared from 2.4 at. % Nb-doped LiFePO$_4$/C powders operated between 3.5 and 2.5 V at the current rate of 1 C.

Fig. 3 shows the scanning electron microscopy (SEM) image of 2.4 at. % Nb-doped LiFePO$_4$/C powders, where powders are consisting of agglomerated particles.

Fig. 4 shows the TEM images of 2.4 at. % Nb-doped LiFePO$_4$/C powders where it seen that the particles are coated and connected by carbon. Fig. 4a confirms that the particles had a size of 50~100 nm with a circular and oval shape. The particle size reported here is in good aggrement with the calculated crystallite size (52 nm) using the Scherrer equation. From Fig. 4b, it is clear that the carbon coating is uniform, and the shell thickness of the coating is in the range of ~3 nm, indicating that carbon could inhibit the particle growth, and help in obtaining smaller particles [29].

Fig. 5a shows discharge curves of the CR2032 button battery cell with a positive electrode prepared from 2.4 at. % Nb-doped LiFePO4/C powders. The discharge capacity at the rate 1 C, was about 139 mAhg^{-1} between a cutoff voltage of 2.5 and 3.5 V. Also, a good voltage plateau was observed at about 3.4 V (vs. Li/Li+). Fig. 5b shows the cycle performance at 1 C rate. An initial specific discharge capacity of 153 mAhg^{-1} and a specific discharge capacity of 128.4 mAhg^{-1} is recorded after the 8th charge/discharge cycling.

CONCLUSION

We synthesized Nb doped LiFePO$_4$/C nano composite cathode materials by mechanochemical activation at 250 rpm for 5 hours followed by a calcination at 650 °C for 10 hours. The resultant materials are structurally (XRD, SEM, TEM) and electrochemically characterized. LFP with high electrochemical performance is obtained. The discharge capacity at the rate 1 C, is about 139 mAhg^{-1}

and a good voltage plateau is observed at about 3.4 V (vs. Li/Li+). A specific discharge capacity of 128.4 mAhg^{-1} is recorded after the 8th charge/discharge cycling at 1C.

ACKNOWLEDGEMENTS

This work was supported by the Hitit University Scientific Research Projects Funding Program through a research Grant No. MUH190001.15.02. The authors wish to thank Prof. I. Sonmez for his interest in this work and Res. Assts. B. Alkan and D. Candemir of Hitit University for their help with the laboratory instruments.

REFERENCES

1. Xie G, Zhu H–J, Liu X–M, and Yang H. A core-shell LiFePO4/C nanocomposite prepared via a sol-gel method assisted by citric acid. Journal of Alloys and Compounds 574 (2013) 155-160.
2. Johnson ID, Blagovidova E, Dingwall PA, Brett DJL, Shearing PR. Darr JA. High power Nb–doped LiFePO4 Li–ion battery cathodes; pilot–scale synthesis and electrochemical properties. Journal of Power Sources 326 (2016) 476e481
3. Toprakci O, Toprakci HAK, Ji L, Zhang X. Fabrication and electrochemical characteristics of LiFePO$_4$ powders for lithium–ion batteries. Kona Powder and Particle Journal 28 (2010) 50–72.
4. Franger S, Cras FL, Bourbon C, Rouault H. Comparison between different LiFePO4 synthesis routes and their influence on its physico–chemical properties. Journal of Power Sources 119-121 (1) (2003) 252-257.
5. Franger S, Benoit C, Bourbon C, Cras FL. Chemistry and electrochemistry of composite LiFePO4 materials for secondary lithium batteries. Journal of Physics and Chemistry of Solids. 67 (5–6) (2006) 1338-1342.
6. Park CK, Hwang JT, Cho WI and Jang H. The origin of the residual carbon in LiFePO4 synthesized by wet milling. Bull Korean Chem Soc. 32 (2) (2011) 536–540.
7. Shin HC, Park SB, Jang H, Chung KY, Cho WI, Kim CS, Cho BW. rate performance and structural change of cr–doped LiFePO4/C during cycling. Electrochemica Acta 53 (2008) 7946-7951.
8. Li C, Hua N, Wang C, Kang X. Effect of Mn^{2+} doping in LiFePO4 and the low temperature electrochemical performances. Journal of Alloys and Compounds 509 (2011) 1897-1900.
9. Park CK, Park SB, Park CH, Shin HC, Cho WI and Jang H. The root cause of the rate performance improvement after metal doping: a case study of LiFePO4. Bull Korean Chem Soc. 32 (3) (2011) 921–926.
10. Ma Z, Shao G, Wang G, Zhang Y and Du J. Effects of Nb–doped on the structure and electrochemical performance of LiFePO$_4$/C composites. Journal of Solid State Chemistry 210 (1) (2014) 232-237.
11. Zhang, Q, Wang S, Zhou Z, Ma G, Jiang W, Guo X, Zhao S. Structural and electrochemical properties of Nd–doped LiFePO4/C prepared without using inert gas. Solid State Ionics 191 (2011) 40–44.
12. Zhuang D, Zhao X, Xie J, Tu J, Zhu T, Cao G. One–step Solid–state Synthesis and Electrochemical Performance of Nb–doped LiFePO4/C. ActaPhys.Chim.Sin. 22 (2006) 840-844.
13. Morales J, Trócoli R, Rodríguez–Castellón E, Franger S, Santos–Peña J. Effect of C and Au additives produced by simple coaters on the surface and the electrochemical properties of nanosized LiFePO4. Journal of Electroanalytical Chemistry 63 (2009) 29-35.
14. Suo L, Han W, Lu X, Gu L, Hu YS, Li H, Chen D, Chen L, Tsukimoto S and Ikuhara Y. Highly ordered staging structural interface between LiFePO$_4$ and FePO$_4$. Phys Chem Chem. Phys. 14 (2012) 5363–5367.
15. Zhang D, Yu X, Wang Y, Cai R, Shao Z, Liao X–Z, and Ma Z–F. Ball milling–assisted synthesis and electrochemical performance of LiFePO4/C for lithium–ion battery adopting citric acid as carbon precursor. Journal of the Electrochemical Society 156 (10) (2009) A802– A808.
16. Li M, Xie K, Li D, and Pan Y. Synthesis of LiFePO4 by one–step annealing under the vacuum condition. Journal of Materials Science 40 (2005) 2639-2641.
17. Kim J–K, Choi J–W, Chauhan GS, Ahn J–H, Hwang G–C, Choi J–B and Ahn H–J. Enhancement of electrochemical performance of lithium iron phosphate by controlled sol-gel synthesis. Electrochimica Acta 53 (28) (2008) 8258-8264.
18. Koltypin M, Aurbach D, Nazar L and Ellis B. More on the performance of LiFePO$_4$ electrodes—the effect of synthesis route, solution composition, aging, and temperature. Journal of Power Sources 174 (2) (2007) 1241-1250.
19. Kosova N, Devyatkina E. On mechanochemical preparation of materials with enhanced characteristics for lithium batteries. Solid State Ionics 172 (1–4) (2004) 181-184.
20. Lee J, Kumar P, Lee G, Moudgil BM and Singh RK. Electrochemical performance of surfactant–processed LiFePO$_4$ as a cathode material for lithium–ion rechargeable batteries. Ionics, 19(2) (2012) 371-378.
21. Ojczyk W, Marzec J, Świerczek K, Zając W, Molenda M, Dziembaj R and Molenda J. Studies of selected synthesis procedures of the conducting LiFePO4–based composite cathode materials for li–ion batteries. Journal of Power Sources 173(2) (2007) 700-706.
22. Fey GTK, Chen YG and Kao HM. Electrochemical properties of LiFePO$_4$ prepared via ball–milling. Journal of Power Sources 189 (1) (2009) 169-178.
23. Fey GTK and Lu TL. Morphological characterization of LiFePO$_4$/C composite cathode materials synthesized via a carboxylic acid route. Journal of Power Sources 178 (2) (2008) 807-814.
24. Yun NJ, Ha HW, Jeong KH, Park HY and Kim K. Synthesis and electrochemical properties of olivine–type LiFePO$_4$/C composite cathode material prepared from a poly(vinyl alcohol)–containing precursor. Journal of Power Sources 160 (2) (2006) 1361-1368.
25. Wang D, Li H, Wang Z, Wu X, Sun Y, Huang X and Chen L. New solid state synthesis routine and mechanism for LiFePO$_4$ using LiF as lithium precursor. Journal of Solid State Chemistry, 177(12) (2004) 4582-4587.
26. Lv YJ, Su J, Long YF, Cui XR, Lv XY and Wen YX. Effects of ball–to–powder weight ratio on the performance of LiFePO$_4$/C prepared by wet–milling assisted carbothermal reduction. Powder Technology 253 (2014) 467-473.
27. Chen Z, Ren Y, Qin Y, Wu H, Ma S, Ren J, He X, Sun YK, Amine K. Solid state synthesis of LiFePO$_4$ studied by in situ high energy x–ray diffraction. Journal of Materials Chemistry 21(15) (2011) 5604-5609.

28. Kayyar A, Huang J, Samiee M, Luo J. Construction and testing of coin cells of lithium ion batteries. J Vis Exp 66 (e4104) (2012) 1-5.

29. Kim HS, Kam DV, Kim VS, Koo HJ. Synthesis of the $LiFePO_4$ by a solid–state reaction using organic acids as a reducing agent. Ionics 17 (4) (2011) 293-297.

Hittite Journal of Science and Engineering, 2018, 5(1) 57-61
ISSN NUMBER: 2148-4171
DOI: 10.17350/HJSE19030000065

Some Geological Features of Limestone Aggregates Produced from Central Anatolian Carbonate Formations

Gürsel Kansun[1], Veysel Zedef[2] and Kerim Koçak[1]
[1]Selcuk University, Department of Geology, Konya, TURKEY
[2] Selcuk University, Department of Mining Engineering, Konya, TURKEY

Article History:
Received: 2017/05/03
Accepted: 2017/06/19
Online: 2017/12/22

Correspondence to: *Veysel Zedef,*
Selcuk University, Department of Mining Engineering 42003 Konya
Tel: +90 (332) 2232046
Fax: +90(332) 2410635
E-Mail: vzedef@selcuk.edu.tr

ABSTRACT

For the last fifteen years, there has been extensive motorway and railway constructions in Turkey. This requires enormous amount of road-fillers and aggregates, and the construction companies open many open-pit limestone quarries to fulfill their aggregate needs. The partly double (four lines), partly one-way (double line) motorway of Konya-Hüyük have recently been enlarged and partly re-constructed. During this construction, a total of five limestone quarry were opened to produce limestone aggregate. The Bozlutepe Limestone member of Asmalıtepe Formation near the town of Selki (Hüyük-Konya, central Anatolia) were used for this demand, and it has been operated for the last 6 years. The limestone member is approximately 200 m thick at most and mostly made of three type of minerals and these are dolomitic limestone, crystalline limestone and quartz-bearing crystallized limestones. All the minerals are crystallized and the minerals locally dominate at the quarry. The produced aggregates have relatively flat granulometry curve indicating most of the grains are of thin and have clay-silt sized particles. Our studies revealed that Bozlutepe Limestones are formed in carbonate facies in shallow marine environments during Permian-Carboniferous times. The member most likely have low-grade metamorphism during Paleozoic and Mesozoic eras.

Keywords:
Limestone aggregates, Bozlutepe Limestones, Granulometry curves, Konya, Turkey

INTRODUCTION

The limestones are the most important rock groups as a source of aggregates since these rocks can easily found at most places (10 % -by volume- of the sedimentary rocks are of carbonates). These rocks have a variety of uses. The most important uses are in the cement industry, road construction, the building blocks and lime manufacturing industry. The silica ratio of the cement is strongly depend on the silica contents of the limestone used as aggregates [1]. On the other hand Alhozaimy [2] stated that the water absorption capacity of limestone aggregates strictly controls the cement resistance. The grain size of limestone aggregates used in cement also controls the development of cracks system in the produced cement [3]. The biggest drawback in the use of limestone as aggregate for all purposes is the weakness against acid, especially sulfuric acid which widely available in the nature [4].

The main aim of this study is to reveal that some mineralogical, petrographic and physical features of Bozlutepe limestones which were used for local aggregates need at Yazı Places of Selki, Hüyük, Konya.

GENERAL GEOLOGY

The study area is geographically located at the southeastern tip of Sultan Dağları Mountains which geologically comprise a variety of rock units of mainly metamorphic. These rock units essentially are schists, quartzites and metamorphosed carbonates. The alluviums and rock talus are widespread in intermountain valleys and depression areas, for example east of Lake Beyşehir region and Akşehir-Eber area.

Easy crack-down of the limestones is the result of weak bond values between Ca-O-C even in the metamorphic limestones. The Bozlutepe Limestones are highly fragmented and have irregularly scattered fracture and joint systems. The unit is first described by Zedef [5] and interpreted as a member of Asmalıtepe Formation.

The Bozlutepe Limestone Member is geographically found at approximately 80 km west of Konya (Figure 1).

Figure 1. The location map of the study area.

BOZLUTEPE LIMESTONE MEMBER

Asmalı Tepe Formation covers quite large areas in the northern part of Selki (Hüyük, Konya) (formerly Selki Kasabası-Köyü) (Figure 2).

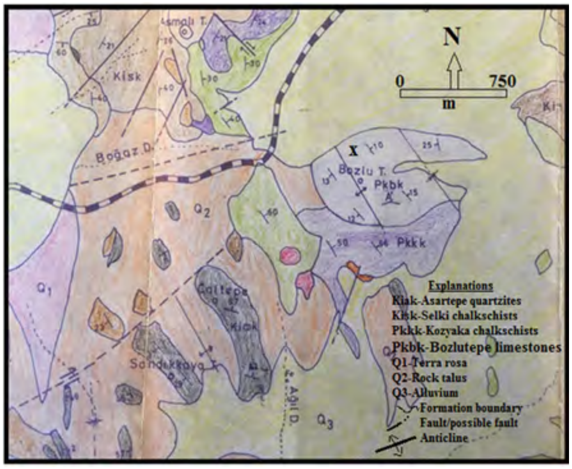

Figure 2. Geological map of the study area [5]. The Bozlutepe Limestones are shown with a light blue color on the Bozlu Tepe with the sign of Pkbk

Zedef [5] stated that the limestones composed mainly of recrystallized limestones are with 95% calcite and 5% quartz. The investigations were further elaborated and new mineralogical and petrographic findings were obtained as a result of resent observations and more representative sample compilation in open quarry for aggregate. These findings will be detailed in the following section.

At a macro-scale, the Bozlutepe Limestones are light gray, whitish and dark gray-black in places where recrystallization is severe (Figure 3). The limestones cover an area of about 1 km2 in the area. The member is intercalated with fine calcschist layers which are not locally persistent, but these are not very common. The thickness of the limestone layers (ranging from the metamorphism to the extent that the partially protected borders can be observed) generally ranges from 10 to 40 cm.

The thickness of Bozlutepe Limestone Member is determined as 150-200 m. The unit is concordant with both the Kozyaka Chalkschist member under it and the Ortaburun Limestone Member above it. The stratigraphic location of the unit is shown in detail in Figure 4.

No fossils were found that during the investigations, but [5] gave Permo-Carbonifer age to the member considering the stratigraphic position of the unit. Detailed information about the Bozlutepe limestones can be found in [5]

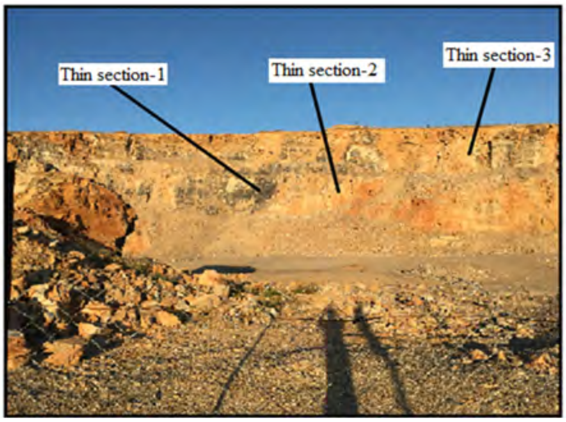

Figure 3. Open pit for the aggregate plant in Bozlutepe Limestone. Note: The locations where thin sections for petrographic-mineralogical examinations are taken are also marked. The place of this figure is indicated in Figure 2 as the point x (Just close to North of Bozlu T).

(together with the meanings of the symbols and signs used in the geological map and stratigraphic section).

MINERALOGY AND PETROGRAPHY

The Bozlutepe limestones were investigated in detail under a polarizing microscope and the following findings were obtained. The sample locations where the thin sections examined are shown in Figure-3.

Thin section-1

The rock is fine grained. Large crystals are observed in places. The rock is composed of carbonate crystals (Fig. 5-a) and locally observed stilolites. The result of the alizarin test, which was applied to the rocks, show that the rock have ~ 85% calcite and ~ 15% dolomite (Figure 5-b). The calcites in the rock are in the form of very high anhedral crystals. Dolomites are again very high double-crusted and semi-spherical and euhedral (usually romboeder) crystals (Figure 5-b).

There are some brecciation (as broken structure) in the rock and it has abundant veins. These veins contain secondary calcite and quartz crystals. Considering the mineralogical composition, the rock is called "dolomitic limestone". The rock has mostly lost its original texture. On the other hand, very few of the rocks retained their original texture properties like micritic levels. According to these properties, the rock is primarily micritic limestone. The rock was deposited in a very shallow marine environment.

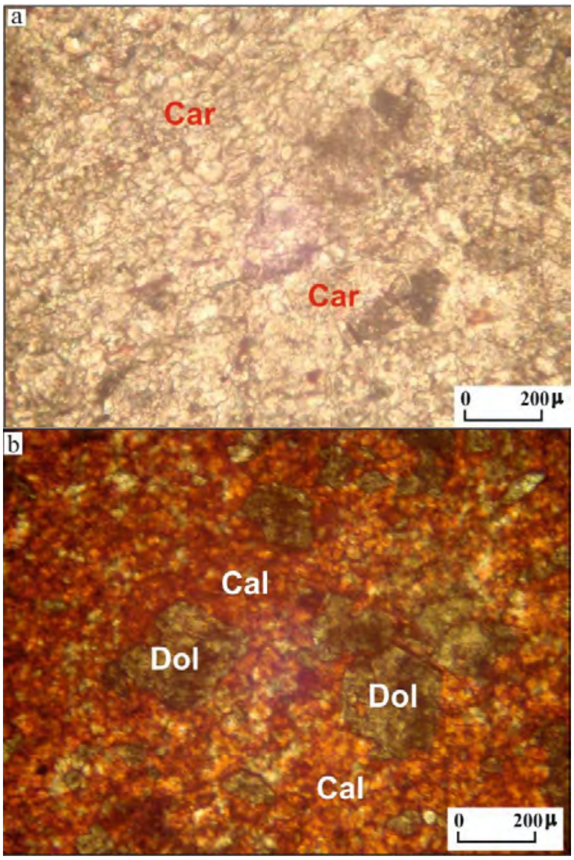

Figure 5. Thin section photograph of Bozlutepe limestones, (b): Same thin section with alizarin red. Car: Carbonate, Dol: Dolomite, Cal: Calcite (// N).reticulum. (TEM) X 20 000.

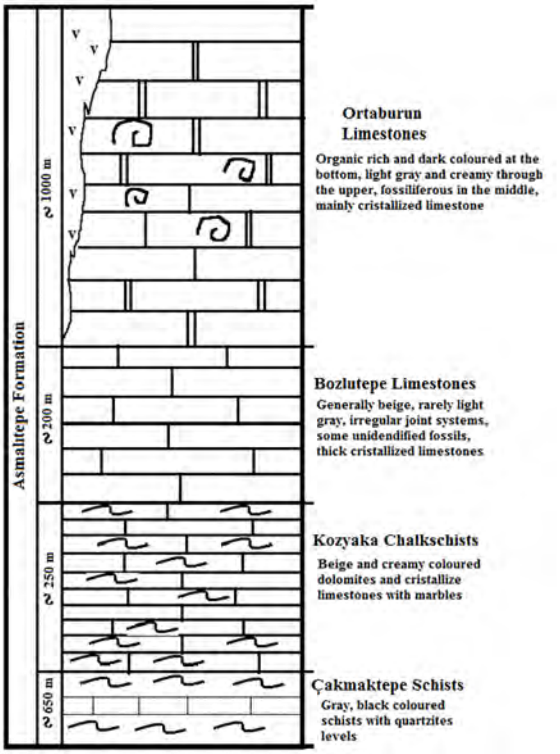

Figure 4. Stratigraphic column section of Bozlutepe Limestone [5]. For details, please see Figure 2-explanations [5]

Thin section-2

The rock is medium granular. According to the modal analysis result, it is composed of ~ 98% carbonate and ~ 2% quartz crystals (Figure 6-a). The result of the test of the alizarin red reveal that the entire carbonates are in the form of calcite (Fig. 6-b). Calcite is anhedral and has very high double-refraction. In the rock, coarse-grained secondary calcite crystals are observed in the form of void fill (patch) in small quantities. Considering the mineralogical composition, the rock is called "crystallized limestone". The rock has completely lost its original texture. The rock was deposited in shallow marine conditions in a relatively deep shelf environment.

Thin section-3

The rock is fine grained and the modal analysis result shows that the rock have ~ 99% carbonate and ~ 1% quartz crystals (Figure 7-a). It is seen that ~ 97% of the carbonate minerals in the rock are calcite and ~ 2% dolomite (Figure 7-b). Of these carbonate minerals with very high double-refraction, calcite is characterized

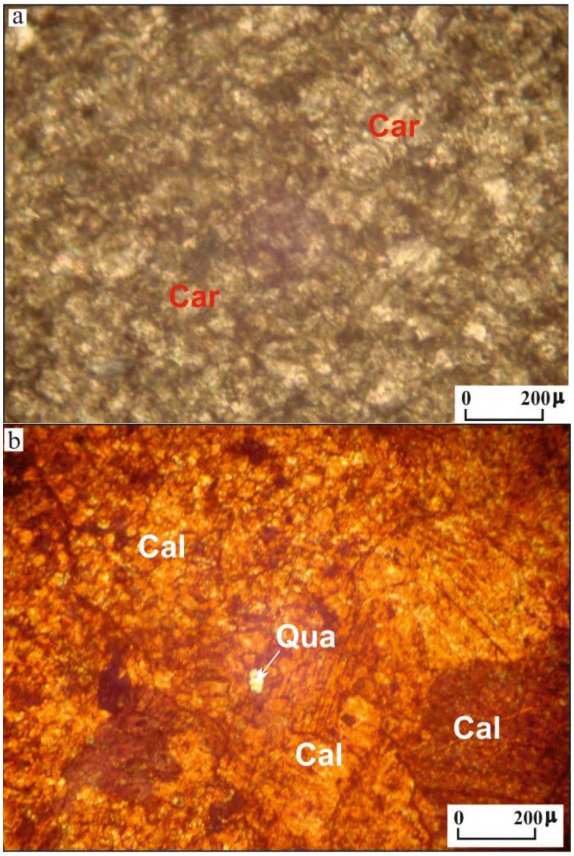

Figure 6.(a): Microphoto of Bozlutepe limestones, (b): Alizarin-red test applied to the same rock. Car: Carbonate, Qua: Quartz, Cal: Calcite (// N).

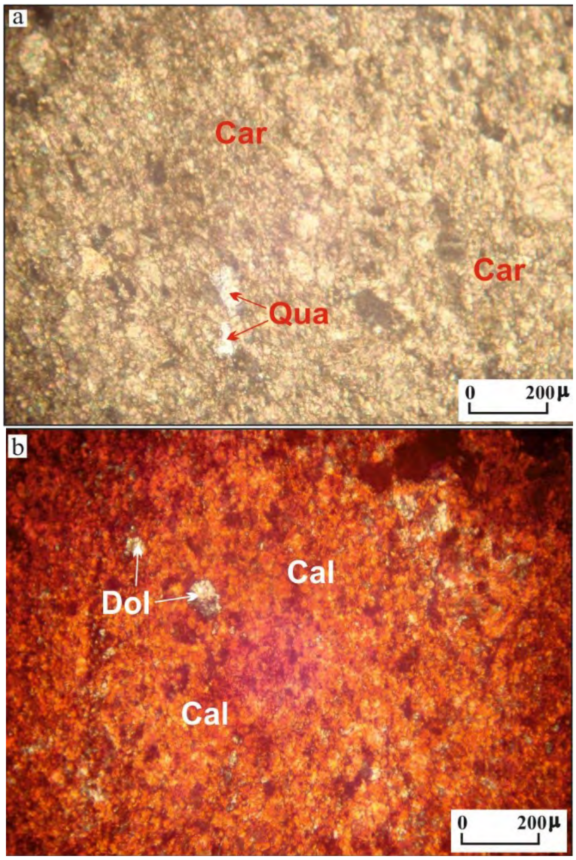

Figure 7.(a): Thin section photograph of Bozlutepe limestones, (b): Same thin section with alizarin red. Car: Carbonate, Dol: Dolomite, Cal: Calcite (// N).

by anhedral crystals and dolomite is characterized by semispherical-euhedral (romboeder-shaped) crystals. Considering the mineralogical composition, the rock is called "crystallized limestone".

The rock has completely lost its original texture. The rock was deposited in a shallow marine conditions which somewhat deeper shelf environment than the rocks of thin-section 1.

AGGREGATE FEATURES

Table 1. The particle size distribution of the aggregates of Bozlutepe Limestones.

Range of sieve diameter (mm)	Passing (gr)	Passing (%)	Passing cumulated (%)
25-14	542.84	7.15	100
14-10	782.38	10.30	92.85
10-7	710.273	9.35	82.55
7-4.75	464.42	6.12	73.2
4.75-1.7	2382.17	31.37	67.08
1.7-0	2710.80	35.71	35.71
	Total 7592.97	Total 100	

The granulometry values of approximately 7.5 kg sample collected from various places of the aggregate stock in the open-pit quarry of Bozlutepe Limestones are shown in Table 1.

From the Table 1, it can be revealed that the most of the grain of the aggregates are smaller than the 4.75 mm. Approximately 67 % of the grains are within the range 0 to 4.75 mm. The granulometry curve of the aggregates is shown in Figure 8. The curve is relatively flat when compared to ideal

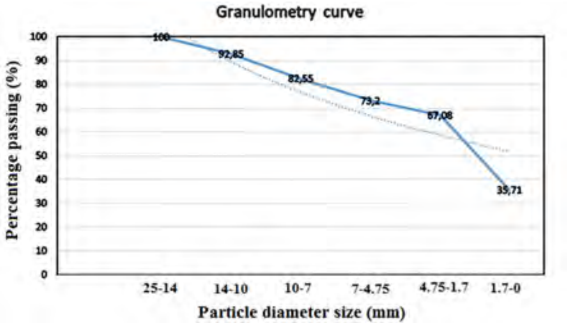

Figure 8. The granulometry curve of the aggregates of Bozlutepe Limestones.

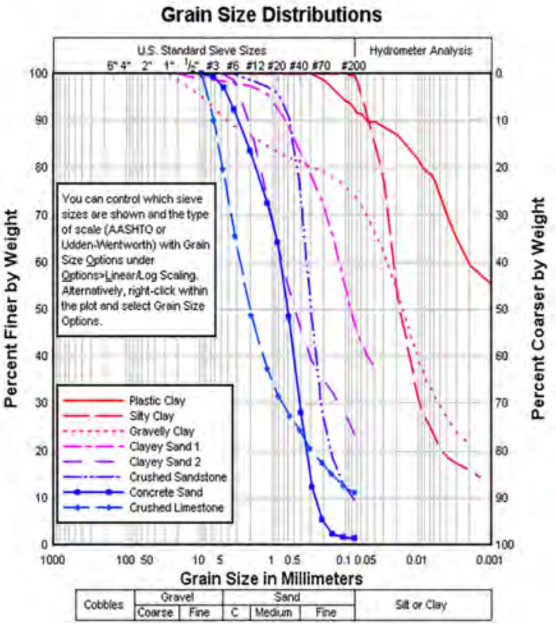

Figure 9. The U.S. standard sieve sizes and typical granulometry curves of various detrital [6].

granulometry curves of the aggregates used by cement industry. Despite these, there has been no negative feed-back from the local consumer of the aggregates.

The American classification of grain size related to granulometry curve of variety of detrital is shown in Figure 9. Our grain size distribution is in the range of crushed limestone area.

RESULTS AND RECOMMENDATIONS

The Bozlutepe Limestone Member is a unit belonging to Asmalitepe Formation and the rock is mainly represented by recrystallized limestones. The rock has mostly made of calcite and dolomite, and contains quartz mineral in places.

The metamorphism of the rock probably led to a widespread recrystallization, during which most of the primary textures disappeared. The limestones belonging to the member are very suitable to be evaluated as aggregate with abundant fractured, cracked and perfectly developed joint sets. The main disadvantages are that the reserves are very small (about 1 km2 area and 150-200 m thickness).

The aggregates produced from the Bozlutepe Limestone Member is generally fulfill the local consumer in spite of the differences of typical granulometry curve. For more proper interpretations, all the test should be done with more samples.

REFERENCES

1 Elçi E, Türk N, İşintek I. Limestone dimension stone quarry waste properties for concrete in Western Turkey. Arabian J. of Geosciences, 8 (10), (2015) 8951–8961.

2 Alhozaimy MA. Effect of absorption of limestone aggregates on strength and slump loss of concrete. Cement and Concrete Composites, 31 (7), (2009) 470–473.

3 Aquino C, Inoue M, Miura H, Mizuta M, Okamoto T. The effects of limestone aggregate on concrete properties. Construction and Building Materials 24(12) (2010) 233–236.

4 Chang ZT, Song XJ, Munn R, Marosszeky M. Using limestone aggregates and different cements for enhancing resistance of concrete to sulphuric attack. Cement and Concrete Research, 35, (2005) 1486–1494.

5 Zedef V. Selki–İmrenler–Çamlıca (Beyşehir) yöresinin jeolojisi, kil ve demir zuhurları. Selçuk Üniversitesi, Fen Bilimleri Enstitüsü Yüksek Lisans Tezi (Yayımlanmamış), (1987) 70s.

6 Google(https://www.google.com.tr/search?q=granulometry+curve&biw=1280&bih=870&source=lnms&tbm=isch&sa=X&ved=0ahUKEwjZ8_jFjIrQAhUBxRQKHZeTDC4Q_AUIBigB#imgrc=6pRBDzQ-BBmavM%3A), visited at 2.11.2016.

Hittite Journal of Science and Engineering, 2018, 5 (1) 63-68
ISSN NUMBER: 2148-4171
DOI: 10.17350/HJSE19030000066

Determination of Phase Transformation and Activation Energy in High Temperature Shape Memory Ti-V-Al Alloy

Semra Ergen
Gaziosmanpasa University, Department of Physics, Tokat, Turkey.

ABSTRACT

Ti-V-Al alloys are a good candidates for lightweight high temperature shape memory alloys. Due to their excellent mechanical properties with low density, in industrial applications, there are widely used as high temperature shape memory alloys. However, Ti-V-Al alloys have cold workability. Because of this feature, machinability in different forms is quite easy and cheap. In this work, microstructure and phase transformation of Ti-V-Al alloy produced by arc-melting method were investigated. The phase formations, microstructures, martensite-austenite transformation temperatures were characterized using XRD, SEM and DSC. Activation energies of the alloy were calculated by Kissinger and Osawa methods.

Article History:
Received: 2017/06/08
Accepted: 2017/09/10
Online: 2017/12/22

***Correspondence to**: Semra Ergen*
Gaziosmanpasa University, Faculty of Science and Arts, Department of Physics
Tokat, Turkey
Tel: +90 (356) 252-1616
Fax: +90 (356) 252 1585
E-Mail: semraergengop@gmail.com

Keywords:
High Temperature, Shape memory alloys, Phase transformations, Martensitic transformation, Activation energy

INTRODUCTION

High temperature shape memory alloys (HTSMA) with are potentially engineered to operate at temperatures above 100 ° C in the automotive, aerospace, and manufacturing industries. The HTSMA can be categorized into three groups depending on the transformation temperatures. First group; 100-400 ° C, the second group is 400-700 ° C and the third group is alloys having temperatures above 700 ° C [1].

There are many high temperature shape memory alloys in the literature. Some of these are Ni-Ti-X (X = Pt, Pd, Hf, Zr), Ni-Al, Cu-Al-Ni, Ni-Mn-Ga and Ti–Ta alloys [2-4]. These alloys have many problems that limit their practical application. The Ni-Ti-Pd / Pt alloy is quite expensive due to the Pd / Pt content. Ni-Ti-Hf / Zr alloys have poor cold workability [1]. Ni-Mn-Ga alloys are cracked at relatively high temperatures [5]. Ni-Al alloy is virtually no plastic at room temperature [1]. Cu-Al-Ni alloys have brittle phase deposits that cause poor ductility at grain boundaries of 1 mm size and large grains [6]. However, the density of all these high temperature shape memory alloys is still relatively high (6,4 -9 gr/cm^3). The high density of these alloys does not meet the demand for weight reduction in aerospace applications [7]. For this reason, it is necessary to produce and develop lighter high temperature shape memory alloys.

Ti-V-Al alloys are a good candidate for lightweight high temperature shape memory alloys. First, the densities of Ti-V-Al alloys are very low and close to the density of nearly pure titanium (4, 5 g / cm3). However, Ti-V-Al alloys have excellent cold workability, which can be reduced by more than 90% [8].

As mentioned above, Ti alloys used in many areas are preferred, especially in aircraft engines compared to other alloys in the aerospace industry due to their high temperature properties as well as their lightness, high strength (high specific strength) and heat resistance properties. Turbo fan motors used on aircrafts; Propeller, compressor, ignition chamber and tribune. Ti alloys are generally used in propeller and compressor sections located at the front of the engine where the air temperature is relatively low (400 ° C and lower). At the back of the aircraft, the tribune and combustion chamber parts use alloys with higher temperatures (700 ° C and higher). Ti alloys are also used in these parts of the aircraft, in the propeller and compressor sections, which are located in the front section of the engine where the temperature is relatively low (400 °C and lower). Alloys with higher temperatures (700 °C and higher) are used in the tribune and combustion chamber parts in the back half of the aircraft.

In the present study, Ti-15V-4Al alloy was produced by arc melting technique to be used in the front panels of aircraft engines in the aviation industry. Phase structures, microstructures and transformation temperatures of alloy were characterized with XRD, SEM and DSC techniques. Solid phase transformation properties of alloy were investigated by DSC technique at various heating/cooling rates. In the investigations made, it was observed how the phase transformation temperatures and the activation energy change with the heating/cooling rate and the number of thermal cycles. It has been generally determined that the phase transformation temperatures and the activation energy values reduce by the increase in the heating/cooling rate and their did not changed with the number of cycles. Thermal activation energy can be defined as the energy required during phase transformation of materials [9]. The calculation method of this energy was previously acquired by Kissinger and Ozawa [10,11]. The phase transformation temperatures are based on the fact that the material changes with the heating rate. At least four different heating and cooling rates were used in the calculation of the activation energy of the alloy. The energy values obtained by both Kissinger and Osawa methods were close to each other. It is seen that the activation energy values of alloy is much lower when compared to Ni-Ti. This means that activating the solid-solid transformation of the alloy is much easier than with the Ni-Ti alloy, which is an advantage for the Ti-V-Al alloy. In this manner, Ti-V-Al alloy which could be an alternative to the Ni-Ti alloy, was produced which was both lighter and more active.

EXPERIMENTAL

Ti–15V-4Al (wt %) alloy was prepared by vacuum arc melting in a water-cooled copper crucible under an Ar atmosphere using high purity Ti, V and Al. During the melting, zirconium was used as a getter material to reduce oxygen contamination of the prepared alloy buttons. The Ti-15V-4Al alloy was remelted many times for homogenization and was homogenized at 950 °C for 8 h in vacuum-sealed quartz tubes. And then was quenched in ice water by breaking the tubes. The transformation temperatures of the alloy were examined by differential scanning calorimetry. The differential scanning calorimetry measurements were carried out by a DSC 131 equipment (Seteram, France) at different heating/cooling rates in the temperature range 25–500°C. The surface of the TiVAl alloy etched with 10ml HF+ 20ml HNO_3 + 40ml H_2O solution for SEM analysis. The alloy was thermally cycled three times in the DSC to determine the stability of the transformation peaks. Activation energy of alloy has been determined by Kissinger and Osawa methods.

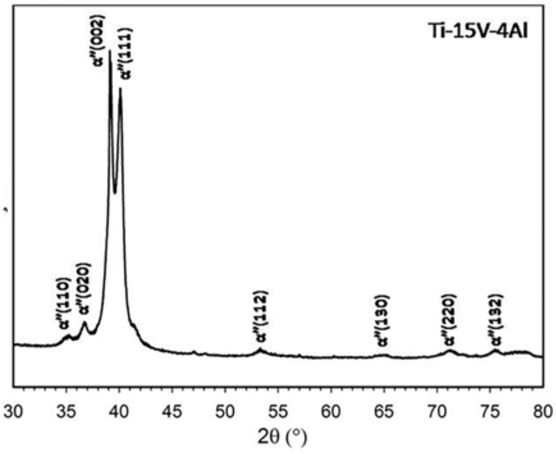

Figure 1. The X-ray diffraction pattern of Ti–15V-4Al alloy.

RESULTS AND DISCUSSION

Figure 1 shows the X-ray diffraction pattern of Ti–15V-4Al alloy at room temperature. It was understood that when the diffraction peaks were indicted, the alloy contained entirely orthorhombic α″ martensite phase. This indicates that the martensitic transformation temperature is above room temperature and the microstructure of the alloy is entirely composed of the α” martensite phase.

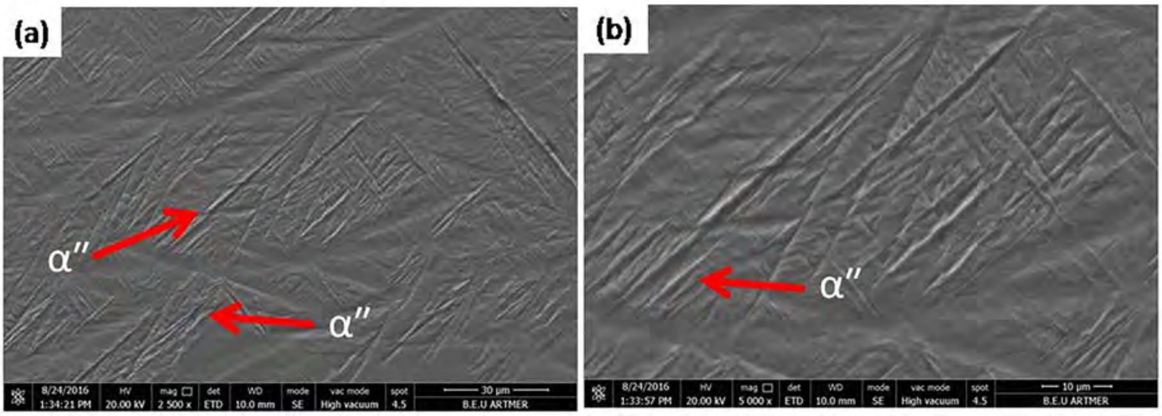

Figure 2. The SEM photographs of Ti-15V-4Al alloy.

Table 1. The starting and finishing temperatures (As, Af) of the reverse martensitic transformation, the enthalpy and activation energy values.

Heating Rate (°C/min)	*As (°C)*	*Af (°C)*	*ΔH_{MA} (kJ/mol)*	*$E_{Kissinger}$ (kJ/mol)*	*E_{Osawa} (kJ/mol)*
5	150	230	42	13.71	11.14
10	200	271			
15	210	297			
20	211	300			

Table 2. Reverse martensitic transformation temperatures under thermal cycling depending on heating-cooling rate.

Heating Rate (°C/dk)	*Cycle Number*	*As (°C)*	*Af (°C)*
10	1	209	298
	2	212	301
	3	218	308
20	1	211	312
	2	218	314
	3	219	318

Figure 2 shows the SEM photographs taken at 2500 and 5000 magnifications of the alloy. The microstructure of alloy consists entirely of α″ martensite phases. The martensite structures which are formed in a acicular shape are indicated by arrows in the Figure 2. As can be seen, SEM analyzes are consistent with XRD results.

Figure 3 shows the DSC curves recorded at four different heating cooling rates of Ti–15V-4Al alloy. The alloy exhibits a typical stepwise thermoelastic martensitic transformation (MT). In the DSC, the endothermic peak on the heating curves shows the reverse martensitic transformation from orthorhombic martensite to cubic austenite. The reverse martensitic transformation temperatures were measured by tangent method according to the DSC curves. An endothermic peak showing reverse martensitic transformation temperatures on the heating is clearly visible starting (As) temperature of 211 ° C and finish (Af) temperature of 300 ° C at heating and cooling rate of 20 °C/min. However, no significant exothermic peaks were detected on cooling. This phenomenon is similar to that of Ti-20Zr-10Nb [12], Ti-19Nb-9Zr [13] and Ti-30Ta [14] alloys, which can be attributed to the low enthalpy of transformation from β to α″ or the partial transformation from β phase to α″ martensite phase. This makes the martensite transformation peak too small to be detected by the DSC [12,15]. The starting and finishing temperatures (As, Ap, Af) of the reverse MT and the enthalpies depending on heating-cooling rate are summarized in Table 1.

In Fig. 3 (a-d), reverse martensitic transformation peaks are observed for heating cooling rates of 5, 10, 15 and 20 °C/min, respectively.

The transformation temperature graph versus heating rate is plotted in Figure 4. A small increase in transformation temperatures was observed as the heating rate increased. The reason for this increase is thought to be due to the internal friction in the microstructure [16].

In the Figure 5 (a,b), the DSC graphs belonging to the cycle analysises at heating and cooling rate of 10 °C/min and 20 °C/min are given for Ti-15V-4Al alloy.

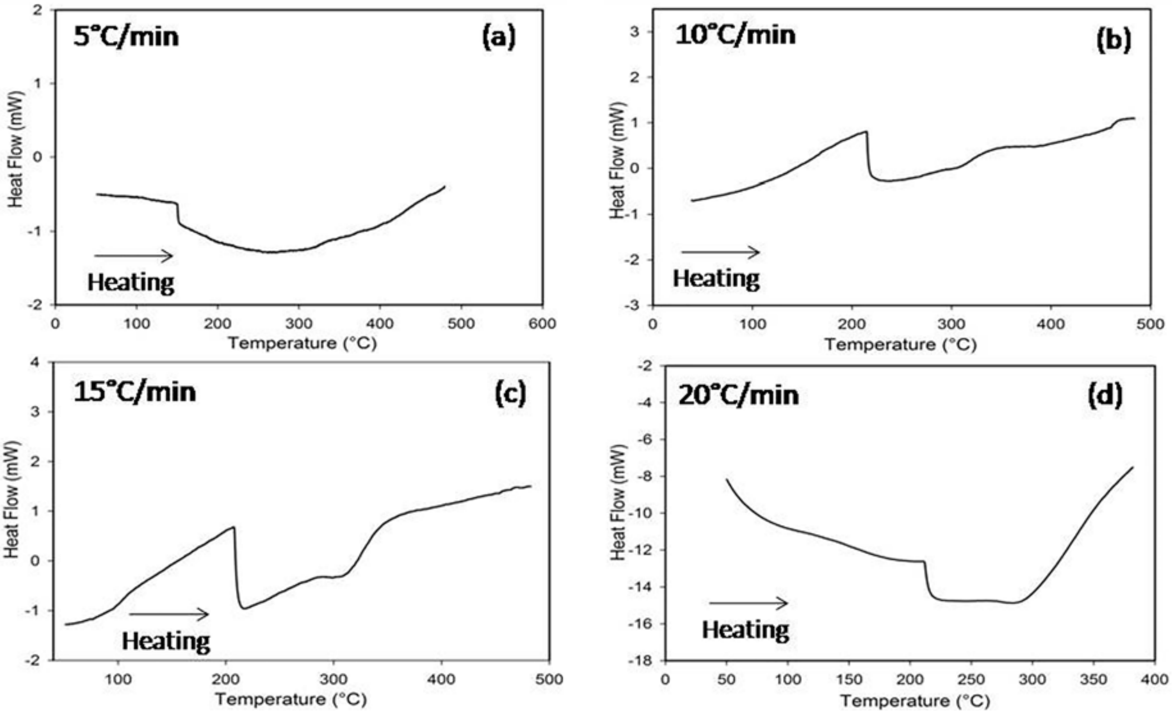

Figure 3. The DSC curves taken at four different heating-cooling rates of Ti–15V-4Al alloy. a) 5°C/min b) 10°C/min c) 15°C/min d) 20°C/min

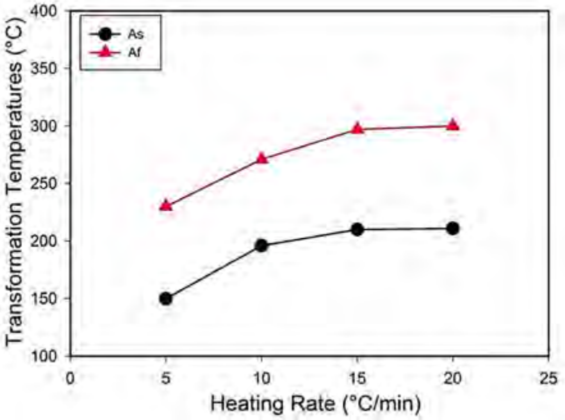

Fig 4. The transformation temperatures depending on heating-cooling rate of Ti-15V-4Al alloy.

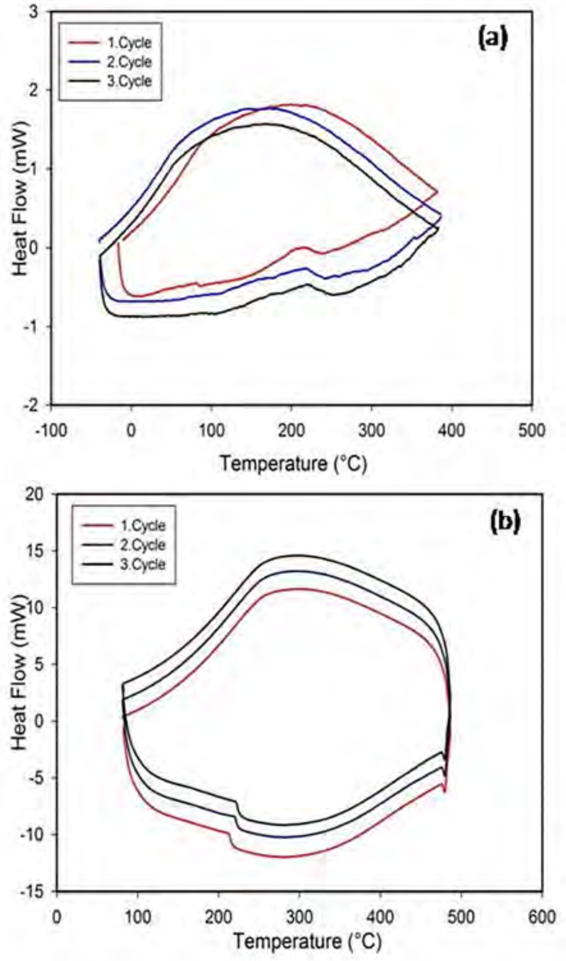

Fig 5. The thermal cycling analysises of Ti-15V-4Al alloy at heating-cooling rate a) 10 °C/min and b) 20°C/min

Figure 6 shows how the reverse martensitic transformation temperature changes with the number of cycles. No significant change in transformation temperatures was observed as the number of cycles increased at two different heating and cooling rates (Table 2). This means that the reverse martensitic transformation is stable. It is necessary to interpret it together with the TEM analysis in order to investigate both the number of cycles and the changes depending on the heating rate in more detail.

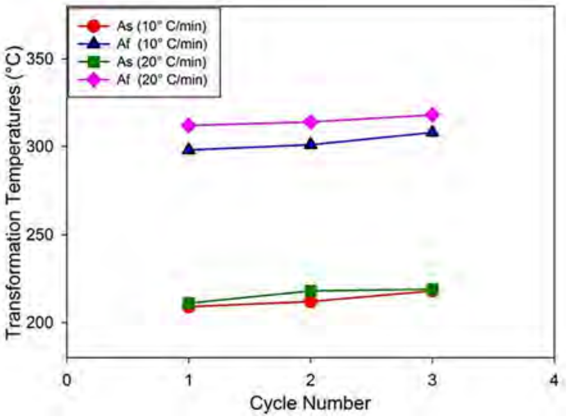

Fig 6. The reverse martensitic transformation temperatures depending on the number of cycles.

The energy that the material needs for phase transformation is called the activation energy. This energy can be found by making use of thermal cycling curves made with different heating rates [10-11]. Kissinger ve Osawa methods are available for estimating the kinetic parameters of materials from the DSC results. The kisssinger and Osawa methods for estimating the activation energy, E_A is derived from the following equation based on the maximum rate of phase transformation occuring at temperature T_m. According to the Kissinger method, the formula in equation 2 is used, and according to Osawa method, the formula in equation 3 is used in the calculation of activation energies.

$$\frac{d\alpha}{dT}=\frac{A}{\beta}\exp(\frac{E_A}{RT})(1-\alpha)^n \tag{1}$$

For Kissinger method, by plotting ln (versus , the slope of the plot equals - and subsequently the value of E_A can be obtained.

$$\frac{d(\ln\left(\frac{\beta}{T_m^2}\right)}{d\left(ln\frac{1000}{T_m}\right)}=\frac{E_A}{R} \tag{2}$$

As for Osawa method, by plotting ln (versus, with multiplying the slope of the plot equation by 2.19, the value of E_A can be obtained.

$$\frac{d(\ln(\beta)}{d\left(ln\frac{1000}{T_m}\right)}=2.19\times-\frac{E_A}{R} \tag{3}$$

In these equations, R is the general gas constant (R = 8,314 J / mol), E_A is the activation energy, β is the heating rate, and Tm is the temperature corresponding to the

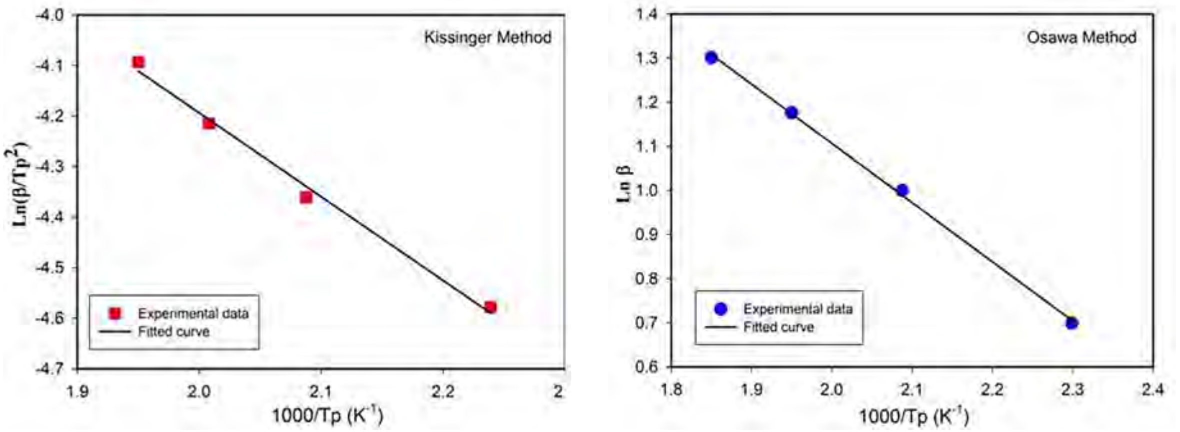

Fig 7. Determination of E_A for Ti-15V-4Al alloy using a) Kissinger and b) Osawa methods.

maximum peak during transformation in the DSC curve. The Kissinger and Osawa methods to estimate the kinetic parameters requires the DSC results obtained under at least three heating rates (Fig. 7).

The calculated activation energy values were 13.71 kJ / mol according to the kissinger method and 11.14 kJ / mol according to the Osawa method. The activation energies calculated by both methods are found to be close to each other (Table 1). It is seen that these values are much lower when compared to the activation energy value of the Ni-Ti alloy. This means that activating Ti-V-Al alloy is easier than Ni-Ti alloy [17].

CONCLUSIONS

In this study, phase transformation and microstructure of Ti-15V-4Al alloy were investigated by XRD and SEM analysis. Reverse transformation temperatures and phase transformation properties were examined by DSC technique as a function of heating-cooling rate and number of cycles. The results are summarized below.

1. The results show that the Ti-15V-4Al alloy is composed of a single orthorhombic α″-martensite phase at room temperature.
2. It was observed that the microstructure of the alloy contained martensite structures with a spindle-like shape.
3. The As and Af reverse martensitic transformation temperatures were approximately found to be 211 and 300 °C at heating-cooling rate of 20°C/min, respectively. No obvious exothermic peak was detected for Ti-15V-4Al alloy during cooling from 500 °C to room temperature.
4. From the DSC analyses, it was found that the increase in the heating rate caused a small increase in the reverse martensitic transformation temperatures.
5. No significant change in the reverse transformation temperatures of the alloy was observed as the number of cycles increased from the thermal cycling analyzes.
6. It was observed that the activation energy values calculated by both methods are close to each other and much lower than the energy values of the Ni-Ti alloy.

REFERENCES

1. Ma, J., Karaman, I., and Noebe, R.D. High temperature shape memory alloys. International Materials Reviews 55: 5 (2010) 257–315.
2. Atlı, K.C., Karaman, I., Noebe, R.D., Garg, A., Chulyakov, Y.I., Kireeva, I.V. Shape memory characteristics of $Ti_{49.5}Ni_{25}Pd_{25}Sc_{0.5}$ high–temperature shape memory alloy after severe plastic deformation. Acta Mater 59 (2011) 4747-4760.
3. Meng, X.L., Cai, W., Wang, L.M., Zheng, Y.F., Zhao, L.C., Zhou, L.M. Microstructure of stress–induced martensite in a Ti-Ni-Hf high temperature shape memory alloy. Scripta Mater 45 (2001) 1177-1182.
4. Zheng, X.H., Sui, J.H., Zhang, X., Yang, Z.Y., Wang, H.B., Tian, X.H., Cai, W. Thermal stability and high–temperature shape memory effect of Ti-Ta-Zr alloy. Scripta Mater 68 (2013) 1008-1011.
5. Ma, Y., Yang, S., Liu, Y., Liu, X. The ductility and shape–memory properties of Ni- Mn-Co-Ga high–temperature shape–memory alloys. Acta Mater 57 (2009) 3232-3241.
6. Kato, H., Stalmans, R., Van Humbeeck, J. Two–way shape memory effect induced by tension training in Cu–13.4Al–4.0Ni (mass%) alloy single crystals. Mater. Trans. 39 (1998) 378–386.
7. Yang, Z.Y., Zheng, X.H., Wu, Y., Cai, W. Martensitic transformation and shape memory behavior of Ti–V–Al–Fe lightweight shape memory alloys. Journal of Alloys and Compound, 680 (2016) 462–466.
8. Yang, Z.Y., Zheng, X.H., Cai, W. Martensitic transformation and shape memory effect of Ti-V-Al lightweight high–temperature shape memory alloys. Scripta Materialia 99 (2015) 97-100
9. Kok M., Yakıncı ZD., Aydogdu A., Aydogdu Y. Thermal and magnetic properties of Ni51Mn28.5Ga19.5B magnetic–shape–memory alloy. J Therm Anal Calorim 115 (2014)

555–559.

10. Kissinger, H. E. Reaction Kinetics in Differential Thermal Analysis. Analytical Chemistry. 29 No. 11, National Bureau of Standards, Washington, pp. 1702–1706, 1957.
11. Ozawa, T. A new method of analyzing thermogravimetric data. ***Chem. Soc. Jpn*** 38 (11) (1965) 1881–1886.
12. Cui, Y., Li Y., Luo K., Xu H. Microstructure and shape memory effect of Ti-20Zr-10Nb alloy. Mat. Sci. Eng. A. 527 (2010) 652–656.
13. Ma, L.W., Cheng, H.S., Chung, C.Y., Yuan, B. Effect of heat treatment time on microstructure and mechanical properties of Ti-19Nb-9Zr (at%) shape memory alloy. Materials Science & Engineering A 561 (2013) 427-433.
14. Zheng XH, **Sui JH,** Zhang X, Tian XH, Cai W. Effect of Y addition on the martensitic transformation and shape memory effect of Ti–Ta high–temperature shape memory alloy.**Journal of Alloys and Compounds** 539 (2012) 144–147.
15. Takahashi, E., Sakurai, T., Watanabe, S., Masahashi, N., Hanada, S. Effect of heat treatment and Sn content on superelasticity in biocompatible TiNbSn alloy. Mater. Trans. 43 (12) (2002) 2978-2983.
16. Acar E. Dynamic mechanical response of a Ni45.7Ti29.3Hf20Pd5 alloy. Materials Science and Engineering :A (2015) 633 169–175.
17. Fang, H., Wong, B., Bai, Y. Kinetic modeling of thermophysical properties of shape memory alloys during phase transformation. Construction and Building Materials 131 (2017) 146–155.

Hittite Journal of Science and Engineering, 2018, 5 (1) 69-73
ISSN NUMBER: 2148-4171
DOI: 10.17350/HJSE19030000067

The Synthesis and Spectral Properties of Benzofuran Derivative Bis-Chalcone

Neslihan Beyazıt
Mustafa Kemal University, Department of Chemistry, Faculty of Arts and Sciences, Hatay, Turkey

Article History:
Received: 2017/06/23
Accepted: 2017/08/21
Online: 2017/12/22

Correspondence to: Neslihan Beyazıt
Mustafa Kemal University, Department of Chemistry, Faculty of Arts and Sciences, Hatay, Turkey
Tel: +90 (531) 526-17 19
E-Mail: nbeyazit@mku.edu.tr

ABSTRACT

Khellin, a natural furanochromone, was isolated from the fruits of *Ammi visnaga* L. by using a rapid and easy technique. It was then hydrolyzed with 10% KOH to obtain khellinone. From the Claisen-Schmidt condensation of khellinone with terephthalaldehyde, a new benzofuran derivative bis-chalcone was synthesized and its spectroscopic properties were investigated in details.

Keywords:
Khellin, Khellinone, *Ammi visnaga* L., Claisen Schmidt condensation, Bis-chalcone

INTRODUCTION

Chalcones, a class of compounds naturally occuring in various plants, are precursors of flavonoids and they consist of two aromatic rings connected by an α,β-unsaturated carbonyl group (Figure 1). They can be obtained by the Claisen-Schmidt condensation reaction between acetophenone and benzaldehyde derivatives in the presence of acid or base catalysts [1].

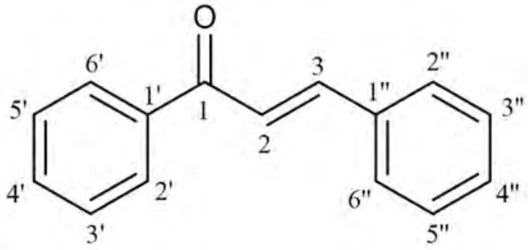

Figure 1. The general structure and numbering of chalcones.

Khellinone, the compound containing an acetophenone group, is a valuable starting material for the synthesis of new chalcone derivatives. It is essentially prepared via alkaline hydrolysis of khellin, a natural furanochromone isolated from Ammi visnaga L. (Scheme 1) [2]. In the literature, there are few studies on the synthesis of khellinone derivative chalcone compounds. Due to the presence of benzofuran moiety, they have a great potential for biological activities and pharmaceutical utilities [3-5].

Hitherto, many studies have been focused on synthetic and natural chalcone derivatives and their biological activities such as antibacterial, anticancer, antifungal, anti-inflammatory, antitubercular and antioxidant activity [6]. Also they have been extensively studied in optoelectronic fields due to their interesting photopysical and photochemical properties [7-10]. Recently, in situ generated copper (II) complexes of chalcone ligands have been found to catalyze the oxidation reaction of catechol to the corresponding o-quinone, a procedure known as catecholase activity [11].

In the present study, we report the isolation of khellin from Ammi visnaga L. growing in Hatay region and its basic hydrolysis to khellinone which is a benzofuran derivative and a starting material for the synthesis of chalcone. Then, a new bis-chalcone containing benzofuran moiety was synthesized from Claisen Schmidt condensation reaction of khellinone with terephthalaldehyde and its spectral properties was described in details.

MATERIALS AND METHODS

Terephthalaldehyde, Sodium hydroxide (NaOH) and the organic solvents were analytical grade and used without further purification. The plant material was harvested in September 2014 near Hatay region of Turkey and a voucher specimen have been deposited in the Herbarium of Biology Department, Mustafa Kemal University. The melting points were determined with a Thermo Scientific 9100 melting point apparatus and are not corrected. Elemental analyses were performed with a LECO CHNS-932 (USA) elemental analyzer. The electronic spectra were

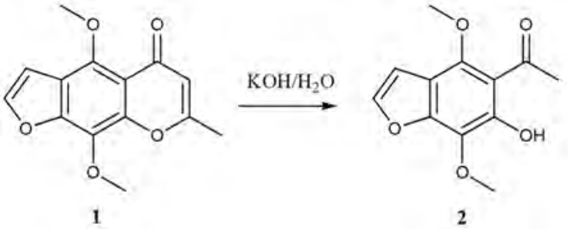

Scheme 1. Alkaline hydrolysis of khellin to khellinone.

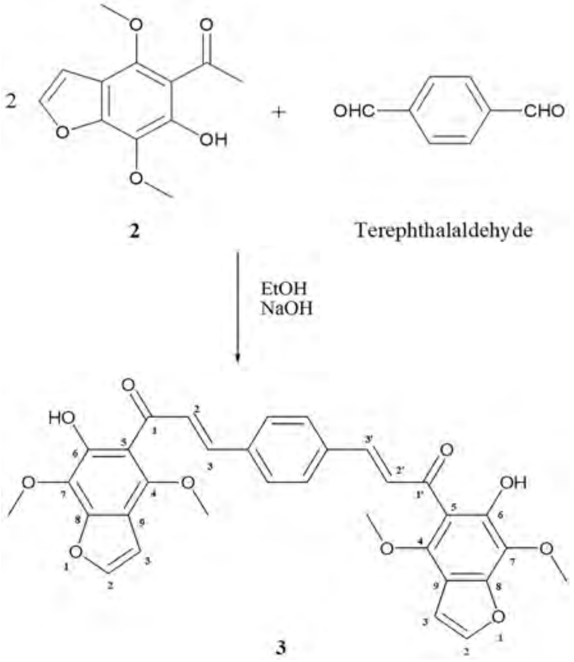

Scheme 2. The synthetic route of bis-chalcone.

measured on a OPTIZENα UV-Vis Spectrometer (South Korea). The mass spectra have been obtained by Agilent (USA) LC/MSD spectrometer using the ESI technique. The FT-IR spectra (4000-400 cm^{-1}) were recorded by Perkin Elmer (USA) Spectrum Two with U-ATR FTIR spectrometer. ^{1}HNMR (600 MHz) and ^{13}C NMR (600 MHz) spectra were recorded on a Bruker Advance III HD (USA) spectrometer using $CDCl_3$ and tetramethylsilane (TMS) was used as an internal reference. Thin-layer chromatography (TLC) was performed on Merck silicagel plates ($60F_{254}$), and visualized with ultraviolet light (366 and 254 nm).

Isolation of Khellin, 1

The ripe fruits (500 g) of *Ammi visnaga* L. were dried, grounded and extracted with 1 L hot water by a Soxhlet apparatus for 30h and the extract was concentrated by rotary evaporator to its half-volume. It was then extracted with 150 mL hexane many times, dried over Na_2SO_4 and concentrated to dryness under vacuum. The presence of khellin in the hexane residue was detected by thin layer chromatography. Khellin gave yellowish brown fluorescence under 254 nm UV light with R_f value 0.56 in solvent system EtOAc:$CHCl_3$ (60:40) [12]. The hexane residue was purified by column chromatography on silica gel G 60. The fraction eluted with dichloromethane-ethyl acetate (90:10) were concentrated and recrystallized from MeOH-water to obtain 0.9 g khellin. The structure of khellin (4,9-dimethoxy-7-methylfuro[3,2-g]chromen-5-one) was confirmed by comparing its melting point with the value reported as 154-155°C [13, 14].

Synthesis of Khellinone, 2

Khellinone (4,7-Dimethoxy-5-acetyl-6-hydroxybenzofuran) was prepared by alkaline hydrolysis of khellin according to the literature [2, 15]. 1.00 g of khellin (3.84 mmol) was dissolved in 15 mL of hot 10% KOH solution while the temperature was maintained at 70-80°C. At the end of the 2h reflux period, the reaction mixture was allowed to cool to room temperature and 3 mL of concentrated HCl was added dropwisely. The resulting precipitate was filtered off, recrystallized from hot MeOH and dried under vacuum to obtain 0.81 g (3.43 mmol) of khellinone with a yield of 89% (m.p. 99-100°C) [2, 15].

Synthesis of Bis-Chalcone, 3

Khellinone (4.23 mmol) was dissolved with terephthalaldehyde (2.15 mmol) in 30 mL of ethanol. The solution was treated with 5 mL of 50% sodium hydroxide solution and left overnight. The reaction mixture was neutralized with dilute acetic acid (10%) and the separated product was collected, washed with water and recrystallized from hot MeOH.

3.(2E,2'E)-3,3'-(1,4-phenylene)bis[1-(6-hydroxy-4,7-dimethoxybenzofuran-5-yl)]prop-2-en-1-one. Dark yellow powder, yield: 0.77g, 63%. m.p.: 229-230°C. Molecular formula $C_{32}H_{26}O_{10}$. Elemental Analysis Calc. (%): C = 67.36; H = 4.59. Found. (%): C = 67.03; H = 4.77. Selected IR data (ν, cm^{-1}) 3137 (Ar-H), 2940 (C-H), 2835 (C-H), 1621 (C=O), 1551 (C=C). UV-Vis: λ_{max} (nm) (Ethanol): 270, 362. ^{1}H NMR (600 MHz; $CDCl_3$): δ, ppm 12.68 (s, 2H, 2xAr-OH), 7.94 (d, 2H, *J*=15.6 Hz, 2xC=CH), 7.85 (d, 2H, *J*=15.6 Hz, 2xCO=CH), 7.70 (s, 4H, Ar-H), 7.54 (d, 2H, *J*=2.3 Hz, 2xfuran-H), 6.90 (d, 2H, *J*=2.3Hz, 2xfuran-H), 4.10 (s, 6H, $2xOCH_3$), 4.07 (s, 6H, $2xOCH_3$). ^{13}C NMR (150 MHz; $CDCl_3$): δ, ppm 194.52 (C), 153.27 (C), 152.07 (C), 150.77 (C), 144.30 (CH), 142.19(CH), 137.13 (C), 129.07 (CH), 129.00 (CH), 128.84 (CH), 128.08 (CH), 112.76 (C), 111.87 (C), 105.25 (CH), 62.03 (OCH_3), 61.08 (OCH_3). MS (+API-ES): *m/z* 571.0 $[M+H]^+$.

RESULTS and DISCUSSION

In the present work, khellin **(1)** was isolated from the ripe fruits of *A. visnaga* L. and it was then hydrolyzed by using 10% KOH to form khellinone **(2)** which is a benzofuran derivative containing acetophenone group. The structure of khellin and khellinone was confirmed by comparing

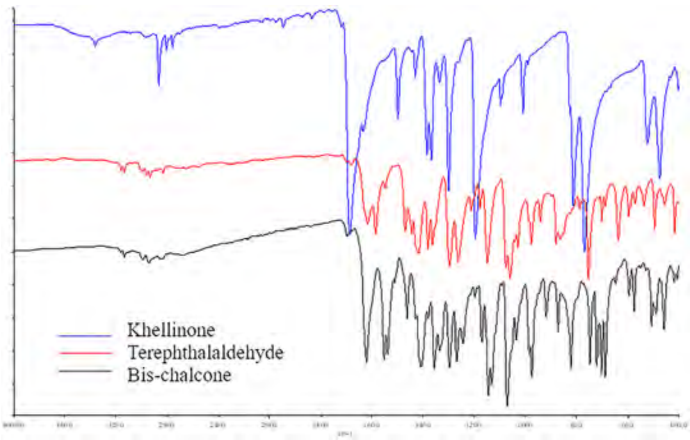

Figure 2. FT-IR spectra of khellinone, terephthalaldehyde and bis-chalcone (**3**).

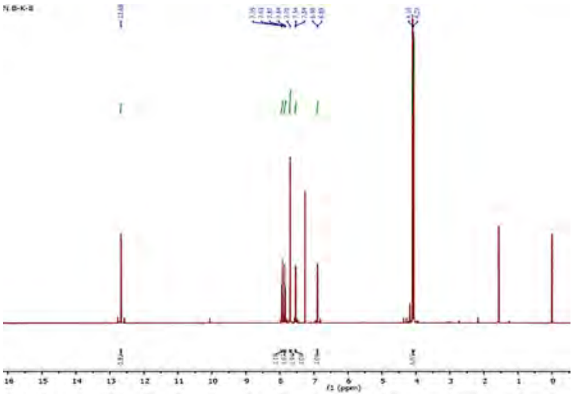

Figure 3. ^{1}H NMR spectrum of **3** in $CDCl_3$.

their melting points obtained experimentally with those found in the literatüre [13-15]. From the reaction of khellinone with terephthalaldehyde in the presence of NaOH, a new bis-chalcone **(3)** was obtained and the synthetic route to the compounds is outlined in Scheme 1 and Scheme 2.

The purification of bis-chalcone (**3**) was carried out by column chromatography. The crude product loaded on the chromatography column was first eluted with CH_2Cl_2 in order to remove the possible side products and unreacted starting materials, and then eluted with CH_2Cl_2/acetone (1:1) to collect bis-chalcone. The chemical structure of purified product was characterized by spectroscopic data (FT-IR, ^{1}H-NMR, ^{13}C-NMR, UV-Vis and mass) and elemental analyses. The elemental analyses and the physical measurement results confirmed the proposed structure of title molecule. The mass spectrum of **3** was recorded in $CHCl_3$ solution (Figure S1, in the supplementary file). In the spectrum, the molecular ion peak observed at m/z 571.0 which is attributed to $[M+H]^+$, provided the evidence for the formation of the suggested structure.

The ATR-FTIR spectrum (Figure 2) of **3** revealed a band at 1621 cm^{-1} indicating the presence of carbonyl (C=O) group. The band at 1551 cm^{-1} was assigned to the C=C group that is characteristic of the α,β-unsaturated carbonyl compounds. The IR frequency values of carbonyl and olefinic groups are lower than typical values (ca. 1700 cm^{-1} and 1650 cm^{-1}, respectively) because of the conjugation effect of C=C-C=O moiety. Also the presence of electron donor groups at *ortho*- positions of benzofuran rings shifted the IR frequencies of C=O and C=C bands to a lower values [16]. Moreover, the spectrum shows several weak bands in the region of 2835-3137 cm^{-1} corresponding to aliphatic and aromatic C-H stretching vibration frequencies.

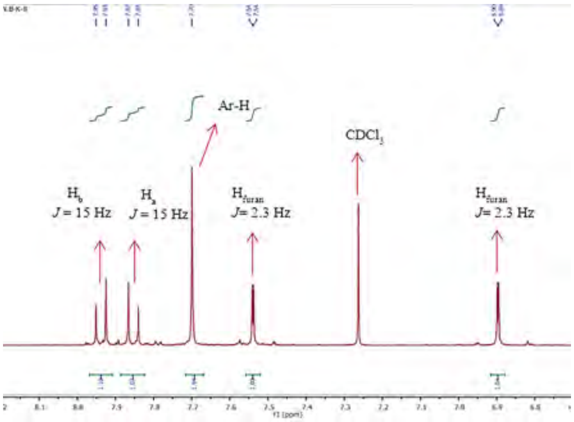

Figure 4. ^{1}H NMR spectrum of **3** (zoom in to 6.7-8.2 ppm range).

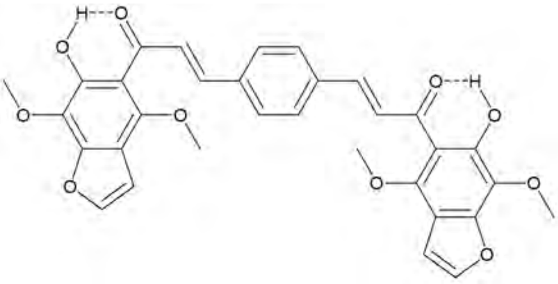

Scheme 3. Intramolecular hydrogen bonding at bis-chalcone.

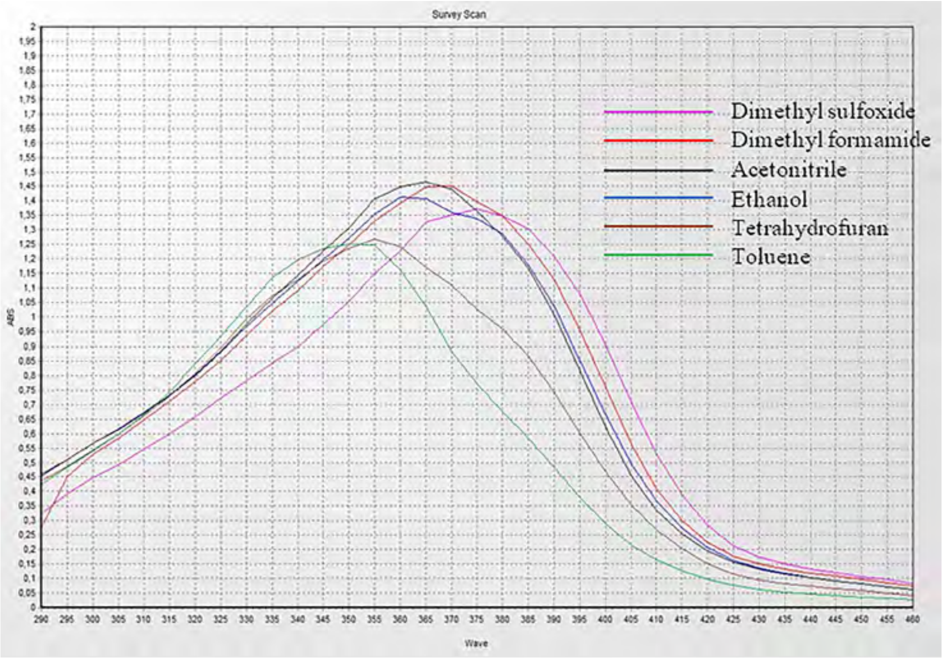

Figure 5. Electronic absorption spectra of **3** in six different solvents.

^{1}H NMR spectrum of **3** measured in $CDCl_3$ (Figure 3) exhibits two doublets at 7.94 ppm (*J*=15.6) and 7.85 ppm (*J*= 15.6), indicating the trans configuration of vinylic system due to the large coupling constant (*J*) values (Figure 4) [17]. The ethylenic protons adjacent to the carbonyl group (H_α) showed chemical shift at higher field (7.85 ppm) than those of H_β (7.94 ppm) which are more deshielded by carbonyl group due to the conjugation of the carbonyl group and double band [18]. The singlet signal observed at 12.68 ppm was attributed to phenolic protons of benzofuran moieties. The two vicinal protons in the furan ring were appeared as two doublets at 7.54 ppm (*J* = 2.3 Hz), and 6.90 ppm (*J* = 2.3 Hz) (Figure 4).

The structure of 3 was also supported by 13C APT NMR spectrum (Figure S2, in the supplementary file). The number of signals in the spectrum was consistent with the non-equivalent carbon atoms in the molecule. The carbonyl carbon atoms of the α,β-unsaturated ketone groups gave rise to a characteristic signal at 194.52 ppm. The negative signals at 61.08 and 62.03 ppm confirmed the presence of methoxy carbons in the benzofuran rings. The positive signals appeared between 150.77 and 153.27 ppm in the APT spectrum of 3, are likely to be ascribed to the quaternary carbons adjacent to the oxygen atoms. Signals due to aromatic ring, α, and β-carbon atoms were appeared in the range of 128.09-144.30 ppm. Relatively high chemical shift values for phenolic protons and carbonyl carbons (12.68 and 194.52 ppm, respectively) might be due to the formation of intramolecular hydrogen bonding between the carbonyl oxygens with phenolic hydroxyl protons (Scheme 3) [16].

The electronic spectra of chalcones have been extensively studied by a large number of researh groups. It was reported that UV spectrum of chalcones generally consists of two essential absorption bands: one usually appears at 340-390 nm referred to as band I and relatively a minor absorption band at 220-270 nm known as band II [19]. The characteristic band I of chalcones may be attributed to n-π* transitions of the whole molecule.

The electronic absorption spectra of bis-chalcone (3) were recorded in the region 300-500 nm (Figure 5), using freshly prepared 10-6 M solutions in six different solvents (toluene, tetrahydrofuran, ethanol, acetonitrile, dimethyl formamide and dimethyl sulfoxide) with increasing polarities from apolar to polar. The maximum absorption values of 3 were found to be in the range of 350-375 nm and upon increasing the polarity of solvents, noticeable batochromic shifts were observed in the UV spectra. The results obtained in the present study were consistent with the literature. Kumari et al. reported that the solvatochromic effect on absorption spectra of chalcone derivatives showed appreciable red shifts from apolar to polar solvents because of the intramolecular charge transfer (ICT) interactions. They suggested that the strong interaction between singlet excited state of chalcone molecules with polar solvents caused batochromic shifts in the electronic spectra due to large charge distribution between ground and singlet excited state of title molecules (20).

CONCLUSION

In the present study, it was reported the synthesis and spectral characterization of a new benzofuran derivative bis-chalcone obtained from the condensation reaction of terephthalaldehyde with khellinone which is the hydrolysis product of khellin. The spectral analyses revealed that the resonance-stabilized intramolecular hydrogen bonding in the bis-chalcone noticeably affects the spectroscopic properties of the compound, causes a considerable downfield shift of hydroxyl proton and carbonyl carbon signals in the NMR spectrum and also a shift to lower frequencies for carbonyl and vinyl group in the FT-IR spectrum. The effect of various solvents over electronic spectra of the title molecule was also studied and it was observed the long-wavelength absorption band undergoes a red (batochromic) shift with increasing solvent polarity which means excited state molecule is better stabilized by solvation than the molecule in the ground-state.

REFERENCES

1. Xue Y, LiuY, An L, Zhang, L, Yuan Y, Mou, J, Liu L, Zheng Y. Electronic structures and spectra of quinoline chalcones: DFT and TDDFT–PCM investigation. Computational and Theoretical Chemistry 965 (2011) 146-153. https://doi.org/10.1016/j.comptc.2011.01.042.
2. Gammill RB. The Synthesis and Chemistry of Functionalized Furochromones. 2. The Synthesis, Sommelet–Hauser Rearrangement, and Conversion of 4,9–Dimethoxy–7–[(methylthio)methyl]–5H–furo[3,2–g][1]benzopyran–5–one to Ammiol. Journal of Organic Chemistry 49 (1984) 5035–5041. DOI: 10.1021/jo00200a002.
3. Osman SA, Yosef HAA, Hafez TS, El–Sawy AA, Mousa HA, Hassan AS. Synthesis and Antibacterial Activity of Some Novel Chalcones, Pyrazoline and 3– Cyanopyridine Derivatives Based on Khellinone as well as Ni(II), Co(II) and Zn(II) Complexes. Australian Journal of Basic and Applied Sciences. 6 (2012) 852–863.
4. Baell JB, Gable RW, Harvey AJ, Toovey N, Herzog T, Hansel W, Wulff H. Khellinone Derivatives as Blockers of the Voltage–Gated Potassium Channel Kv1.3: Synthesis and Immunosuppressive Activity. Journal of Medicinal Chemistry 47 (2004) 2326–2336. DOI: 10.1021/jm030523s.
5. Ahmed Farag IS, Abd El–Hafez OM, Rybakov VB. Crystal Structure of a New Chalcone Compound Prepared from Khellinone. Crystal Research and Technology 25 (1990) 1399–1404. DOI: 10.1002/crat.2170251209.
6. Singh P, Anand A, Kumar V. Recent developments in biological activities of chalcones: A mini review. European Journal of Medicinal Chemistry 85 (2014) 758–777. https://doi.org/10.1016/j.ejmech.2014.08.033.
7. Shettigar S, Chandrasekharan K, Umesh G, Sarojini BK. Studies on nonlinear optical parameters of bis–chalcone derivatives doped polymer. Polymer 47 (2006) 3565–3567. https://doi.org/10.1016/j.polymer.2006.03.062.
8. Prabhu SR, Jayarama A, Chandrasekharan K, Upadhyaya V, Ng SW. Synthesis, growth, structural characterization, Hirshfeld analysis and nonlinear optical studies of a methyl substituted chalcone. Journal of Molecular Structure Volume 1136 (2017) 244-252. https://doi.org/10.1016/j.molstruc.2017.01.069
9. Arshad MN , Al–Dies AM, Asiri AM, Khalid M, Birinji AS, Al–Amry KA, Braga AAC. Synthesis, crystal structures, spectroscopic and nonlinear optical properties of chalcone derivatives: A combined experimental and theoretical study. Journal of Molecular Structure Volume 1141 (2017) 142-156. https://doi.org/10.1016/j.molstruc.2017.03.090.
10. Muhammad S, Al–Sehemi AG, Su Z, Xu H, Irfan A, Chaudhry AR. First principles study for the key electronic, optical and nonlinear optical properties of novel donor–acceptor chalcones. Journal of Molecular Graphics and Modelling. 72 (2017) 58–69. https://doi.org/10.1016/j.jmgm.2016.12.009.
11. Thabti S, Djedouani A, Rahmouni S, Touzani R, Bendaas A, Mousser H, Mousser A. Synthesis, X–ray crystal structures and catecholase activity investigation of new chalcone ligands. Journal of Molecular Structure 1102 (2015) 295–301. DOI: 10.1016/j.molstruc.2015.08.071.
12. Beltagy AM, Beltagy DM. Chemical composition of Ammi visnaga L. and New Cytotoxic Activity of its Constituents Khellin and Visnagin. Journal of Pharmaceutical Sciences and Research 7 (2015) 285–291.
13. Günaydın K, Beyazit N. The Chemical Investigations on the Ripe Fruits of Ammi visnaga (Lam.) Lamarck Growing in Turkey. Natural Product Research 18 (2004) 169–175. http://dx.doi.org/10.1080/14786410310001608091.
14. Anrep GV, Barsoum GS, Kenawy MR. The Pharmacological Actions of the Crystalline Principles of Ammi visnaga Linn. Journal of Pharmacy and Pharmacology 1 (1949) 164–176. DOI: 10.1111/j.2042–7158.1949.tb12395.x.
15. Schöberg A, Sina A. Khellin and Allied Compounds. Journal of American Chemical Society 72 (1950) 1611–1616. DOI: 10.1021/ja01160a051.
16. Tay MG, Tiong MH, Chia YY, Kuan SHC, Liu ZQ. A Way to Improve Luminescent Efficiency of Bis–Chalcone Derivatives. Journal of Chemistry 2016 (2016) 1–8. http://dx.doi.org/10.1155/2016/3608137.
17. Aksöz BE, Ertan R. Spectral Properties of Chalcones II. FABAD Journal of Pharmaceutical Sciences 37 (2012) 205–216.
18. Thirunarayanan G, Gopalakrishnan M, Vanangamudi G. IR and NMR spectral studies of 4–bromo–1–naphthyl chalcones–assessment of substituent effects. Spectrochimica Acta Part A: Molecular and Biomolecular Spectroscopy. 67 (2007) 1106–1112. DOI: 10.1016/j.saa.2006.09.034.
19. Mabry TJ, Markham KR, Thomas MB. The Ultraviolet Spectra of Chalcones and Aurones, in: The Systematic Identification of Flavonoids, Springer–Verlag, Berlin–Heidelberg–New York, pp. 227–250, 1970.
20. Kumari R, Varghese A, George L, Sudhakar YN. Effect of solvent polarity on the photophysical properties of chalcone derivatives. RSC Advances 7 (2017) 24204–24214. DOI: 10.1039/c7ra01705g.

Hittite Journal of Science and Engineering, 2018, 5 (1) 75-83
ISSN NUMBER: 2148-4171
DOI: 10.17350/HJSE19030000068

The Effect of Welding Positions on the Weldability of X20CrMoV11-1 Steels

Bünyamin Çiçek[1] **Emine Gündoğdu İş**[2] **Emre Gümüş**[2] **Polat Topuz**[2]
[1] Hitit University, Alaca Avni Celik Vocational School, Corum, TURKEY.
[2] Istanbul Gedik University, Gedik Vocational School, Istanbul, TURKEY.

Article History:
Received: 2017/07/24
Accepted: 2017/08/21
Online: 2017/12/28

***Correspondence to**: Bünyamin Çiçek,*
Hitit University, Alaca Avni Celik Vocational School, Corum, Turkey
Tel: +90 (364) 411-5050/4515
Fax: +90 (364) 411-5353
E-Mail: bunyamincicek@hitit.edu.tr

ABSTRACT

In the study, mechanical properties of martensitic steel X20CrMoV11-1 was investigated after being welded using Tungsten Inert Gas (GTAW) welding method at different weld positions (PC and PJ-EN 6947). The X20CrMoV11-1 steels have been widely used in thermal power plant applications in combustion chambers and other high-temperature parts. These materials experience extremely high internal pressure at the service conditions. WCrMoV12 Si was used as the filler metal in the welding. The GTAW welding process was conducted in a controlled manner and all the parameters used during the process was monitored. The post welding heat treatment was applied in order to eliminate the variations in the hardness of the welded materials. The samples were characterized using tensile, bending, hardness, and notch impact tests. Macro photographs were taken from the samples to observe the transition areas. The results indicated that the mechanical properties obtained from the samples welded in PC position were higher than those obtained from PJ position.

Keywords:
Weld; Welding positions; Mechanical tests; Heat input.

INTRODUCTION

Steels with martensitic microstructure (low carbon) and high creep resistance can be used at high temperatures for a long period of time. One of the potential applications of these materials is thermal and nuclear power plants. Over the years, the demand on the service temperature level in these plants have increased. As a result, studies on the development of new steel-based materials with enhanced creep and corrosion resistance have soared. The graph shown in Fig. 1 shows the need for service temperatures and pressures depending on years. Steels with 9-12% Cr content have been started to be used in these applications since 1950s. These steels can be used at the pressures of about 350 bar and temperatures of 600°C. In our work, X20CrMoV11-1 (short name X20) steel was used from these steels. [1, 2]

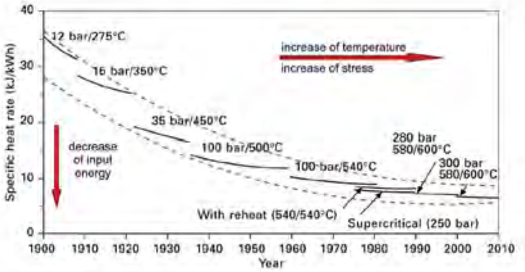

Figure 1. Heat rate of steam power plants in Germany as a function of steam parameters[1]

The X20 steel, developed in 1950, containing 12% Cr, was modified in 1970s by micro-alloying with tungsten. This phase enhances the corrosion and oxidation resistance. The main use of these steels in the world was limited primarily to turbine blades. However, in Europe these modified steels have been used in steam pipelines for energy production especially in Germany. The weldability of this X20 steel was low due to the high carbon content (especially due to the high content of carbon-about 0.2%). The high carbon content results in to hydrogen fracture. On the other hand, these deficiencies were minimized by the heat treatment of the weld zone. This post-weld heat treatment (PWHT) is made to dissipate the irregular hardness distribution in the weld zone [2-5].

In the world, the X20 steel was used in the construction of the indispensable elements in the energy sector. In the application stage, the acceptability of welding related to the rapid cooling (cooling time and rate) of the weld zone was found to be in different positions [6-10]. In our study, we aimed to unravel the effect of different welding positions on the mechanical and microstructural properties of X20 steel. We tried to shed light on the welding science in the X20 steels depending on various welding configuration.

MATERIALS AND METHOD

In this study, pipes made of X20 steel with the dimensions of Ø38x5 mm were used. According to production reports; the X20 material was exposed to hydrostatic testing at the pressure of 70 bar for 5 sec. Then, a 20 minute normalization heat treatment conducted at 1090°C and tempering heat treatment at 780°C were applied to the samples. The chemical composition of the steel samples determined using spectral analysis method

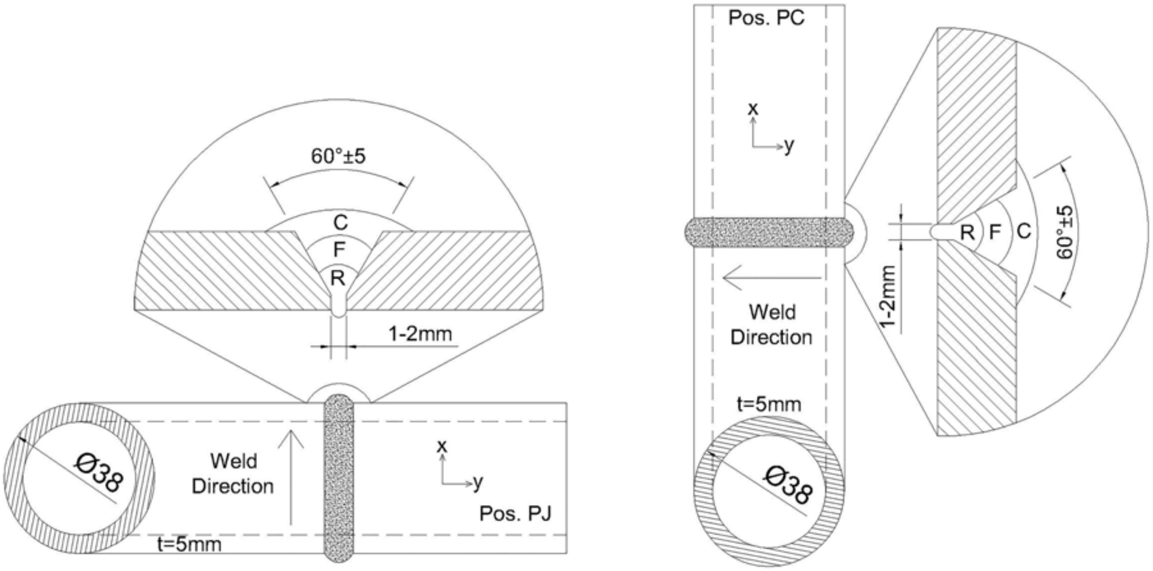

Figure. 2. Welding positions PJ-PC and welding groove details

Table 1. Comparison of chemical composition of 11-12% Cr steels according to to steel makers [2] and Chemical composition of tested X20 steel grade. (Based on the manufacturer's data).

Type	*Chemical Element (%)*															*Ceq**
	C	*Si*	*Mn*	*Nb*	*Co*	*Cr*	*Mo*	*Ni*	*Cu*	*V*	*W*	*B*	*N*	*Ta*	*Nd*	
X20	*0,2*	*0,4*	*0,6*	-	-	*11*	*1*	*0,5*	-	*0,25*	-	-	-	-	-	*1,37*
HCM12A (T/P122)	*0,11*	*0,1*	*0,6*	*0,05*	-	*12*	*0,4*	-	*1*	*0,2*	*2*	*0,003*	*0,03*	-	-	*1,46*
NF12	*0,08*	*0,2*	*0,5*	*0,07*	*2,5*	*11*	*0,2*	-	-	*0,2*	*2,6*	*0,004*	*0,05*	-	-	*1,28*
SAVE12	*0,1*	*0,3*	*0,2*	*0,07*	*3*	*11*	-	-	-	*0,2*	*3*	-	*0,04*	*0,07*	*0,04*	*1,25*
VM12-SHC	*0,12*	*0,5*	*0,3*	*0,055*	*1,6*	*11,5*	*0,3*	*0,25*	-	*0,25*	*1,5*	*0,0045*	*0,05*	-	-	*1,36*
X20 (Tested)	*0,17*	*0,26*	*0,47*	-	-	*10,39*	*0,94*	*0,38*	-	*0,27*	-	-	-	-	-	*1,35*

*C_{eq} *calculated by K. Winterton Formula for pre-heat temp.[13]*

Table 2. Filler Metal Chemical Analysis (EN 21952) (according to the manufacturer's data).

Element	*C %*	*Si %*	*Mn %*	*P %*	*S %*	*Cr %*	*Ni %*	*W %*	*V %*	*Mo %*
min.	*0,170*	*0,200*	*0,400*	-	-	*10,500*	-	*0,350*	*0,200*	*0,800*
max.	*0,240*	*0,600*	*1,000*	*0,025*	*0,020*	*12,000*	*0,800*	*0,800*	*0,400*	*1,200*
W20	*0,199*	*0,46*	*0,6*	*0,015*	*0,001*	*11,03*	*0,34*	*0,4*	*0,31*	*1,01*

Table 3. During of Welding use to Parameters

Pass Code	*Current (A) Avg.*	*Voltage (V) Avg.*	*Current Type (Filler Metal Polarity)*	*Weld Speed mm/min. Avg.*	*Heat Input KJ/mm. Avg.*
Root (R)	*75*	*10*	*DC (-)*	*52*	*0,87*
Filler (F)	*105*	*11*	*DC (-)*	*55*	*1,26*
Cap (C)	*115*	*12*	*DC (-)*	*57*	*1,45*

(product data). TIG welding method was used in different welding positions of PC and PJ and the corresponding configurations are shown in Fig. 2. In the same figure, weld groove and pass numbers (R-Root, F-Filler, and C-Cap) are also indicated. The welding processes were carried out by EN 9606-1 certified welders and by taking the considering carbon equivalent (C_{eq}) value into account, the specimens were preheated to 250 °C before the welding [11] (EN 12952-5). As shown in Fig. 2, the welding of the metals were conducted in 3 passes and the inter-pass temperature was measured to be 350-400 °C. WCrMoWV12Si (named as W20 throughout the manuscript) was used as filler material. The chemical composition of the filler material is shown in Table 2(acc. to product data). In the table, the composition of a standard filler material is also given to compare the composition of the applied filler with the standards. The welding parameters used in the work is listed in Table 3. The heat input was calculated based on Equation 1 using the values shown in Table 3 [12].

$$H = \frac{60 \text{ x E x A}}{1000 \text{ x S}} \qquad (1)$$

where; **H**=heat input(kJ/mm), **E**=arc volt(volts), **A**=current(amp), **S**=weld speed (mm/min)

Heat input is a relative measure of the energy transferred per unit length of the weld. It has a significant effect on the characteristics of the weld metal since it affects preheat and inter-pass temperature. In addition, as a function of heat input, the cooling and heating rate of the metal chances, which in turn results in obtaining different mechanical properties and the metallurgical structures in the weld metal and the HAZ [12]. The welded samples were finally exposed to a post-weld heat treatment (PWHT) based on EN 12952-5 (Table 4). The cycle graphic after the PWHT operation is presented in Fig. 3a and schematic drawn it is given Fig. 3b. The cooling and the heating rates were calculated using the slopes of the graph. The calculated heating and cooling rate values were found to be compatible with the standards values as shown in Table 4 and, PWHT (Post Weld Heat Treatment) parameters for all position specimens.

After the welding process, all the samples were characterized using non-destructive tests (NDT) including

Table 4. PWHT parameters.

Material Group Code (acc. to EN 15608)	*Material First Temp. (°C)*	*Heating Rate (°C/h)*	*Max. Temp. (°C)*	*Holding Time (min.)*	*Cooling Rate (°C/h)*	*Device* Closed Temp. (°C)*
min.	-	-	*730*	*30*	-	-
max.	-	*150*	*770*	-	*400*	-
Group No: 6	*25*	*150*	*750*	*30*	*150*	*175*

** Device= PWHT Heater device (Weldotherm STE 82-6)*

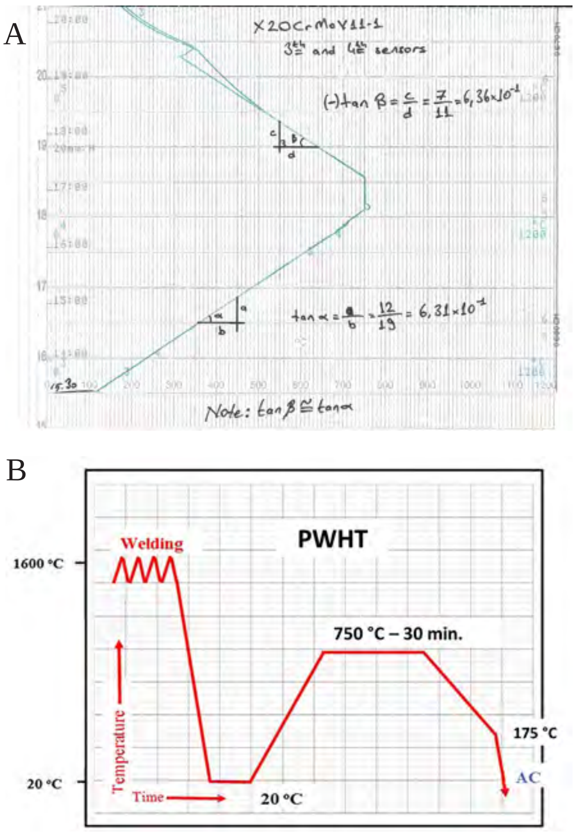

Figure. 3. PWHT graphs for both positions; (a) device, (b) schematic.

visual (VT), penetrant (PT), and radiography (RT) tests. All the mentioned tests were conducted according to the requirements of quality level B in EN 5817. The samples which passed the NDT tests were then subjected to further mechanical testing. The mechanical tests used in the work and their corresponding standards are given below.

1. Tensile Test (made of acc. to EN 4136)
2. Bending Test (made of acc. to EN 5173)
3. Impact Test (made of acc. to EN 9016)
4. Hardness Test (made of acc. to EN 9015-1)
5. Macrostructure Analysis (made of acc. to EN 17639)

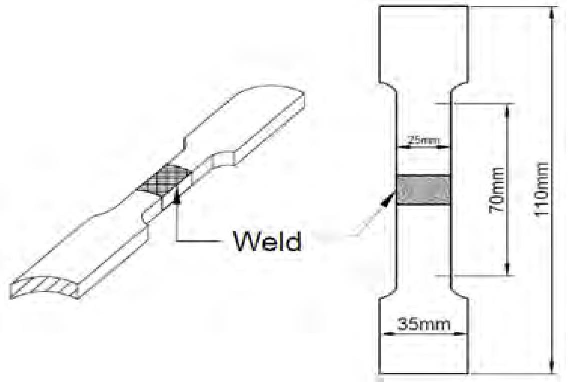

Figure. 4. Tensile test specimen acc. to relevant the standard

Tensile Test

The sample configuration used in the tensile testing is shown in detail in Fig. 4 and used Instron 5989 tensile module. The tests were carried out at room temperature.

Bending Test

The bending test parameters and the applied test method are shown in Fig. 5. Specimens were prepared for two welding positions (PC and PJ), separately for both root and face as required by relevant standard (Fig. 5). The bending values and test parameters were calculated according to the equations given below. The 3-point bending test was conducted using an Instron 5989 Bend Module.

$$A_{min} = D + (2 * t) + 3 \tag{2}$$

$$A_{max} = D + 3t \tag{3}$$

$$B = \frac{100 * t}{E} - t \tag{4}$$

$$C = t + (0.1 * D) \tag{5}$$

Where; **A**: Distance rollers, **B**: Bend roller diameter, **C**: Specimen width, **t**: Thickness, **D**: Pipe diameter

Impact Test

The sample configuration used for impact testing is

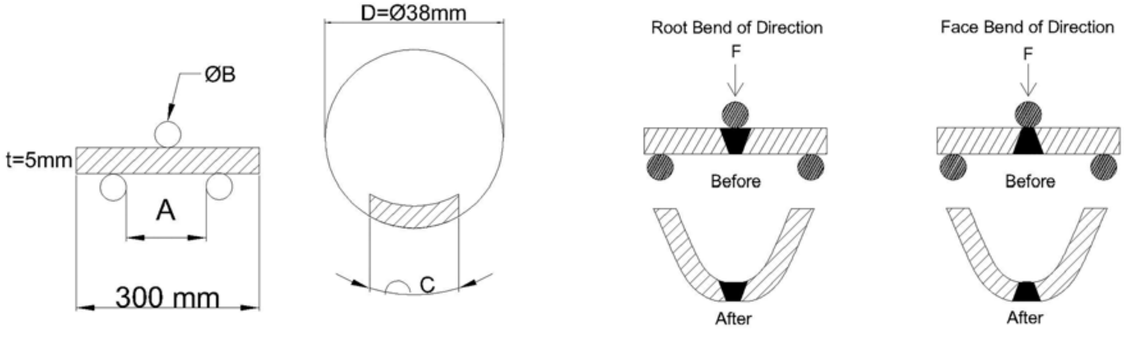

Figure. 5. Bending test parameters according to relevant the standard

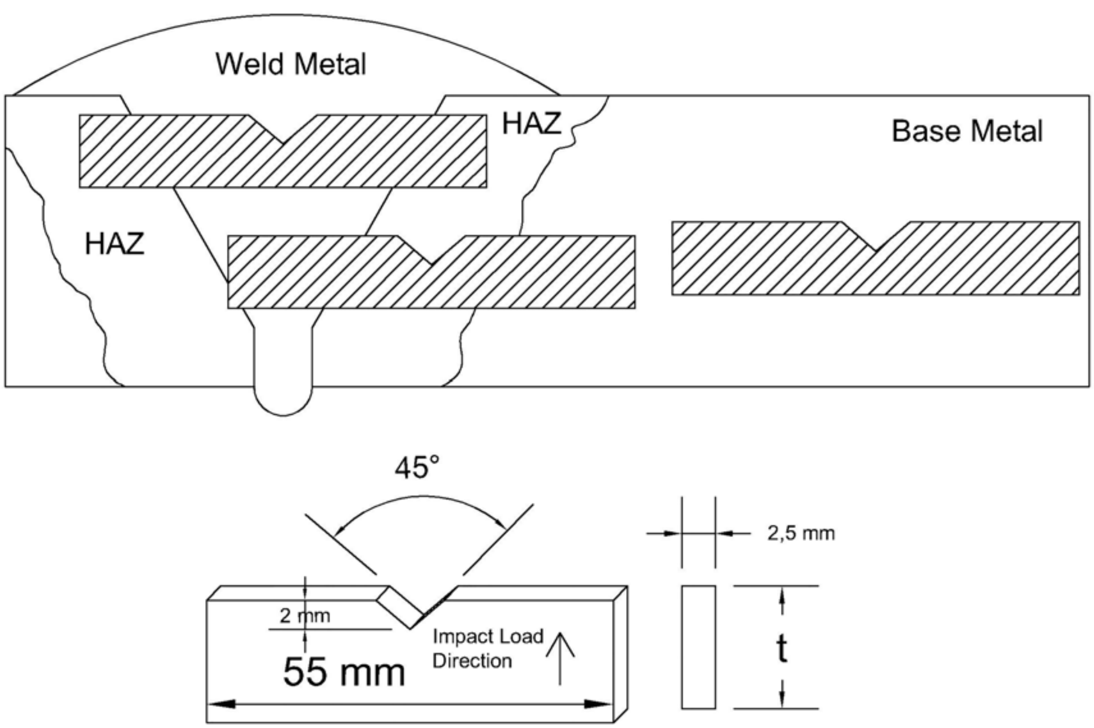

Figure. 6. Dimensions of impact test specimens and notch locations acc. to the standard

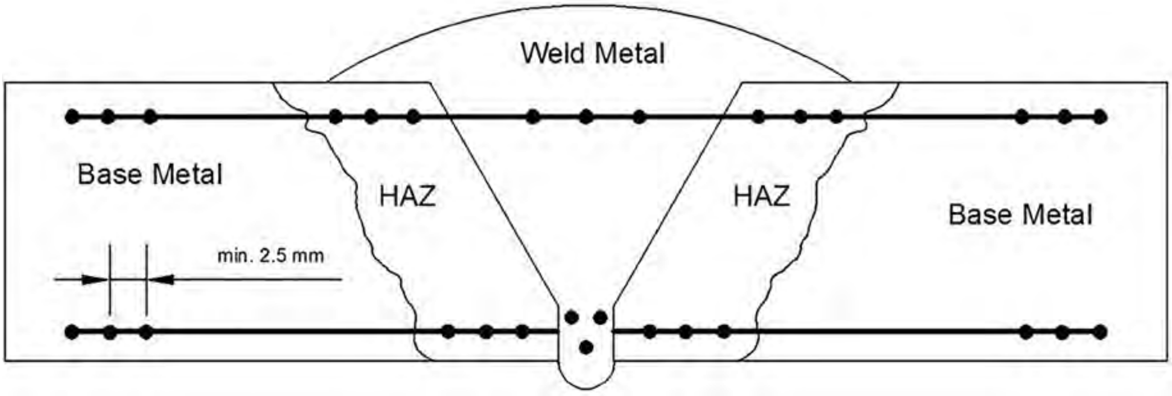

Figure. 7. Measurement locations for hardness test

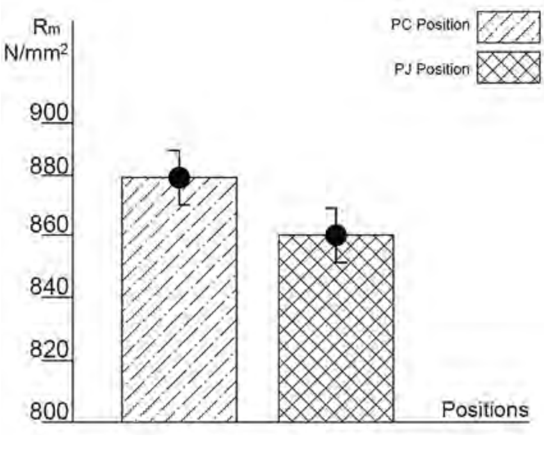

Figure 8. Tensile strength values

shown in Fig. 6. The tests were carried out at room temperature. These specimens were examined with an Instron 450MPX. For each welding positions, 3 specimens were prepared from the base material, HAZ, and weld metal.

Hardness Test

The hardness tests were conducted at the root line and cap line (Fig. 7) using 10 kg of load used to Vickers (HV10). These specimens were examined with a Qness Q10M. 3 independent measurements were recorded at the root and cap line.

Macrostructure Analysis

Specimens were cut from the vertical section of welded

Table 5. Tensile Test Results

Specimen Code	Test Temp. (ºC) (+)	Max. Load (kN)	Rp 0,2 (N/mm^2)	Rm (N/mm^2)	Elongation (%)
PC 1	20	103	657	882	16,3
PC 2	20	104	685	876	16,9
PJ 1	20	99	630	861	17,1
PJ 2	20	96	633	857	16,2

plates in order to investigate the welding zone. The samples were made of metallographic process and etched with a Nital10 solution (%10 HNO3 + %90 Alcohol) [14, 15].

RESULTS AND DISCUSSION

It is known that the weld quality requires control of weld pool width and cooling time. The cooling time $t_{8/5}$ (from 800 °C to 500 °C) is related to the hardness of the weld metal [16]. The microstructure of the weld metal is highly dependent upon speed of the heating and cooling cycles and based on these parameters various microstructural features are formed in the weld metal. Therefore, one of the most important factors affecting the microstructure and thus strength of the weld metal is the cooling time which is the function of the heat input [16]. The weld regions of carbon steels mainly consists of a microstructure containing allotriomorphic ferrite grains (primary ferrite or grain boundary ferrite – α_a), acicular ferrite (AF), and Widmanstatten ferrite (ferrite with aligned second phase – α_W) phases [17-20].

Tensile Test

The tensile test results showed that all the specimens got broken in the HAZ area. Tensile strength (Rm) of the samples which were welded in PC position was higher than those obtained from welded samples in PJ position. The results revealed that the highest tensile strength (879 N/mm^2) was obtained from the sample welded in PC position. The tensile strength of the sample welded in PJ position, however, was found to be 859 N/mm^2 (Fig. 8). The all of results in the test is listed in Table 5. Despite the difference between the tensile strength values, elongation of the samples were close to each other. In addition, as expected from EN10216-2: A1 standards, the elongation should began in range of 14-17% which is fully compatible with the test results.

It was reported that while the welding position of a metal did not have any significant effect on tensile and hardness values, the toughness of the weld metal showed a dependency on the welding position [21]. It was observed that the toughness value of the weld metal obtained from the vertical position was lower than that of obtained from the flat position at all temperatures. In the same paper it was also shown that the hardness values obtained regardless of the welding positions were close to each other, indicating a good agreement with the tensile test results [21]. Those findings suggest that the total heat input values can be different in each material during the welding process. The difference in the total heat input value varying based on the welding position leads to different cooling rate and time, which in turn results in the formation of different grain structure and microstructure [16]. The difference in the cooling rates, as well as the dwell time at high temperatures causes significant microstructural changes [22]. Briefly; the difference in the mechanical properties of the weld metal is attributed to the difference in the cooling time (t8/5) resulted from the amount of heat input.

Bending Test

The bending test parameters and results are shown in Table 6. Images taken random from the bended samples are given in Fig. 9 for both root and face bending. It is noteworthy that after both bending modes, no crack formation was observed in welding and HAZ regions. After the bending tests, no visual damage was observed after 180° folding. Furthermore, liquid penetration test detected no invisible surface cracks. The PC and PJ

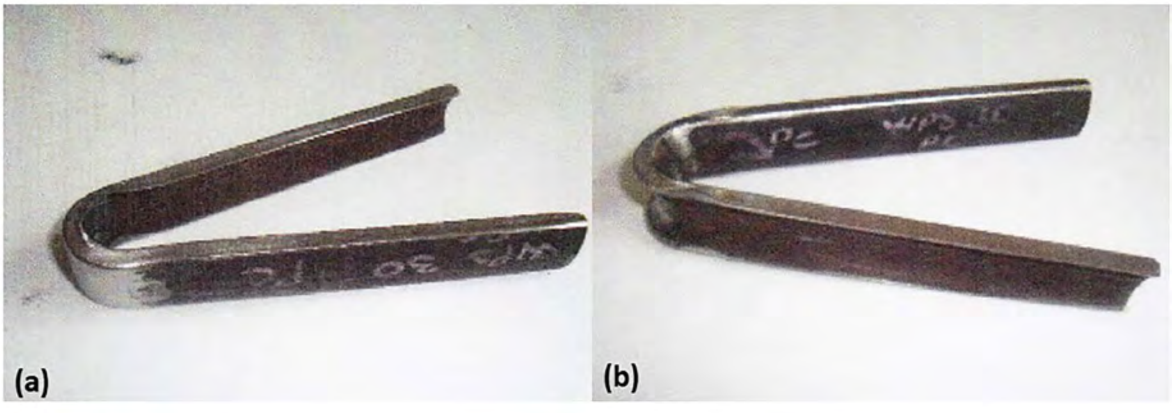

Figure. 9. Bending test sample type photos; (a) Face bend, (b) Root bend

Table6. Bending Test Results

Test Specimen Code	Test Direction*	Rollers Distance (A) (mm)		Roller Diameter (B) (≈mm)	Specimen Width (C) (≈mm)	Last Bending Angle	Crack Result*
		min	max				
PC	F	51	52	24	9	180°	UN
PC	R	51	52	24	9	180°	UN
PJ	F	51	52	24	9	180°	UN
PJ	R	51	52	24	9	180°	UN

* F = Face Bend, R = Root Bend, UN = Unobserved

positions no damage was reported neither in weld metal nor in HAZ. In a study conducted by Figueirôa et al. [6] showed that weld region with a lower shape factor and more penetration were observed. In addition, when the same test but in the overhead position was applied to the same material the authors obtained weld regions with a low shape factor [6]. Our results (shown in Fig. 7) indicated a low shape factor and thus no deformation, which is in a good agreement with the results shown by Figueirôa et al. [6].

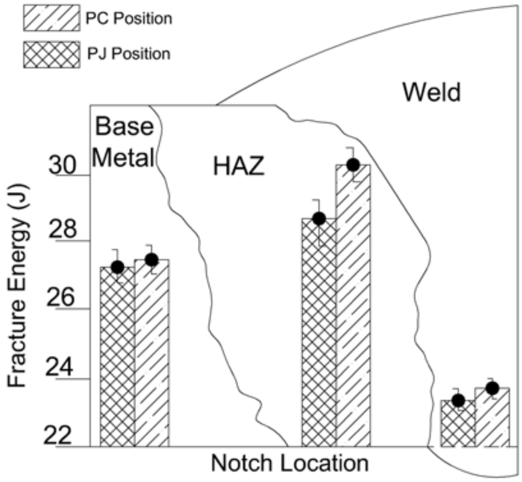

Figure. 10. Fracture energy difference of zones

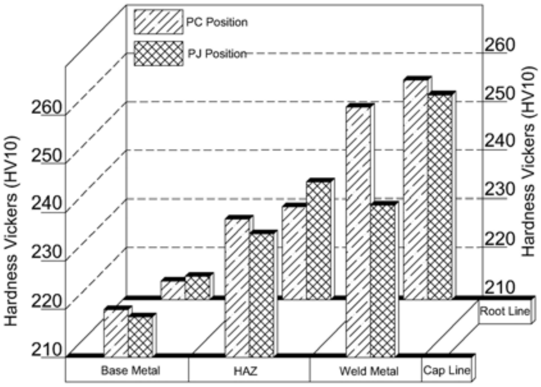

Figure. 11. Hardness test results

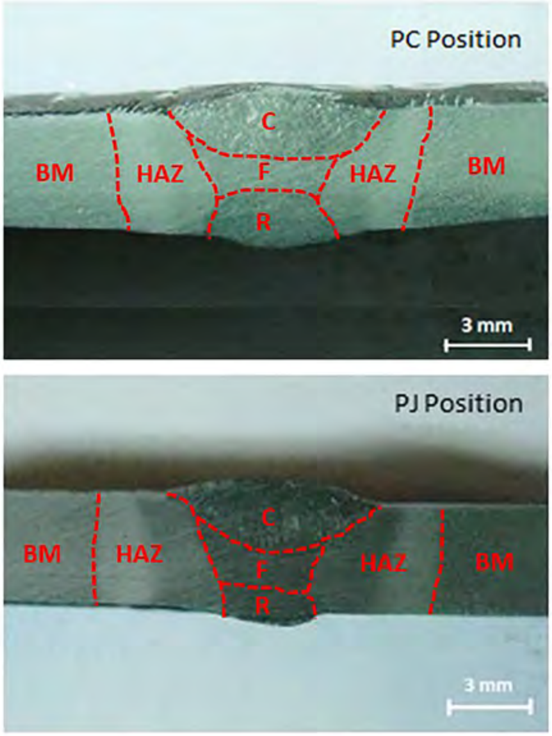

Figure. 12. Macrostructure images

Impact Test

Impact test results are shown in Fig. 10. For the specimens welded in PC position, the fracture energy values of 27, 31, and 23 J were obtained from the base, HAZ, and weld metal, respectively. For the samples welded in PJ position, the measured fracture energy values were 27, 29, and 23 J in base, HAZ, and weld metal, respectively.

When the Charpy test results are taken into account, it can be stated that welding position had no effect on the fracture energy. The toughness of the HAZ area, however, was higher than the toughness values obtained from both weld and base metals. Gomes et al. [22] explained the increment in the toughness in the HAZ area by the repeated welding process in the HAZ region. The repeated welding process results in a recrystallization of the HAZ region in every welding pass, which in turn leads to higher toughness [22].

Hardness Test

The results are given in Fig. 11. It is expected that hardness of the weld metal should be higher than the base metal and HAZ, which was confirmed by this study. For every welding positions, the base metal hardness values were 211±9 HV min. and 220±5 HV max. as shown in Figure 11. Hardness values of HAZ were 211±9 HV min. and 238±7 HV max. On the other hand, measurements on weld metal were found to be 244±5 HV min. and 264±6 max.

The hardness test results indicated that for both welding modes, the hardness of the base metal was different than those obtained from weld metal. In addition, the welding process resulted in an increase in the hardness. This can be explained by cooling time and fine grain structure of the weld metal. Heat input that transferred into the material during the welding process caused hardening in HAZ and weld metal. Hardness values measured from the base metal and HAZ were close to each other. However, hardness of the weld metal measured in the cap line were higher for PC and lower for PJ. The values in the root of the weld metal were about the same level. For PC position, this can be explained by the effect of the total heat input on grains. When the cooling is faster because of the lower total heat input, the structure will be harder. Finally, looking at all the values, the maximum 350 HV (HV10) limit in EN12952-6 standard was not exceeded [23-25]. The highest hardness values were measured in the HAZ and weld metal, and can be attributed to the process of quenching and tempering by the subsequent passes. This hardening only occurs in steels in which a small fraction of martensitic microstructure is formed and when they possess elements that promote secondary hardening [26-28].

Macrostructure Analysis

The images of the welding zone shown in Fig. 12 recorded by a Strues-Welding Expert. The images were taken using the standard of EN 17639.

Macro images (BM: Base Metal) of the side surfaces were examined for both welding modes at different positions. Root (R), filler (F), and cap (C) formations were observed from the images. HAZ also occurred because of the heat input. HAZ showed equal distribution on both sides of welding depending on the heat input for both positions. No defect or discontinuities were detected from the weld metal to HAZ transition area. Similarity; a study, macro photographs taken and HAZ borders were examined. But because the preheat value varies in this study, the HAZ limits are different and the other areas (base metal and weld metal) are clearly monitored [22]. In our work, the HAZ limits are close to each other because the preheat value is constant.

CONCLUSION

In our work, the effect of welding position on the mechanical properties of weld metals (X20CrMoV11-1 steels (X20)) were evaluated. The obtained results are given below:

1. Similar tensile test results were obtained regardless of the welding position, which is consistent with the literature.
2. It was observed that the bending behavior of the weld metal was not affected by the welding position. No deformation was observed in the weld zone for both positions.
3. The impact test results indicated that the toughness values obtained from the HAZ region were higher than the toughness values measured from the welding zone and base metals. In addition, the toughness of the weld zone was low due to the high hardness of the region. The toughness of the base metal was similar with the data obtained during the fabrication process of the metal.
4. The Vickers test results confirmed the impact test results and were in a good agreement with the literature.
5. Macro photographs taken from the weld zone showed all the elements of the welding zone and there was no difference based on the welding position.

REFERENCES

1. Bazazi, A.A., Evolution of Microstructure during Long-term Creep of a Tempered Martensite Ferritic Steel. 2009: Cuvillier.
2. Urzynicok, M., K. Kwieciński, and M. Szubryt, Experience in the welding of martensitic steel VM12-SHC. Welding International, 2013. 27(4): p. 249-254.
3. Qian, Y. and J. Zhao, Influences of local PWHT from different criteria at home and abroad on the residual stress of the under-matching welded joint. International Journal of Pressure Vessels and Piping, 2017. 154: p. 11-16.
4. Khalaj, G., Pouraliakbar, H., Jandaghi M.R., Gholami A. Microalloyed steel welds by HF-ERW technique: Novel PWHT cycles, microstructure evolution and mechanical properties enhancement. International Journal of Pressure Vessels and Piping, 2017(152): p. 15-26.
5. Loots, R., Susceptibility of service exposed creep resistant materials to reheat cracking during repair welding, University of Pretoria, 2003.
6. Figueirôa, D.W., Pigozzo, I.O., Gonçalves e Silva, R.H., Abreu Santos T.F., Filho S.L.U. Influence of welding position and parameters in orbital tig welding applied to low-carbon steel pipes. Welding International, 2017. 31(8): p. 583-590.
7. Muzaka, K., Park, M., Lee, J.P., Jin, B., Lee B.R., Soo Kim, W.Y. A Study on Prediction of Welding Quality Using Mahalanobis Distance Method by Optimizing Welding Current for A Vertical-position Welding. Procedia Engineering, 2017. 174: p. 60-67.
8. Yan, Z., Xu, D., Li, Y. A visual servoing system for the torch

alignment to initial welding position. Intelligent Robotics and Applications, 2008: p. 697-706.

9. Bermejo, M.V., Karlsson L., Svensson, L.E., Hurtig, K., Rasmuson, H., Frodigh, M., Bengtsson, P., Effect of welding position on properties of duplex and super duplex stainless steel circumferential welds. Welding in the World, 2015. 59(5): p. 693-703.
10. Pasternak, J., S. Fudali, Własności oraz doświadczenia w spawaniu stali przeznaczonych na elementy ciśnieniowe kotłów o parametrach nadkrytycznych. XVI Międzynarodowa Konferencja Spawanie w Energetyce, Opole-Jarnołtówek, 2008.
11. Yurioka, N., T. Kasuya, A chart method to determine necessary preheat in steel welding. Welding in the World/Le Soudage dans le Monde, 1995. 5(35): p. 327-334.
12. Funderburk, R.S., A look at input. Welding Innovation, 1999. 16(1).
13. Rao, T.R., Metal casting: Principles and practice, New Age International, 2007.
14. Kurgan, N., Sun, Y., Cicek, B., Ahlatci, H., Production of 316L stainless steel implant materials by powder metallurgy and investigation of their wear properties. Chinese science bulletin, 2012. 57(15): p. 1873-1878.
15. Vander Voort, G.F., Etching isothermally treated steels. Heat Treating Progress, 2001. 1(2): p. 25-32.
16. Jin, B., M. Soeda, K. Oshima, Control of weldpool width and cooling time in TIG welding using a neural network model. Welding international, 1996. 10(8): p. 614-621.
17. Grong, O., D.K. Matlock, Microstructural development in mild and low-alloy steel weld metals. International Metals Reviews, 1986. 31(1): p. 27-48.
18. SA, D., Inclusion formation and microstructure evolution in low alloy steel welds. ISIJ international, 2002. 42(12): p. 1344-1353.
19. Hu, F., P. Hodgson, K. Wu, Acceleration of the super bainite transformation through a coarse austenite grain size. Materials letters, 2014. 122: p. 240-243.
20. Santos,T.F., Torres, Edwar A. Vilela, José M. C. Andrade, Margareth S. Cota, André B., Caracterização Microestrutural De Aços Baixo Carbono Por Microscopia De Força Atômica (Microstructural Characterization Of Low Carbon Steels By Atomic Force Microscopy). Revista Latinoamericana de Metalurgia y Materiales, 2014: p. 118-133.
21. Masoumi, F., D. Shahriari, Effects of welding positions on mechanical properties and microstructure in weld metal of high strength steel, Advances in Materials and Processing Technologies 83(2009) p. 1121-1127.
22. Gomes Moojen, R., Machado, I.G., Mazzaferro J.A.E., Gonzalez, A.R., Cooling rate effects in the welding of API 5L-X80 steel. Welding International, 2017. 31(2): p. 100-110.
23. Kasuya, T., N. Yurioka, M. Okumura, Methods for predicting maximum hardness of heat-affected zone and selecting necessary preheat temperature for steel welding. Nippon Steel Technical Report, 1995: p. 7-14.
24. Graville, B., Weld Cooling Rates and Heat-Affected Zone Hardness in a C Steel. Welding Journal, 1973. 52(9): p. 377-385.
25. Abd El-Rahman Abd El-Salam, M., I. El-Mahallawi, M. El-Koussy, Influence of heat input and post-weld heat treatment on boiler steel P91 (9Cr–1Mo–V–Nb) weld joints Part 1–Microstructure. International Heat Treatment and Surface Engineering, 2013. 7(1): p. 23-31.
26. Kim, C.M., J.B. Lee, J.Y. Yoo. A study on the metallurgical and mechanical characteristics of the weld joint of X80 Steel. The Fifteenth International Offshore and Polar Engineering Conference. , 19-24 June, Seoul, Korea, p. 158-162, 2005.
27. Zhu, Z., Structure property correlation in the weld HAZ of high strength line pipe steels, University Of Wollongong Thesis Collection, 2013.
28. Nicholas, J., Abson. The prediction of maximum HAZ hardness in various regions of multiple pass welds, 17th International Conference Computer Technology in Welding and Engineering, University of Cranfield, 18-19 June, 2008.

NATIONAL & INTERNATIONAL SCIENTIFIC EVENTS

ASME 2018 Annual Meeting

Venue: JW Marriott parq Vancouver
Location: Vancouver British Columbia , Canada

BEGINS: Jun 2, 2018
Ends: Jun 6, 2018

7th International Dietary Fibre Conference

Venue: De Doelen Concert Hall and Congress Centre
Location: Rotterdam, The Netherlands

BEGINS: Jun 4, 2018
Ends: Jun 6, 2018

14th International Conference On Diffusion In Solids And Liquids (DSL 2018)

Venue: Mercure Hotel Amsterdam City
Location: Amsterdam, The Netherlands

BEGINS: Jun 28, 2018
Ends: Jun 29, 2018

12th International Conference On Advanced Computational Engineering And Experimenting (Acex 2018)

Venue: Mercure Hotel Amsterdam City
Location: Amsterdam, The Netherlands

BEGINS: July 1, 2018
Ends: July 5, 2018

IFT'18 Annual Meeting, Theme: A Matter of Science and Food

Venue: McCormick Place
Location: Chicago, Illinois, USA

BEGINS: July 15, 2018
Ends: July 18, 2018

ASME Pressure Vessels & Piping Conference (PVP 2018)

Venue: Hilton Prague
Location: Prague, Czech Republic

BEGINS: July 15, 2018
Ends: July 20, 2018

International Design Engineering Technical Conferences & Computers & Information in Engineering Conference (IDETC/CIE 2018)

Venue: Hilton Québec
Location: Quêbec, Canada

BEGINS: August 26, 2018
Ends: August 29, 2018

7th EuCheMS Chemistry Congress, Molecular frontiers and global challenges

Venue: ACC Liverpool
Location: Liverpool, UK

BEGINS: August 26, 2018
Ends: August 30, 2018

XXV EFMC International Symposium on Medicinal Chemistry (EFMC-ISMC 2018)

Venue: Ljubljana Exhibition and Conv. Centre
Location: Ljubljana, Slovenia

BEGINS: September 2, 2018
Ends: September 6, 2018

2018 International Conference on Solid State Devices and Materials (SSDM2018)

Venue: Hongo Campus, The University of Tokyo
Location: Tokyo, Japan

BEGINS: September 9, 2018
Ends: September 13, 2018

5th Nuclear Materials Conference (NuMat 2018)

Venue: Motif Seattle
Location: Seattle, WA, USA

BEGINS: Oct 14, 2018
Ends: Oct 18, 2018

19th International Metallurgy and Materials Congress

Venue: TUYAP Fair, Conv. and Congress Center
Location: İstanbul, Turkey

BEGINS: Oct 25, 2018
Ends: Oct 27, 2018

Abstracted & Indexed in:

TR Dizin Mühendislik ve Temel Bilimler Veri Tabanı |
CrossRef | Google Scholar | MIP Database | StuartxChange | ResearchBib | Scientific Indexing Services (SIS)

HITTITE